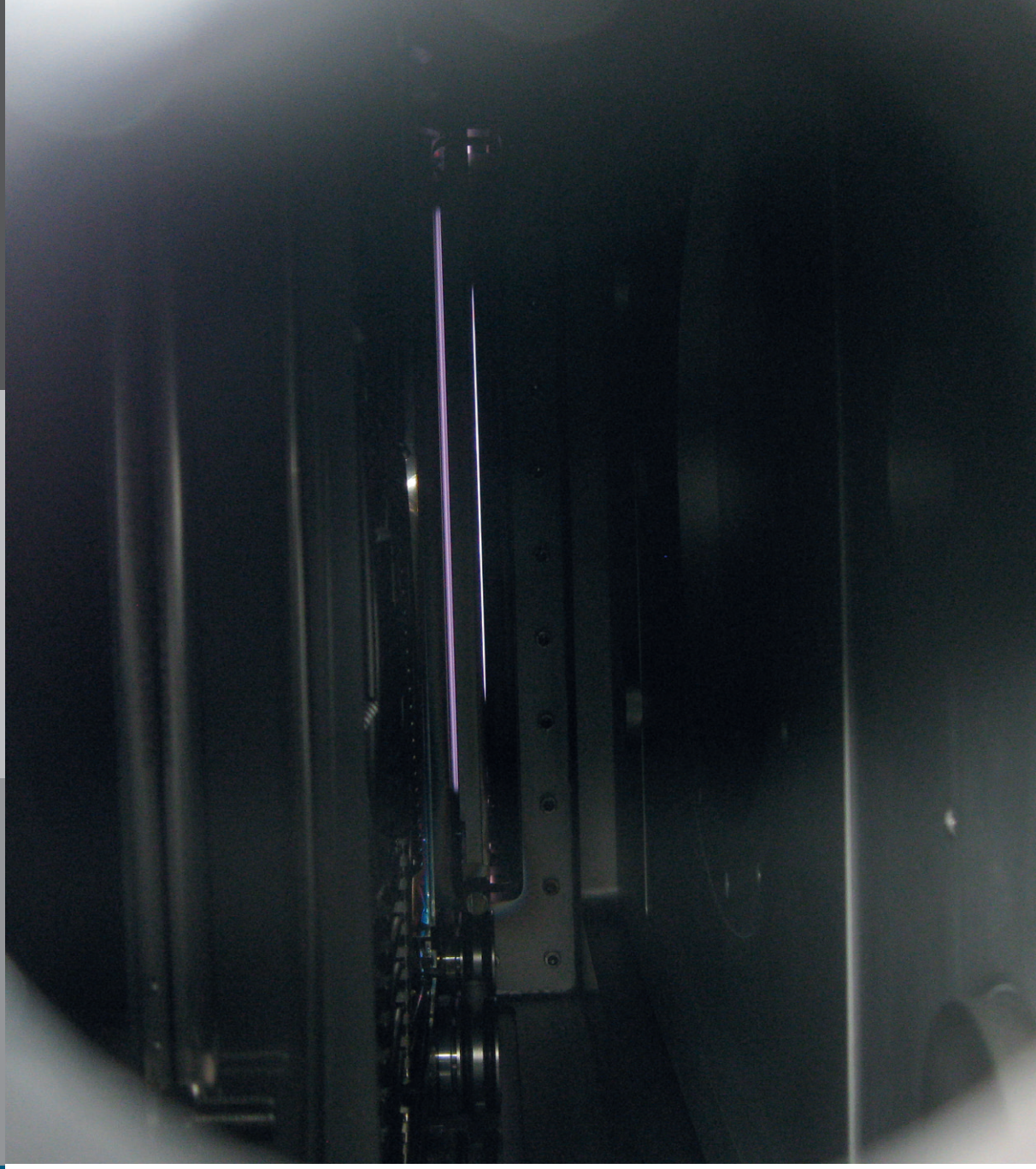

# Impact of contamination on hydrogenated amorphous silicon thin films & solar cells

Jan Wördenweber

Mitglied der Helmholtz-Gemeinschaft

JÜLICH
FORSCHUNGSZENTRUM

Schriften des Forschungszentrums Jülich
Reihe Energie & Umwelt / Energy & Environment Band / Volume 103

Forschungszentrum Jülich GmbH
Institute of Energy and Climate Research (IEK)
Photovoltaic (IEK-5)

# Impact of contamination on hydrogenated amorphous silicon thin films & solar cells

Jan Wördenweber

Schriften des Forschungszentrums Jülich
Reihe Energie & Umwelt / Energy & Environment Band / Volume 103

ISSN 1866-1793 ISBN 978-3-89336-697-2

Bibliographic information published by the Deutsche Nationalbibliothek.
The Deutsche Nationalbibliothek lists this publication in the Deutsche Nationalbibliografie; detailed bibliographic data are available in the Internet at http://dnb.d-nb.de.

| | |
|---|---|
| Publisher and Distributor: | Forschungszentrum Jülich GmbH<br>Zentralbibliothek<br>52425 Jülich<br>Phone +49 (0) 24 61 61-53 68 · Fax +49 (0) 24 61 61-61 03<br>e-mail: zb-publikation@fz-juelich.de<br>Internet: http://www.fz-juelich.de/zb |
| Cover Design: | Grafische Medien, Forschungszentrum Jülich GmbH |
| Printer: | Grafische Medien, Forschungszentrum Jülich GmbH |
| Copyright: | Forschungszentrum Jülich 2011 |

Schriften des Forschungszentrums Jülich
Reihe Energie & Umwelt / Energy & Environment Band / Volume 103

D 82 (Diss., RWTH Aachen, University, 2010)

ISSN 1866-1793
ISBN 978-3-89336-697-2

The complete volume ist freely available on the Internet on the Jülicher Open Access Server (JUWEL) at http://www.fz-juelich.de/zb/juwel

# Einfluss von Verunreinigungen auf hydrogenisierte, amorphe Silizium Dünnschichten und Solarzellen

**Kurzfassung** Diese Studie beschäftigt sich mit dem Einbau von Sauerstoff und Stickstoff während der Deposition amorpher, intrinsischer Absorberschichten (i-Schichten) für p-i-n Dünnschichtsolarzellen aus amorphem, hydrogenisiertem Silizium (a-Si:H). Des Weiteren wird die Problematik der Bor-Verschleppung bei Einkammerprozessen untersucht.

Die atmosphärischen Verunreinigungen wurden während der Deposition der nominell unkontaminierten i-Schicht mittels künstlicher Lecks hinzugefügt. Untersucht wurde unter anderem der Einfluss der Art der Verunreinigung (Sauerstoff & Stickstoff), der zugefügten Menge der Verunreinigung (Leckflussrate), des Ortes der Verunreinigung (Kammerleck bzw. Prozessgasleitung) und der Plasmaleistung auf die Solarzelleneigenschaften. Dadurch können z.B. Vakuum-mindestanforderungen, mögliche Lecks im Rezipienten, Prozessgasmindest-reinheiten und Prozessgasleitungslecks simuliert werden. Des Weitern wurden Depositionsregime entwickelt, mittels derer der Einbau von Verunreinigungen unterdrückt werden kann. Unter Standardbedingungen fanden sich kritische Stickstoff- und Sauerstoff-Kontaminationsgrenzen (Kammerleck) von etwa $4\times10^{18}\,cm^{-3}$ bzw. $2\times10^{19}\,cm^{-3}$ überhalb derer es zu einer starken Abnahme des Wirkungsgrads der Solarzelle kam. In der Literatur wird als eine Hauptursache der Wirkungsgradabnahme der Einbau von Verunreinigungen in dotierender Konfiguration diskutiert. Begleitende Materialstudien innerhalb dieser Arbeit unterstützen diese These.

Die unterschiedlichen Maximalkontaminationen lassen sich durch unterschiedliche Dotiereffizienzen deuten. So ist die dotierende Wirkung des eingebauten Stickstoffs um etwa eine Größenordnung über der des Sauerstoffs. Allerdings ist auch die Einbauwahrscheinlichkeit von Sauerstoff um etwa eine Größenordnung höher als die für Stickstoff, was dazu führt, dass bei einem Luftleck beide Kontaminationsgrenzen gemeinsam bei einem bestimmten Luftleckfluss erreicht werden.

Bei Benutzung des Lecks in der Prozessgasleitung hingegen fand sich für Sauerstoff ein kritisches Level von etwa $2\times10^{20}\,cm^{-3}$, wo hingegen das kritische Stickstoffniveau vom Leckort unabhängig ist. Für ein Depositionsregime mit sehr hohem Prozessgasfluss wurde auch für das Kammerleck eine kritische Sauerstoffkonzentration von $2\times10^{20}\,cm^{-3}$ beobachtet.

Mögliche Ursachen sind einerseits die von Regime und Leckageort abhängigen Reaktionswahrscheinlichkeiten von Silan ($SiH_4$), Silan Radikalen und atomarem Wasserstoff mit Sauerstoff. Z.B. ist die Konzentration an atomarem Wasserstoff in der Gasleitung gering im Vergleich zur Umgebung des Kammerlecks. Durch diese Reaktionen entstehen z.B. $SiO_x$, Siloxan- ($SiH_3$-O-$SiH_3$) oder OH / $H_2O$-Molekühle. Andererseits spielt auch die Lebensdauer dieser Moleküle und damit ihre Einbaugeschwindigkeit eine Rolle. Letztere kann für verschiedene Regime durchaus

unterschiedlich sein. Für $SiO_X$ wird angenommen, dass es mit hoher Wahrscheinlichkeit nicht in die Schicht eingebaut wird, es entsteht Staub in der Depositionsanlage. Siloxan, von dem angenommen wird, dass der darin enthaltene Sauerstoff nicht dotierend eingebaut wird, hat eine hohe Lebensdauer und wird sehr wahrscheinlich in die Schicht eingebaut, wenn es nicht anderweitig abgepumpt / gebunden wird. Hingegen haben die Wasserstoffverbindungen eine begrenzte Lebensdauer, was u. U. dazu führt, dass sie in einem Regime eingebaut werden (schneller Einbau), in einem anderen nicht (langsamer Einbau). Es wird angenommen, dass OH / $H_2O$ Molekühle zum Einbau von Sauerstoff in Dotierkonfigurationen führen können.

Beim Stickstoff sind diese Mechanismen aufgrund der sehr trägen Reaktion mit Silan nicht gegeben. Folglich findet sich ein eindeutiges kritisches Stickstoffniveau unabhängig von der Art des Lecks. Ein weiteres, überraschendes Ergebnis dieser Studie ist, dass die kritischen Verunreinigungskonzentrationen nach der Lichtalterung unverändert geblieben sind. Darüber hinaus zeigte sich, dass eine hohe Plasmaleistung, angewandt z.B. bei Standard-Depositionsbedingungen von mikrokristallinem Silizium, dazu führt, dass der Unterschied der kritischen Sauerstoffkonzentration verschwindet. Dies liegt möglicherweise daran, dass die gebildeten Siloxan-Moleküle durch die hohe Leistungsdichte wieder aufgespaltet werden. Hier führten extrem niedrige Leistungsdichten für µc-Si:H Depositionen wieder zu einem erhöhten kritischen Sauerstoffniveau.

Ein weiterer Punkt dieser Arbeit ist die Verbesserung von Einkammerprozessen zur Herstellung von amorphen Dünnschichtsolarzellen. Hauptaugenmerk hierbei war die Verschleppung von Bor-Atomen, die zur Dotierung der p-Schicht nötig sind, in die i-Schicht. In dieser Arbeit sind verschiedene Solarzellkonfigurationen und Reaktorbehandlungen zur Vermeidung der Bor-Verschleppung systematisch untersucht worden. Die Reaktorbehandlungen wurden untereinander in Punkto Effektivität, Wirkungsweise und Zeitaufwand verglichen.

Als Reaktorbehandlung vor der Deposition der i-Schicht haben sich eine Wasserdampf-Spülung und das einfache Abpumpen des Reaktors auf $9\times10^{-7}$ mbar als schnell und zuverlässig erwiesen. Nachteil der Wasserdampf Behandlung ist die Kontrolle über selbige. Nachteil der Abpumpmethode ist, dass sie nicht in allen Anlagen funktioniert: Scheinbar ist in großflächigen Anlagen das Bor-Recycling von den Wänden vernachlässigbarer, als bei kleinen Anlagen. Auch scheint ein direktes Abpumpen der Prozessgase vorteilhaft zu sein. Die Anwendung von $CO_2$-Reinigungsplasmen ist genauso effektiv, wie die beiden vorherigen Methoden, jedoch stellt sie eine ex-situ Reinigungsmethode dar, wobei das Substrat aus der Depositionskammer ausgeschleust werden muss. Dadurch dauert diese Art der Reinigung im Vergleich zu Wasserdampf-Spülung und einfachem Abpumpen des Reaktors etwa doppelt so lang.

Letztendlich ist es gelungen, mit einem Einkammerprozess a-Si:H Solarzellen ($1 \times 1$ cm$^2$) und –module ($40 \times 40$ cm$^2$) mit einem Anfangs-Wirkungsgrad von 10.4 % bzw. 9 % zu fertigen.

# Impact of contamination on hydrogenated amorphous silicon thin films & solar cells

**Abstract** This thesis deals with atmospheric contamination and cross-contamination of boron (single-chamber process) of the intrinsic absorber layer (i-layer) of p-i-n thin-film solar cells based on hydrogenated amorphous silicon.

The atmospheric contaminations were introduced by means of intentional leaks. Hereby, the focus is on the influence of contamination species (oxygen & nitrogen), quantity of contamination (leak flow), source of contamination (leaks at chamber wall or in the process gas pipe), and plasma power on the properties of solar cells. Thereby, the minimum requirements for the purity of vacuum and process gas as well as leak conditions of the recipient and gas pipe system have been determined. Additionally, deposition regimes were developed, where the incorporation of impurities is significantly suppressed.

For standard processes critical levels of nitrogen and oxygen contamination are determined to be ~ $4\times10^{18}$ $cm^{-3}$ and ~ $2\times10^{19}$ $cm^{-3}$, respectively, for a leak situated at the chamber wall. Above these concentrations the solar cell efficiency deteriorates. In literature, incorporation of oxygen and nitrogen in doping configuration is assumed to be the reason for the cell deterioration. This assumption is supported by additional material studies of contaminated absorber layers done in this work. The difference in critical concentration is due to the higher doping efficiency of nitrogen compared to that for oxygen. Nevertheless, applying an air leak the critical concentrations of O and N are reached almost simultaneously since the incorporation probability of oxygen is about one order of magnitude higher compared to that for nitrogen.

Applying a leak in the process gas pipe the critical oxygen contamination level increases to ~ $2\times10^{20}$ $cm^{-3}$ whereas the critical nitrogen level remains unchanged compared to a chamber wall leak. Applying a deposition regime with a very high flow of process gases for oxygen the higher critical contamination level is found as well for a chamber wall leak.

Possible reasons for the dependence of the critical oxygen contamination on the deposition regime and the oxygen source may be the following. Before entering the plasma zone the oxygen can react with hydrogen atoms, silane (very high reaction probability), or silane radicals. Mainly, three reaction products may result, namely $SiO_2$-clusters, siloxane ($SiH_3$-O-$SiH_3$), and OH / $H_2O$ molecules. The $SiO_2$ is assumed to drop to the bottom of the reactor or to be pumped out. If oxygen is incorporated from siloxane, it is assumed to be electrically inactive. In contrast, oxygen incorporated from hydrogen-oxygen molecules leads to oxygen incorporation in an electrically active configuration. For a source gas pipe leak, the density of silane in the gas pipe is high compared to that for the chamber wall leak. For the chamber wall leak the hydrogen density is assumed to be much higher compared to that for the process gas pipe leak. Thus, the critical oxygen concentration is suggested to increases due to the resulting higher siloxane to OH / $H_2O$ ratio for the gas pipe leak compared to that in the vicinity of the chamber wall leak. The different critical levels

for different deposition regimes can be explained by their oxygen incorporation velocity. The lifetime of the OH / $H_2O$ molecules is assumed to be shorter, compared to that for the siloxane. As a consequence this might lead to the fact, that oxygen form these molecules is incorporated in one regime (fast incorporation), and in another regime it is not incorporated (slow incorporation).

For nitrogen the same critical contamination levels are observed which is attributed to the lack of reactivity of silane and nitrogen. The observed critical impurity concentrations do not change after light-soaking experiments of the solar cells. Besides, for oxygen incorporation via gas pipe leak at a high plasma power, usually applied for the deposition of microcrystalline silicon, only the lower critical oxygen concentration level is seen. This is attributed to the high power density that can lead to a decomposition of the siloxane. A series of gas pipe leak contaminated μc-Si:H solar cells deposited at a very low power density supported this model by showing, again, the increased critical oxygen contamination level.

A further aspect of this thesis is to improve the single-chamber process for the fabrication of amorphous hydrogenated silicon thin-film solar cells. The main aspect is the suppression of boron cross-contamination. Before the deposition of the i-layer a boron doped p-layer is deposited and thus, after the p-layer deposition some of the boron remains in the recipient. In this work different solar cell configurations and reactor treatments are examined for their suppression of the boron cross-contamination. The various treatments are compared for their effectivity, their working principle, and their time consumption. Amongst the investigated reactor treatments the application of a $H_2O$-flush or a process chamber evacuation to $9\times10^{-7}$ mbar turned out to be most favourable in order to suppress the boron cross-contamination. These two in-situ methods are fast and efficient. A drawback for the $H_2O$-flush is that this treatment is rather difficult to control. The chamber evacuation to $9\times10^{-7}$ mbar did not work in all deposition systems. It is assumed that for larger deposition systems the boron recycling from the chamber walls plays a minor role compared to that for a small-area deposition system. The application of a $CO_2$-plasma treatment had a similar effectivity compared to the two presented methods but this is an ex-situ reactor treatment and the substrate has to be moved out of the deposition chamber prior to the $CO_2$-plasma. Therefore, the $CO_2$-plasma treatment is ~ two times more time consuming compared to the $H_2O$-flush or to the process chamber evacuation to $9\times10^{-7}$ mbar.

Finally, with a real single-chamber process solar cell ($1 \times 1$ cm$^2$) and module ($40 \times 40$ cm$^2$) initial efficiencies of 10.4 % and 9 % are achieved, respectively.

# Contents

## Publications related to this study

- J. WOERDENWEBER, T. MERDZHANOVA, R. SCHMITZ, A. MUECK, D. HRUNSKI, U. ZASTROW, L. NIESSEN, A. GORDIJN, H. STIEBIG, W. BEYER, and U. RAU, Dependence of a-Si:H solar cell performances on contamination sources and species during plasma deposition - *Proceedings of the 23rd European Photovoltaic Solar Energy Conference, Valencia, Spain / ed.: D. Lincot, H. Ossenbrink, P. Helm.- Muenchen, WIP*, 2008, S. 2121 – 2124.

- J. WOERDENWEBER, T. MERDZHANOVA, R. SCHMITZ, A. MUECK, U. ZASTROW, L. NIESSEN, A. GORDIJN, R. CARIUS, W. BEYER, H. STIEBIG, and U. RAU, Influence of base pressure and atmospheric contaminants on a-Si:H solar cell properties, *Journal of Applied Physics* **104** (2008), 094507.

- T. MERDZHANOVA, J. WOERDENWEBER, W. BEYER, A. GORDIJN, R. SCHMITZ, A. MUECK, U. ZASTROW, L. NIESSEN, J. KLOMFASS, W. REETZ, H. STIEBIG, and U. RAU, Thin-film amorphous silicon solar cells deposited under high base pressure conditions and their light-soaking stability, - *Proceedings of the 24rd European Photovoltaic Solar Energy Conference, Hamburg, Germany / ed.: W. Sinke, H. Ossenbrink, P. Helm.- Muenchen, WIP*, 2009, S. 2660 – 2664.

- J. WOERDENWEBER, T. MERDZHANOVA, H. STIEBIG, W. BEYER, and A. GORDIJN, Critical oxygen concentration in hydrogenated amorphous silicon solar cells dependent on the contamination source, *Applied Physics Letters* **96** (2010), 103505

- T. MERDZHANOVA, J. WOERDENWEBER, T. KILPER, H. STIEBIG, W. BEYER, and A. GORDIJN, Critical Concentrations of Atmospheric Contaminants in a-Si:H and μc-Si:H Solar Cells, *Amorphous and Polycrystalline Thin-Film Silicon Science and Technology — 2010, MRS Proceedings* Volume **1245** - A02-04

- T. MERDZHANOVA, J. WOERDENWEBER, W. BEYER, U. ZASTROW, H. STIEBIG, and A. GORDIJN, High critical oxygen concentration in microcrystalline silicon solar cells, *accepted for publication in Physica Status Solidi RRL 1–3 (2010) / **DOI** 10.1002*

- J. WOERDENWEBER, T. MERDZHANOVA, H. STIEBIG, W. BEYER, and A. GORDIJN, Incorporation and critical concentration of oxygen in a-Si:H solar cells, *to be published*

- J. WOERDENWEBER, T. MERDZHANOVA, A.J. FLIKWEERT, T. ZIMMERMANN, U. ZASTROW, L. NIESSEN, W. REETZ, H. STIEBIG, W. BEYER, and A. GORDIJN, Single chamber process for deposition of thin-film solar cells without plasma treatment, *to be published in Proceedings of the 25rd European Photovoltaic Solar Energy Conference, Valencia, Spain*

- T. MERDZHANOVA, J. WOERDENWEBER, U. ZASTROW, L. NIESSEN, H. STIEBIG, W. BEYER, and A. GORDIJN, Oxygen, nitrogen and air leakages during deposition of thin-film silicon solar cells, *to be published in Proceedings of the 25rd European Photovoltaic Solar Energy Conference, Valencia, Spain*

# List of abbreviations and symbols

**Abbreviations:**

| | |
|---|---|
| AM | air-mass |
| a-Si:H | hydrogenated amorphous silicon |
| a-SiC:H | hydrogenated amorphous silicon carbide |
| CPM | constant photocurrent method |
| CWL | chamber wall leak |
| DSR | differential spectral response |
| FTIR | Fourier transformed infrared spectroscopy |
| FZ-Si | float zone silicon |
| GPL | gas pipe leak |
| HFHP I | high-flow high-pressure deposition regime I (see page 35) |
| HFHP II | high-flow high-pressure deposition regime II (see page 54) |
| LFLP | low-flow low-pressure deposition regime (see page 54) |
| LS | light-soaking |
| μc-Si:H | hydrogenated microcrystalline silicon |
| MFC | mass flow controller |
| MPP | maximum power point |
| PDS | photothermal deflection spectroscopy |
| (PE)CVD | (plasma enhanced) chemical vapour deposition |
| p-i-n | p-doped – intrinsic – n-doped |
| ppb | parts per billion |
| ppm | parts per million |
| *QE* | quantum efficiency |
| *SC* | silane concentration |
| SIMS | secondary ion mass spectrometry |
| SWE | Staebler-Wronski effect |
| TCO | transparent conductive oxide |
| TMB | trimethylboron |
| VHF | very high frequency |

**Symbols:**

| | |
|---|---|
| $\alpha$ | absorption coefficient |
| $A_x$ | FTIR proportionality constants |
| $\beta$ | rate constant for irregular impurity incorporation |
| $C_H$ | hydrogen content |
| $C_I$ | impurity concentration |
| $d$ or $d_I$ | (impurity) distribution coefficient |
| $D^{+,\,0,\,-}$ | (charged) defect state |
| $d_{film}$ | film thickness |
| $d_{irreg}$ | irregular part of distribution coefficient |
| $d_{reg}$ | regular part of distribution coefficient |
| $E_{04}$ | energy at which the absorption coefficient $\alpha$ is $10^4$ cm$^{-1}$ |

| | |
|---|---|
| $E_a$ | amorphous binding energy |
| $E_A$ | activation energy |
| $E_{AB}$ | energy needed for acceptance of additional electron |
| $E_B$ | bonding energy |
| $E_c$ | crystalline binding energy |
| $E_D$ | network distortion energy |
| $E_F$ | Fermi energy |
| $E_{pro}$ | promotion energy of impurity electrons |
| $\Phi$ | gas flow / photon flux |
| $F$ | electrical field strength |
| $FF$ ($FF_{red\ /\ blue}$) | fill factor (red / blue illumination) |
| $\gamma$ | energy loss factor due to the non-symmetric bonding alloying factor (see distribution coefficient) |
| $G$ | generation rate |
| $\eta$ | cell efficiency |
| $\eta_{ini}$ | initial cell efficiency |
| $\eta_{satb}$ | cell efficiency after 1000 h of light-induced dagradation |
| $\eta_G$ | gas phase doping efficiency |
| $\eta_S$ | solid phase doping efficiency |
| $I^*$ | irregularly incorporated impurity |
| $I_{photo}$ | photocurrent |
| $I_x$ | x-fold-coordinated impurity (charge marked as $I^+$ or $I^-$) integrated FTIR intensity at wavenumber x |
| $j$ | current density |
| $j_0$ | saturation current density |
| $j_{00}$ | pre-factor |
| $j_{dark}$ | dark current density |
| $j_{photo}$ | photocurrent density |
| $j_{SC}$ ($j_{SC\ red\ /\ blue}$) | short circuit current density (red / blue illumination) |
| $\mu$ | carrier mobility |
| $n$ | diode quality factor |
| $N$ | photon density |
| $N_D$ | defect density |
| $N_x$ | particle density |
| $P$ | applied discharge power |
| $p_b$ | base pressure |
| $Qe$ | quantum efficiency |
| $R$ | reflection coefficient |
| $R^*$ | microstructure factor |
| $r_d$ | deposition rate |
| $R_S$ | series resistance |
| $R_{SH}$ | parallel resistance |
| $\sigma_{dark}$ | dark conductivity |
| $\sigma_{photo}$ | photoconductivity |

| | |
|---|---|
| $\tau$ | carrier lifetime |
| $t$ | time |
| $T$ | temperature |
| | transmission |
| $T_H$ | heater temperature |
| $T_S$ | substrate temperature |
| $U$ | Voltage |
| $V_{OC}$ | open circuit voltage |
| $\omega$ | wavenumber |
| [X] | solid phase concentration of species X |
| $X_{G,I}$ | gas phase mole fraction of impurity |
| $X_{S,I}$ | solid phase mole fraction of impurity |
| $X_p$ | fraction of non contaminated i-layer |

**Physical constants:**

| | |
|---|---|
| $e$ | elementary charge ($1.602\times10^{-19}$ C) |
| $k_B$ | Boltzmann constant ($1.38\times10^{-23}$ JK$^{-1}$) |

**Useful conversion factors**

| | |
|---|---|
| 1 Torr | 133.3 Pa |
| 1 bar | $10^5$ Pa |
| 0°C | 273.15 K |

# 1. Introduction

The intention of this study is to further develop, improve and understand the deposition technology of amorphous silicon based thin-film solar cells. This is motivated by the increasing demand on energy production all over the world that cannot be satisfied by conventional energy sources. Sustainable and renewable forms of energy production are needed to sustain our living quality as well. One contribution to the numerous ways of renewable energy is given by the photovoltaic sector.

## 1.1. Silicon-based thin-film solar cells

Up to now the photovoltaic market is dominated by silicon waver-based solar modules and to some extent by CdTe based thin-film solar cells, [Jae2007], [Jae2009] & [Kai2009]. Recently, the thin-film silicon solar cell market has strongly developed and still is growing and this technological concept offers many advantages:

- Less material is consumed since the photovoltaic active layer of amorphous, hydrogenated silicon solar cells (a-Si:H) is only 0.3 μm thick, compared to a silicon waver thickness in the order of 100 μm. Microcrystalline hydrogenated silicon solar cells (μc-Si:H) are about 1.2 μm thick which is ~ 1 % of the silicon waver thickness. Thus, also less energy is consumed for the production and purification of the material used for the composition of the cell.
- Due to the development of large-area deposition systems and integrated series connection of the solar cells to modules "turn-key" equipment for an automatic series production is available.
- A large variety of (flexible) substrates can be used since the deposition temperature is very low [Pie2008]. Materials like glass [Ong2006] & [Ich1993], metal (foils) [Yan1994] & [Don2007] or even organic foils for instance made from plastic [Ich1994] & [Shi1994] are applicable.
- Silicon as basic ingredient is largely available and non-toxic which is a great advantage compared to most other thin-film solar cell concepts.

This study deals with amorphous (a-Si:H) and microcrystalline (μc-Si:H) hydrogenated silicon thin-film solar cells. The concept of a-Si:H solar cells was first reported in 1965 by Sterling and Swan [Ste1965]. In 1975 Spear and LeComber for the first time showed the possibility of doping a-Si:H which formerly was believed to be impossible due to its amorphous structure which was assumed to be too flexible for substitutional doping [Spe1975]. From this time the development of complete a-Si:H p-i-n solar cells started and the first cell was produced by Carlson and Wronski in 1976 [Car1976]. In these cells the absorption takes place in the intrinsic (i-)layer. The p- and n-doped layers are responsible for the electrical field over the i-layer in order to extract the generated charge carriers. One year later Staebler and Wronski [Sta1977] discovered the light-induced degradation of a-Si:H solar cells (Staebler-Wronski effect, SWE). As a consequence today's research concentrates on stabilized high-efficiency solar cells. A step towards this aim is the fabrication of multijunction cells since the amorphous part of the layer stack degrades less in these concepts because of a reduced film thickness of the amorphous absorber layer. Also the solar spectrum can be used more effectively in multijunction cells where the different absorber layers have different band gaps. For example, silicon-germanium alloys (a-SiGe:H) have a better absorption in the range of long wavelengths than a-Si:H [Zem1991].

Besides the improvement of the absorber layer other aspects like light trapping [Mue2004] and thus effective absorption path lengthening by means of textured transparent conducting oxides (TCO) were improved as well as absorption losses in the p-layer were reduced by means of carbon additives to form an a-SiC:H p-layer with a larger band gap compared to a-Si:H [Ift1998].

## 1.2. Outline

A better understanding of the properties of the absorber layer and their significance for p-i-n solar cells is crucial for an improvement of the solar cell efficiencies. In this work the effect of atmospheric contamination of the intrinsic absorber layer and the resulting effects on single- and embedded absorber layers are studied. On the one hand the knowledge of how these impurities are incorporated is crucial to understand how they act in a solar cell. On the other hand understanding the impact of impurities on solar cells might lead to improvements of the process conditions towards significant suppression of the negative influence of impurities. The highest allowed concentrations of impurities in the absorber layer are to be established and the vacuum- and process gas requirements can be possibly reduced accordingly, leading to economisation of the costs.

A further possibility of introducing impurities into the i-layer is given by the so called cross-contamination that appears especially for the application of single-chamber processes. This means that the doped and intrinsic layers are all fabricated in the same chamber. The cross-contamination, e.g., of boron from the p-layer growth process into the absorber layer, leads to a reduction of the quality of the absorber layer. In this work the impact of boron cross-contamination on the solar cell

performance and its prevention by means of reactor treatments prior to the deposition of the i-layer are investigated in detail.

The structure of this work is as following:

In *chapter 2* a model describing the incorporation of impurities into a-Si:H is given. Based on this model the impact of various contaminations on the performance of thin-film solar cells can be described.

In *chapter 3* the experimental realisation of this work is shown. In the first section some basic aspects of the fabrication and working principle of solar cells are described followed by an explanation of the growth of thin-film solar cells. The subsequent sections provide information about the material- and solar analysing methods that are used in this work.

*Chapter 4-6* provide the experimental results concerning the atmospheric contamination of solar cells and single layers. For nitrogen and oxygen the highest tolerable concentrations in the absorber layer of the solar cell are analysed. These concentrations appear to depend on the way the impurities are inserted into the process and on the deposition regime. A new deposition regime is presented where the incorporation of cell deteriorating impurities is significantly reduced. Furthermore cell and layer properties as a function of impurity concentrations are compared and discussed. In *chapter 4* a general overview over the state-of-the-art of science and technology concerning atmospheric contamination is given.

In *chapter 7* the incorporation of oxygen and nitrogen is compared to the incorporation of arsenic and phosphorus in order to reveal similarities and differences for their incorporation compared to that of arsenic and phosphorus.

Recent developments concerning single-chamber deposition processes for a-Si:H are presented in *chapter 8*. The impact of boron cross-contamination on the solar cell performance and the reduction of the cross-contamination via reactor treatments and cell configurations are discussed. A general overview over the state-of-the-art of science and technology of single-chamber processes is given in this chapter.

# 2. Doping in hydrogenated amorphous silicon

In literature, the effect of impurity incorporation in the i-layer of a-Si:H solar cells is described as the incorporation of a part of the oxygen and nitrogen impurities in an electronically active donor-like configuration in the i-layer [Mor1991] & [Shi1991]. For oxygen this active state is proposed to be a threefold-coordinated state whereas for nitrogen it is proposed to be fourfold-coordinated [Mor1991]. Nevertheless, still the largest fraction will be incorporated in electronically non-active twofold-coordinated oxygen and threefold-coordinated nitrogen, respectively [Mor1991]. For the thin-film p-i-n solar cell the incorporation of oxygen or nitrogen in doping configuration implies a weakening of the electrical field, which is created by the p- and n-doped layers and extends over the i-layer. This leads to a reduced extraction of charge carriers from the bulk [Kin1996]. For deeper understanding of the incorporation of oxygen and nitrogen it is helpful to first refer to doping of a-Si-H in general. A detailed study of phosphorous and arsenic doping of a-Si:H was done by Stutzmann et al. [Stu1987], Street et al. [Str1982], and Wiener et al. [Win1990]. The proposed models are discussed in the following sections.

## 2.1. Substitutional doping in a-Si:H

Up to 1975 it was widely believed that it is impossible to substitutionally dope amorphous silicon because of the disorder in the material. Every impurity was assumed to build its non-doping configuration [Str1982] & [Mot1967]. In general, substitutional doping in crystalline silicon with a group-V element is possible because the crystalline binding energy $E_C(I_{(4)})$ of the fourfold-coordinated impurity (electronically active) given by

$$E_C(I_{(4)}) = E_{pro} - 4E_B + E_{AB} \tag{2.1}$$

is lower than the binding energy $E_C(I_{(3)})$ [Stu1987] of the non-doping threefold-coordinated impurity state given by

$$E_C(\mathrm{I}_{(3)}) = 3\gamma \cdot E_B + E_D . \qquad (2.2)$$

In equation (2.1), $E_{pro}$ is the energy that is needed to promote the impurity electrons into a hybridized $sp^3$ state necessary for the impurity-to-silicon bonding. $E_B$ is the energy which is gained by the 4 bonding electrons ($\sigma$-symmetry) with respect to their not-promoted configuration and $E_{AB}$ represents the energy needed for the fifth electron. For the non-active states $\gamma < 1$ is a factor describing the energy losses due to the non-symmetric bonding and, finally, $E_D$ describes the distortion of the network. In the crystalline network this leads to a doping efficiency of approximately 100 %.

For amorphous silicon this simple picture is no longer valid. If the short range order in amorphous silicon is assumed to be similar to the one of crystalline silicon, the impurity may be incorporated fourfold-coordinated but in the amorphous state the binding energy $E_a(\mathrm{I}_{(4)})$ is larger than $E_a(\mathrm{I}_{(3)})$ because of variations in $E_B$ and $E_{AB}$ due to the disordered network. Furthermore, the threefold-coordinated incorporation of the impurities is promoted since the distortion energy and the loss of $\sigma$-symmetry do no longer exist.

Consequently, from this point of view no substitutional doping would be expected and the model has to be reconsidered for the amorphous case. The above described problem is also known as the so called "8-N" rule, introduced by Mott in 1967 [Mot1967]: "In the absence of topological constraints, substitutional doping can not occur in a-Si:H".

However, in 1975 the first study on substitutional doping of amorphous silicon was reported by Spear and LeComber [Spe1975] for the incorporation of phosphorous and boron. This can be explained by the application of the "8-N" rule to impurities that are charged at the time of deposition [Str1982]. The application of the "8-N" rule implies further that the Fermi energy level $E_F$ cannot move into the conduction band since a neutral donor state would violate the "8-N" rule. Furthermore, doping in a-Si:H always goes along with the creation of "compensating" defect states keeping the Fermi level away from the conduction band

$$\mathrm{I}^0_{(3)} + \mathrm{Si}^0_{(4)} \Leftrightarrow \mathrm{I}^+_{(4)} + \mathrm{Si}^-_{(3)} . \qquad (2.3)$$

In equation (2.3) Si and I represent the silicon and impurity states, respectively, which are negative, neutral, or positive charged. The coordination of the impurity and of the silicon is given by the numbers. Experimental evidence for this fact has been reported by Spear and LeComber [Spe1975].

## 2.2. Impurity distribution coefficients for arsenic and phosphorus

The distribution coefficient $d_I$ is defined as the ratio of the solid impurity fraction $X_{S,I}$ to the gas-phase impurity fraction $X_{G,I}$ [Win1990], given by

$$d_I = \frac{X_{S,I}}{X_{G,I}} = \frac{[I]}{[Si]+[H]+[I]} \times \frac{\Phi_I + \Phi_{SiH_4} + \Phi_{H_2}}{\Phi_I} \tag{2.4}$$

where [I], [Si], and [H] denote the solid-phase concentrations of the incorporated impurities, silicon, and hydrogen, respectively. The quantities $\Phi_I$, $\Phi_{SiH4}$, and $\Phi_{H2}$ are the applied flows of the impurities, silane, and hydrogen during the deposition of the intrinsic layer. Usually, $d_I$ is larger than unity which means that the impurity fraction in the solid is larger than in the source gas. For impurities like P or As in a-Si:H the distribution coefficient is given by [Win1990]:

$$d_I = d_{reg} + d_{irreg}(P, X_I) = d_{reg} + \frac{\beta}{r_d \sqrt{X_{G,I}}}. \tag{2.5}$$

This expression is empirically obtained from experimental data. The deposition rate is denoted by $r_d$, $\beta$ is an irregularity factor. The regular part $d_{reg}$ is found to be independent of substrate temperature $T_S$, total process gas flow $\Phi_{tot}$, applied discharge power $P$, and gas-phase fraction $X_{G,I}$ of the impurity [Win1990]. This distribution coefficient can be interpreted in the following way. From the gas phase of silicon $Si_{gas}$ and of the impurity $I_{gas}$ these atoms are incorporated into the solid either in form of $Si^0_{(4)}$, $Si^-_{(3)}$, $I^0_{(3)}$, or $I^+_{(4)}$ given by these reactions with reaction constants $K_1$, $K_2$, $K_3$, and $K_4$ [Win1990]:

$$Si_{gas} \leftrightharpoons Si_{(4)}, \qquad [Si_{(4)}] = K_1 X_{G,Si}; \tag{2.6}$$

$$Si_{gas} \leftrightharpoons Si^-_{(3)} - e^-, \qquad [Si^-_{(3)}]/[e^-] = K_2 X_{G,Si}; \tag{2.7}$$

$$I_{gas} \leftrightharpoons I_{(3)}, \qquad [I_{(3)}] = K_3 X_{G,I}; \tag{2.8}$$

$$I_{gas} \leftrightharpoons I^+_{(4)} + e^-, \qquad [I^+_{(4)}] \cdot [e^-] = K_4 X_{G,I}. \tag{2.9}$$

If all reaction constants would be independent of the gas-phase fraction $X_{G,I}$ and of the applied discharge power $P$, i.e. regular, the distribution coefficient would be given by $d_I = d_{reg}$. Thus, the incorporation of the impurities in regular non-doping and doping configurations would be described by equations (2.8) and (2.9), respectively. The fourfold coordinated state is energetically only slightly above the threefold coordinated state and the states are separated by a small energy barrier, shown for P in Figure 2.1 [Win1990]. These two energy levels represent the doping and non-doping substitutional P-configurations whose occupation is determined by the thermodynamical equilibrium [Win1990].

However, for As and P, $K_3$ is found to be irregular, i.e. dependent on $X_{G,I}$ and on $r_d$ [Win1990], leading to an additional irregular part of the distribution coefficient $d_{irreg}$, representing irregular impurity incorporation into non-doping very stable states. These stable states are assumed to be, for example, P-$H_n$ complexes. Their conversation to electronically active states may be prevented by an increased barrier or the conversion product may not be a shallow donor [Win1990] (see Figure 2.1).

Since the rate constant $K_3$ depends on $P$ and $X_{G,I}$ also the parameter $d_{irreg}$ depends on the gas phase fraction $X_{G,I}$, on the applied discharge power $P$, and on an empirical rate constant for irregular impurity incorporation $\beta$. This dependence might be interpreted in the following way [Win1990].

First it is helpful to look at the impurity, e.g., phosphorus deposition rate $r_P$ given by

$$r_{\mathrm{P}} = d_{\mathrm{P}} \times r_{\mathrm{Si}} \times X_{G,\mathrm{P}} = d_{reg} \times X_{G,\mathrm{P}} \times r_d + \beta \sqrt{X_{G,\mathrm{P}}}\,, \tag{2.10}$$

assuming that the deposition rate of silicon $r_{Si} \sim r_d$. Thus, the regular impurity incorporation is proportional to the deposition rate and to the impurity gas phase fraction. However, the irregular incorporation rate $r_{\mathrm{P}}^{*}$ only depends on $\sqrt{X_{G,\mathrm{P}}}$ and not on the deposition rate. If P is incorporated from $PH_3$ in an irregular P-$H_n$ complex, as suggested for the irregular P-incorporation, this reaction must account for the $\sqrt{X_{G,\mathrm{P}}}$ -dependence of $r_{\mathrm{P}}^{*}$.

$$\mathrm{Si}_{(3)} + \left(\mathrm{PH}_3\right)_{gas} \leftrightharpoons \mathrm{SiPH_n} + \mathrm{Z_{gas}} \tag{2.11}$$

From the law of mass of action the concentration of the unknown reaction product Z must be proportional to $\sqrt{X_{G,\mathrm{P}}}$. One suggestion for the rate limiting impact for irregular incorporation is the surface attachment at a Si-dangling bond and ionization of $PH_3$, i.e.,

$$\mathrm{Si}_{(3)} + \left(\mathrm{PH}_3\right)_{gas} \leftrightharpoons \mathrm{Si}_{(3)} \text{—} \mathrm{PH}_3^{+} + \left(\mathrm{e}^{-}\right)_{gas}. \tag{2.12}$$

This would lead to $r_{\mathrm{P}}^{*} \sim X_{G,\mathrm{P}}/[\mathrm{e}^{-}] \sim \sqrt{X_{G,\mathrm{P}}}$, requiring $[\mathrm{e}^{-}] \sim \sqrt{X_{G,\mathrm{P}}}$ (observed experimentally in [Str1982], [Str1985a] & [Str1985b]). Therefore, the amount of electrons at the surface, that also have an impact on the Fermi-level, might be a rate limiting issue for irregular impurity incorporation. However, there might be other reactions leading to irregular incorporation and in this direction further investigations are necessary.

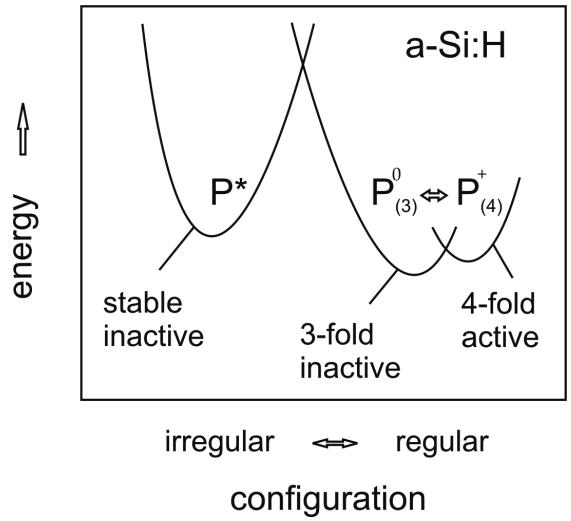


*Figure 2.1 Schematic diagram of the energy levels of impurities (P) incorporated in a-Si:H. The irregular part of the distribution coefficient accounts for the stable inactive P* states. The regular part accounts for the 3- or 4-fold coordinated impurities. This incorporation mode leads to doping. Diagram according to [Win1990].*

Since nitrogen is a group V element (like As or P) the incorporation of nitrogen might be similar to that of arsenic and phosphorus. For oxygen incorporation in a-Si:H, which is extensively studied in this work, comparable mechanisms might apply. An analysis of the incorporation behavior of N and O is given in *chapter 7*

# 3. Experimental methods

In this chapter first the applied fabrication process of hydrogenated amorphous silicon (a-Si:H) and microcrystalline silicon (μc-Si:H) material and solar cells is discussed. In the second part of this chapter the measurement techniques are introduced that are used for the characterisation of the material properties of silicon films and solar cell devices. Finally, the characterization methods used for complete solar cells are briefly described.

## 3.1. Deposition of silicon films and solar cells

In this section insight into the deposition of thin-film silicon solar cells by means of a plasma-enhanced chemical vapour deposition (PECVD) process is given.

### 3.1.1. Plasma-enhanced chemical vapour deposition

Various methods are used for the preparation of hydrogenated amorphous and microcrystalline silicon thin-films. Plasma-enhanced chemical vapour deposition (PECVD) is the most prominent method for the deposition of a-Si:H and μc-Si:H thin-films. This technique is established for industrial manufacturing of photovoltaic devices of up to 5.7 $m^2$ [Ama2010] from these films.

In this work the source gases silane ($SiH_4$) and hydrogen ($H_2$) are used to deposit the intrinsic a-Si:H or μc-Si:H absorber layers. In order to induce the decomposition of $SiH_4$ below the temperature necessary for thermal decomposition of $SiH_4$ (~ 450 °C), capacitively coupled parallel plate electrodes are used to apply an rf-plasma (13.56 MHz). The silane radicals can be adsorbed at the substrate surface and contribute to the film growth. A typical decomposition reaction of $SiH_4$ into, e.g., a $SiH_3$ radical is given by:

$$2\left(SiH_4 + e^-\right) \rightarrow 2\left(SiH_3 + 2H + e^-\right) \rightarrow 2\left(SiH_3 + e^-\right) + H_2 \qquad (3.1)$$

Generally, $SiH_3$ radicals are assumed to be precursors leading to a high quality film growth [Sch1993]. Nevertheless, these radicals probably do not reach the growing surface without undergoing further reactions with other molecules present in the

deposition chamber. At the usual low deposition pressures $p_d$ of a few Torr the mean free path of these radicals is less than some tens of a millimetre, thus, these radicals can react to various other radicals that contribute to deposition of low quality films. Besides the type of precursors, also the mobility of the adsorbed radicals and the 'radical lifetime', i.e., the path length of the radical on the substrate surface, have an impact on the film quality in terms of micro-voids, defects, etc. A long path length increases the possibility of the radical to find a good binding side. A parameter influencing the mobility is the substrate temperature $T_S$. High temperatures lead to a high mobility of the radical. Furthermore, hydrogen is expected to cover the growing surface and to enhance the radicals mobility [Mat1986] & [Mat1987]. In addition, unfavourable weak bonded silicon atoms or impurities can be etched or passivated by hydrogen [Tsa1988]. This may explain the tendency of a more ordered film growth. Nevertheless, these ideas are discussed controversially in literature. In turn, e.g., a high deposition rate leads to a low 'radical lifetime' because the radical is covered by the growing film.

Until now, parameters for the deposition of a-Si:H or μc-Si:H, such as substrate temperature $T_S$ or deposition pressure $p_d$, have been introduced. Additionally, the most important deposition parameters are discussed in the following:

I) The applied discharge power P determines the silane dissociation rate and the composition of radicals. For example, at higher power densities the formation of SiH or $SiH_2$ radicals becomes more likely compared to the formation of $SiH_3$ [Ama2001]. A higher dissociation rate has an important influence on the deposition rate. Above a certain threshold a phase transition between amorphous and microcrystalline growth is observed

II) The silane concentration *SC* is another key deposition parameter and is given by the ratio of silane flow $\Phi_{SiH4}$ to total flow of silane and hydrogen $\Phi_{SiH4} + \Phi_{H2}$ according to

$$SC = \frac{\phi_{SiH_4}}{\phi_{SiH_4} + \phi_{H_2}} \qquad (3.2)$$

The *SC* also has an important influence on the deposition rate and below a certain threshold a phase transition between amorphous and microcrystalline growth is observed, similar to the impact of the applied discharge power. Depending on the silane concentration many nuances of crystalline volume fractions can be established in the amorphous matrix. In recent years it has been demonstrated that the best amorphous and microcrystalline silicon solar cells were deposited for conditions closely before and after the transition between amorphous and microcrystalline growth, respectively [Vet2000].

III) The total gas flow determines, for instance, the residence time of the film precursors which is the average time a precursor has got to find a bonding site before being pumped out of the deposition chamber. Furthermore process condition independent flows of impurities (e.g., introduced into the chamber by controlled leakages) might be more diluted due to the higher process gas flow.

IV) The deposition pressure influences the mean free pathlength of the precursors and, thus, the frequency of collisions between them. Furthermore, the frequency of secondary reactions between radicals in the plasma zone depends of the deposition pressure.

### 3.1.2. Deposition system I (5K)

All silicon single layers and solar cells presented in *chapters 4-7* have been grown in the PECVD system I (Glasstech Solar Inc., USA, delivered by Material Research Group MRG Inc., USA) that is schematically presented in Figure 3.1. It contains 5 deposition chambers (5-chamber-PECVD deposition setup, abbreviated with 5K) which are interconnected by transport and load locks. The substrate with dimensions of 10 × 10 $cm^2$ is mounted on a metal substrate holder, which can be moved within a rail system (not indicated on Figure 3.1).

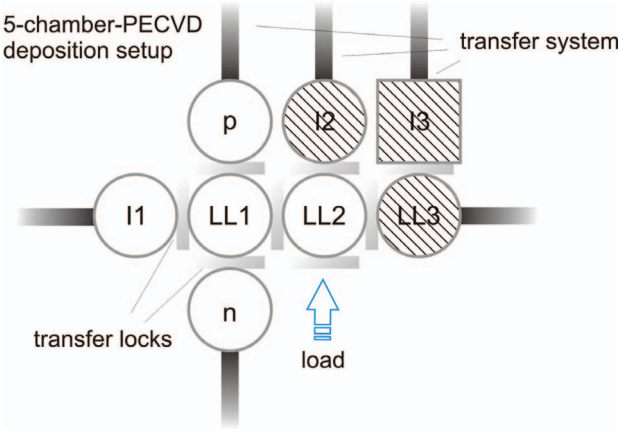


*Figure 3.1 An overview of the 5-chamber PECVD deposition system. The process chambers used in this work are I1, p, and p for the deposition of the intrinsic, p-type, and n-type silicon films, respectively. These chambers are connected via transfer locks and load locks (LL1 & LL2).*

The use of multi-chamber systems prevents cross-contamination of dopant atoms like boron into the intrinsic layers. For the fabrication of solar cells there are two chambers in which the doped layers can be produced, namely the n-chamber for n-type doping with phosphine ($PH_3$) and the p-chamber for p-type doping with trimethylboron TMB ($B(CH_3)_3$). In this study the I1-chamber was used to deposit the intrinsic absorber layer. The I2 and I3 chamber are not used in this study.

In the process chambers the base pressure before deposition is about $10^{-8}$ Torr realized by turbomolecular pumps that are series connected with rotation primary pumps. During the deposition the high-vacuum valve between reactor chamber and pumping system is closed and the unused process gases are pumped out through a bypass. The deposition pressure is regulated by a butterfly valve and a vacuum gauge (Baratron) positioned in the bypass line. All gas lines are equipped with automatic mass flow controllers (MFC). In the chamber I1 a further purification of the process gases $SiH_4$ and $H_2$ (both purity 6.0) is possible by using a gas purifier (Entegris/Aeronex CE-35KF-SK-4R) that is sketched in Figure 3.2. In the chamber I1 the process gases are feed into the plasma through a showerhead electrode which has turned out to be favorable for a homogeneous deposition of the i-layer. In the two chambers for deposition of doped layers the gases are introduced at one side of the electrode and pumped out at the opposite side below the electrode, i.e. an electrode configuration with longitudinal gas flow (not shown in Figure 3.2).

The capacitively coupled electrodes have a diameter of 13.5 cm and are separated by 10 mm, 20 mm, and 12 mm for the I1-, n-, and p-chamber, respectively. The substrate is heated by the substrate heater. Due to the low heat convection in the vacuum the heater temperature $T_H$ is approximately 3/2 of the substrate temperature $T_S$ [Rec1997]. The applied discharge power is adjusted via a matchbox to avoid power dissipation due to impedance miss-matching.

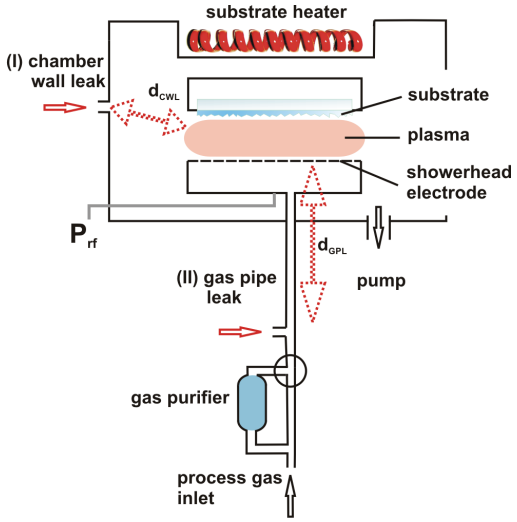


*Figure 3.2 Schematic picture of the PECVD deposition chamber (I1) used for the deposition of the intrinsic absorber layer. The two intentional leaks are (I) chamber leak and (II) gas pipe leak.*

Important special features of the PECVD chamber used for deposition of the intrinsic absorber layer in this study are the two intentional leak sources illustrated in Figure 3.2. They are situated (I) at the chamber wall (chamber wall leak, CWL) as well as (II) at the gas pipe (gas pipe leak, GPL). The leak to plasma zone distances are

approximately $d_{CWL} = 25$ cm and $d_{GPL} = 50$ cm for the CWL and for the GPL, respectively.

### 3.1.3. Deposition system II (LADA)

If not mentioned otherwise, the silicon single layers and solar cells presented in *section 8.3* are grown in the PECVD system II (von Ardenne Anlagentechnik, VAAT) that is schematically presented in Figure 3.3. The so called LADA (Large-area Deposition Apparatus) contains three deposition chambers and one load chamber that are interconnected by transport locks and an automatic substrate transport system. The LADA is also connected to the sputter deposition setup that allows to deposit, e.g., p-i-n structure and ZnO back contact without breaking the vacuum.

In this study the load chamber (LC) and the planar deposition chamber (PC1) are used to develop single-chamber processes for a-Si:H and µc-Si:H solar cells. $SiH_4$, $H_2$, $CH_4$, $CO_2$, TMB, $PH_3$, and Ar gases are connected to the PC1 chamber via MFCs. There are 9 positions for substrates of the size $10 \times 10$ cm$^2$. Alternatively, a single substrate of $40 \times 40$ cm$^2$ size can be mounted. In PC2 linear plasma sources for the deposition of intrinsic silicon layers in an inline process are installed.

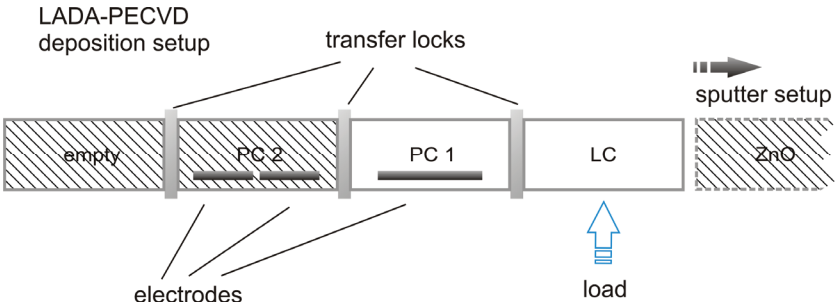


*Figure 3.3 Schematic drawing of the deposition setup LADA. The PC2 is equipped with two linear sources, PC1 is equipped with a planar plasma source.*

A detailed sketch of part of the LADA system that is used in this study is shown in Figure 3.4. In both chambers the substrate is heated by irradiation via a heater positioned behind the substrate. For a more effective substrate heating the carrier is blackened at its side in front of the heater.

In PC1 the substrate temperature $T_S$ is monitored by a pyrometer and it is controlled via a PID-controller. Thus, in contrast to deposition system I (5K), the substrate temperature is controlled with an accuracy of ± 2 °C. Both chambers are connected to vacuum pumps that allow minimum base pressures of ~ $10^{-7}$ mbar. In contrast to the other deposition system, the PC1 is pumped out directly at the plasma via turbomolecular pumps. This represents another advantage of this system over the 5K-system that might be beneficial for single-chamber processes. During the deposition the high-vacuum valve between reactor chamber and pumping system is closed and the process gas that is not used is pumped out through a bypass line by

means of a rotation primary pump. The deposition pressure is regulated by a butterfly valve and a vacuum gauge (Baratron) positioned in the bypass line.

The process gas is feed into the plasma through a showerhead electrode, no gas purifier is used. The capacitively coupled electrodes are separated by ~ 10.5 mm. The discharge power is adjusted via a matchbox in order to avoid power dissipation due to miss-matched electrical connections. Finally, the whole process is fully automated via a computer program.

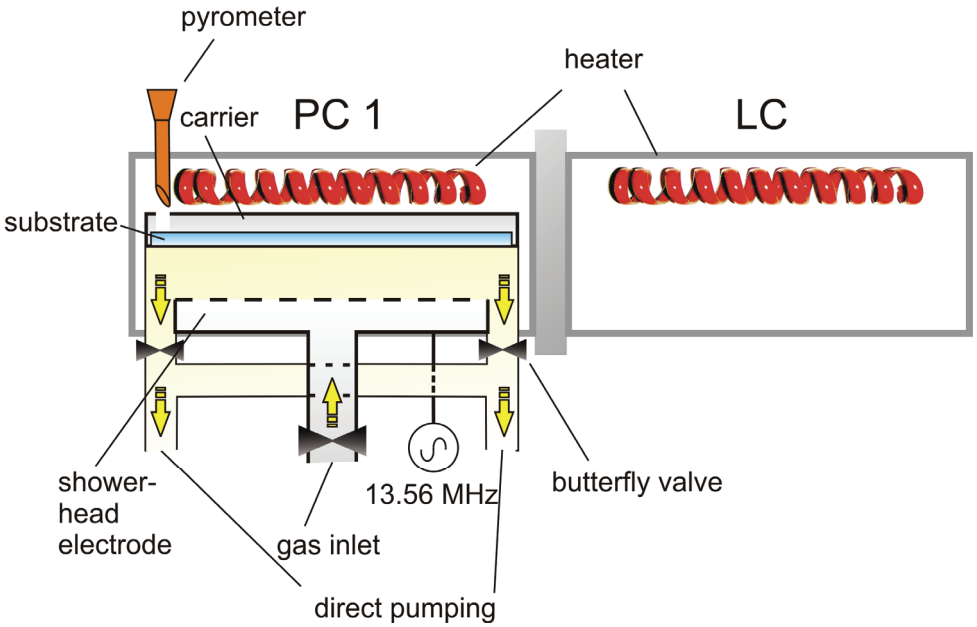


*Figure 3.4 Sketch of the deposition chamber PC1 and the load chamber (LC). The substrate temperature, established via irradiation of the resistive heaters, is measured by a pyrometer. The gas is led into the plasma through a showerhead electrode and is pumped out directly at the side of the plasma (box)*

### 3.1.4. Preparation of films and solar cells

In this section the different types of substrates that are used for material development and the individual components of complete solar cell devices in p-i-n configuration and their functions are described.

**Preparation of thin-films** For material characterization, i.e., for dark- and photoconductivity as well as for PDS and CPM measurements single a-Si:H intrinsic films are deposited on alkaline earth boro-aluminosilcate glass substrates type Eagle 2003 or 1737 supplied by Corning Incorporated. Additionally to the glass substrates, double-sided polished c-Si substrates are added for IR and/or for SIMS measurements. The intrinsic layers are deposited under the same deposition conditions as those used for the intrinsic absorber layer of the solar cells. Therefore, a

seed layer (similar to the solar cell's p-layer but without doping) is deposited just before the deposition of the a-Si:H film without breaking the vacuum.

**Solar cell design** A solar cell is built in the following way, as shown by a schematic drawing of a thin-film silicon solar cell in p-i-n configuration in Figure 3.5. Here, the light is incident from the glass (substrate) side. The light passes the transparent glass substrate coated with TCO and the p-doped layer (p-layer). Free charge carriers are generated in the subsequent intrinsic absorber layer (i-layer). The i-layer is followed by the n-doped layer (n-layer). The p- and n-layer are needed to build up the internal electric field / gradient of the quasi Fermi levels of the solar cell under irradiation. Finally, a back contact is applied which has two functions. On the one hand it serves as an electrical contact of the cells and on the other hand it is used as a so called back reflector. This back reflector increases the path length of light within the solar cell. Such a cell type is called "superstrate" or p-i-n type.

Another possibility is the "substrate" or n-i-p type, where the n-layer can be deposited on a non-transparent substrate, followed by i-layer, p-layer, and TCO. Nevertheless, also in this case the irradiation enters at the p-layer side. This is done due to the much lower mobility of holes in silicon compared to electrons. A larger fraction of the charge carriers is generated in the first part of the cell and consequently the less mobile holes have a shorter path if the irradiation is incident from the p-side of the solar cell. Solar cells in n-i-p configuration have the advantage of a larger variety of substrates (e.g. flexible substrates such as plastic foils, steel or metal) and higher process temperatures compared to p-i-n solar cells can be applied. In this study p-i-n structured solar cells are investigated, which have the advantage of a more simple production process.

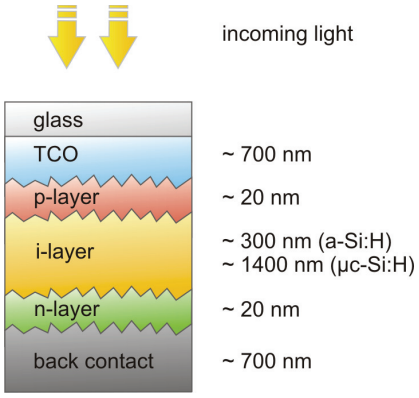


*Figure 3.5 Schematic drawing of a p-i-n structured a-Si:H or µc-Si:H single junction solar cell*

**Transparent conductive oxide** A high transparence in the wavelength range from 300 nm to 1100 nm and high conductivity to avoid ohmic losses are required for the transparent conductive oxide (TCO). In this work, commercially available Asahi

Type U ($SnO_2$:F) substrates that are optimized for a-Si:H growth are used for the deposition of amorphous p-i-n solar cells. This is equivalent to glass substrates on which a textured TCO is deposited by atmospheric pressure CVD (APCVD). The texture is needed for enhanced light-trapping and thus strong improvement of the solar cell's performance [Klu2001], [Loe1997] & [Haa2007]. For μc-Si:H solar cells in-house magnetron sputtered, aluminum doped zinc oxide (ZnO:Al) on Corning eagle 2003 or 1737 glass is used. Details of the magnetron sputtering process can be found elsewhere [Hue2005] & [Klu1996]. Then the ZnO:Al layer (800-1000 nm thick) is wet chemically etched with hydrochloric acid (0.5 % HCl solution, 40 s – 50 s etching time) to obtain a textured substrate surface. The roughness of the textured ZnO:Al substrate is slightly higher than for Asahi Type U substrates.

**Preparation of the p-layer** As a next step, the silicon p-i-n structure is deposited onto the TCO substrate via PECVD. For this the substrate is transferred into the p-chamber (5K-setup) of the deposition system / process chamber 1 (LADA-setup). To improve the temperature balance between heater and substrate an argon (5K) or a hydrogen (LADA) purge is used for some minutes. At the LADA deposition system the substrate temperature is controlled very precisely by the aid of a PID-controller and a pyrometer that monitors the substrate temperature. After the gas-purge the process gases are led into the chamber and the deposition pressure is adjusted by means of a butterfly valve. Again, for the LADA system, a temperature stabilization is performed before deposition. In contrast to the LADA system, in the 5K setup the substrate is removed from the electrode before the plasma is started and then it is moved into the plasma. After the deposition of the p-layer the flow of process gases is stopped and an Ar-purge is applied. For single-chamber processes (LADA and, in some cases, 5K), after the deposition of the p-layer a chamber cleaning process can be applied ($CO_2$ plasma, $H_2O$ purge, etc.).

For a-Si:H solar cells an amorphous p-layer is applied. For the a-Si:H p-layer wide band gap materials like silicon alloys with carbon (a-SiC:H in this work) or oxygen are used [Taw1982] & [Fuj1992]. For μc-Si:H cells a microcrystalline p-layer is applied. The structural properties of the μc-Si:H p-layer determine thi initial layer growth of the subsequent intrinsic layer. The preparation of the p-doped μ-Si:H is challenging since the material have to fulfill more requirements. On the one hand, this p-layer has to be as thin as possible and at the same time has to posses a highly crystalline structure in order to avoid carrier losses due to absorption. On the other hand the p-layer has to be thick enough (10-30 nm) to build up an efficient electric field. Furthermore, it was found that the use of trimethylboron TMB ($B(CH_3)_3$) as a doping gas deteriorates the crystalline growth and enhances the absorption [Das2000].

**Preparation of the i-layer** For the deposition of the intrinsic absorber layer the deposition procedure is nearly the same as the procedure for the p-layer except the application of doping gas. The deposition can take place in the same chamber (LADA, and in some cases, 5K) or in a special chamber used only for the deposition

of i-layers (5K). One difference between the p- and i-layer process is the option to use the gas purifier (5K). The i-layer has two important functions. First, it should absorb as much of the incident light as possible. This depends on the optical design of the device, including the thickness of the i-layer. Typical thickness values for a-Si:H solar cells range between 300 nm and 400 nm while for the μc-Si:H the thickness is much larger ~ 1.4 μm. Second, it has to provide a good electrical transport of the photo generated charge carriers, which are separated and accelerated by the electric field / gradient in the quasi Fermi levels [Wue2009]. Furthermore, since the i-layer is the thickest part of the p-i-n structure its deposition rate strongly influences the total cell deposition time. Usually, deposition rates between 0.1 – 0.5 nm/s are applied.

**Preparation of the n-layer** For all device types an amorphous n-layer is used, with $PH_3$ as doping gas. Due to its low lateral conductivity the definition of the solar cell area can be achieved only by the back contact which is prepared in a next step.

**Back contacts & annealing** There are two different types of back contacts, which can be applied to p-i-n silicon solar cells. First, contact pads of $1 \times 1\ cm^2$ can be prepared simply by thermally evaporating silver (Ag) through a shadow mask. If not mentioned otherwise the results of this study are based on solar cells with simple Ag-back contacts. Second, an additional ZnO layer is sputtered on the n-layer before the Ag evaporation takes place. Subsequently the parts that are not covered with silver are removed by wet chemical etching with HCl (0.5 %). The use of ZnO/Ag as a back reflector leads to higher short-circuit current densities $j_{SC}$ and exhibits a higher stability against thermal back-contact degradation during light-soaking experiment. The higher $j_{SC}$ can be explained by a significantly enhanced reflectivity [Spr2005].

Finally, for contact annealing the solar cells are annealed at 160 °C for 30 min before measuring their current-voltage (IV)-characteristics.

## 3.2. Material characterization

The present section deals with the main film characterizing tools that are used in this study for the investigation of the electrical-, optical-, and structural properties of the thin films.

### 3.2.1. Dark- and photoconductivity measurements

Conductivity measurements are applied to study the electrical transport in thin films. In doped or intrinsic semiconductors like a-Si:H the dark-conductivity $\sigma_{dark}$ is given by

$$\sigma_{dark} = \sigma_0 \times \exp\left(-\frac{E_A}{k_B T}\right) \tag{3.3}$$

For the pre-factor $\sigma_0$ in literature many slightly different values are reported. In this study $\sigma_0 = 150$ S/cm is set, like in the work of [Ast2009]. Now, the activation energy $E_A$ can be estimated via equation (3.3) from the measured room temperature conductivity [Str1991]. Since electrons are the excess carriers in intrinsic a-Si:H and μc-Si:H the activation energy describes the gap between the conduction band edge and the Fermi-level.

In doped material at room temperature most of the dopants are already thermally activated and excitation of charge carriers by photons does not increase remarkably the conductivity. In intrinsic material light irradiation can lead to a significant increase in (photo-) conductivity $\sigma_{photo}$ due to excitation of charge carriers from non-conductive sites to conductive sites. Additionally, the photo-generated charge carriers mainly recombine via mid-gap defect states. Thus, the photoconductivity is an indicator for the intrinsic material quality. However, in intrinsic a-Si:H the conductivity is dominated by the excess carrier density (electrons) whereas in the p-i-n solar cells both, electrons and holes, have to be extracted. A further measure for the quality of the intrinsic absorber layer is the photosensitivity $\sigma_{photo}/\sigma_{dark}$. A high photosensitivity is a necessary condition for solar grade material.

The conductivity measurements are conducted in a coplanar 2-point configuration using thermally evaporated Ag contacts ($10 \times 2$ mm$^2$) separated by a distance of 1 mm. Especially, the dark conductivity of a-Si:H at room temperature is extremely low. To prevent the measurement to be influenced, e.g., by moisture or atmospheric gasses like oxygen at the film surface all conductivity measurements are carried out under vacuum conditions ($< 10^{-6}$ mbar) and the sample is heated at 160 °C for 30 min (similar to the procedure used for solar cells). The voltage $U$ is applied by a Keithley 6517A ELECTROMETER/HIGH RESISTANCE METER, from -100 V to 100 V in 40 steps. The current $I$ is measured by the same device. For the photoconductivity measurements a halogen lamp is used which intensity is measured by a reference diode and is calibrated with respect to the AM1.5 intensity of the solar simulator. Before each measurement under illumination a time period of 3 - 5 min (under illumination) has to be passed due to the light-induced degradation, especially for amorphous silicon.

### 3.2.2. Constant photocurrent method

The constant photocurrent method (CPM), is an important tool for the determination of the optical absorption with the precondition that the product of absorption coefficient $\alpha$ and film thickness $d_{film}$ is significantly smaller than 1 [Van1981]. This requirement is fulfilled for a-Si:H in the energy range of the optical band gap. The sub-gap absorption provides information on the density of charged defects of the material. CPM reveals only relative values and thus the obtained spectra have to be calibrated, e.g., via transmission measurements.

In CPM the photocurrent $I_{photo}$ is generated by monochromatic light that is irradiated onto the film surface. This current (same contact geometry as for

conductivity measurements) depends on the generation of charge carriers, its transport and recombination, and can be expressed as

$$I_{photo} = e \times N(1-R)\left[1-\exp\left(-\alpha \times d_{film}\right)\right]\mu \times \tau \times F \times Qe \qquad (3.4)$$

where $N$ is the number of incident photons, $R$ the reflection coefficient, $Qe$ the quantum efficiency, $F$ the electrical field strength, $\mu$ the carrier mobility and $\tau$ the carrier lifetime. If $\alpha \times d_{film} << 1$ the exponential term can be simplified and the current is approximated by

$$I_{photo} = e \times N(1-R)\alpha \times d_{film} \times \mu \times \tau \times F \times Qe \qquad (3.5)$$

For amorphous silicon $R$ is assumed to be constant in the energy range of interest. Furthermore, the mobility and quantum efficiency are assumed to be the same for all wavelengths. The only energy dependent parameter is the lifetime that is proportional to the generation rate $G \sim N$. The concept of CPM is to keep the photocurrent constant which leads to an unchanged Fermi-level. Thus, the number of recombination centers can be assumed to be constant at the same time leading to a constant lifetime. With these assumptions equation (3.5) simplifies to

$$\alpha(E) \propto \frac{1}{N(E)}, \qquad (3.6)$$

and the relative absorption coefficient $\alpha(E)$ can be determined just by measuring the light intensity $\propto N(E)$ at which the photocurrent remains constant for the different photon energies. With the calibration of the spectrum the absorption coefficient of the sub-gap (< ~ 1.2 eV) can be obtained. In former studies [Rec1997] it has been shown that the absorption in the band gap can be linked to the defect density of the material. In this study the absorption coefficient at 1.2 eV times a constant factor of $2.6\times10^{16}$ $cm^{-2}$ is taken as a preliminarily value for the defect density in a-Si:H material.

Some typical CPM-spectra for uncontaminated and oxygen contaminated films with different defect densities are shown in Figure 3.6. The incorporation of oxygen is directly visible in the enhanced absorption in the sub-gap region caused by (charged) defects.

The experimental setup for CPM measurements is the same as that used for the conductivity measurements, except that a different light source is used. Additionally, a bias voltage of 100 V is applied to the sample. Instead of white light irradiation (for conductivity measurements) a monochromatic light is incident on the film. For noise reduction the light beam is chopped and a lock-in technique is applied. Furthermore, the light intensity is regulated in order to keep the photocurrent constant. Further details about the principle and experimental set-up of CPM-measurements can be found in the work of [Sie1992].

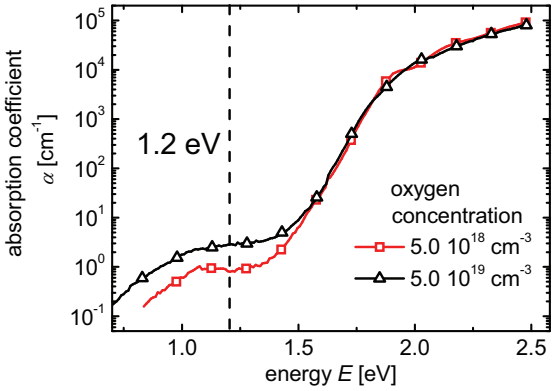


*Figure 3.6 CPM-spectra of two samples with different oxygen concentrations (deposited in the HFHP I regime). The spectra are calibrated via PDS measurements. The characteristic absorption energy of 1.2 eV from which the defect density $N_D$ can be estimated is indicated.*

### 3.2.3. Photothermal deflection spectroscopy

In addition to CPM the absorption coefficient of a-Si:H and µc-Si:H can be determined by means of photothermal deflection spectroscopy (PDS).

A schematic drawing of the PDS-principle is shown in Figure 3.7. A chopped, monochromatic light beam illuminates the film. The absorbed part of the light in the film is converted into heat, which is transported to the surrounding $CCl_4$ liquid. This liquid is transparent in the photon energy range of interest and its refractive index is highly temperature dependent. A second monochromatic light beam passes parallel to the film and its deviation due to the changed refractive index is measured. This deviation is proportional to the refractive index which is in turn dependent on temperature and, thus, on light absorption of the first light beam. By simultaneous measurement of the transmission of the sample, the interference effects due to multiple reflections at the film surface can be eliminated.

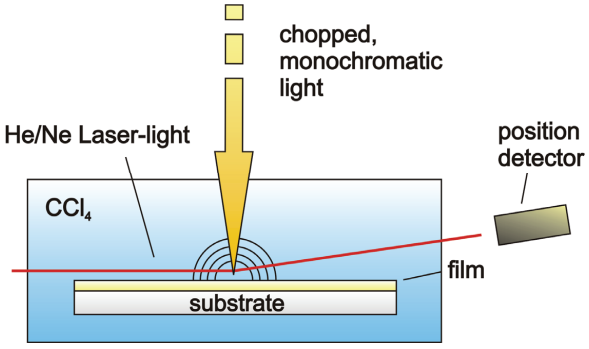


*Figure 3.7 Schematic sketch of the setup for PDS measurements used in this work. For details, see text.*

PDS provides accurate results in the high photon energy range (~ 2 eV) and, thus, the band gap $E_{04}$ of the material can be determined. The $E_{04}$-gap is determined by the photon energy at which the absorption coefficient $\alpha$ is $10^4$ cm$^{-1}$. This is illustrated in Figure 3.8. In contrast to CPM charge transport does not affect the PDS-signal. Unfortunately, it is very difficult to obtain correct defect densities from the absorption in the sub-gap absorption region (below ~ 1.5 eV) because of the sensitivity of PDS to, e.g., surface defects [Sie1997]. The PDS method is very surface sensitive while CPM is sensitive to the bulk material. For the study of the defect density CPM is used, if not mentioned otherwise.

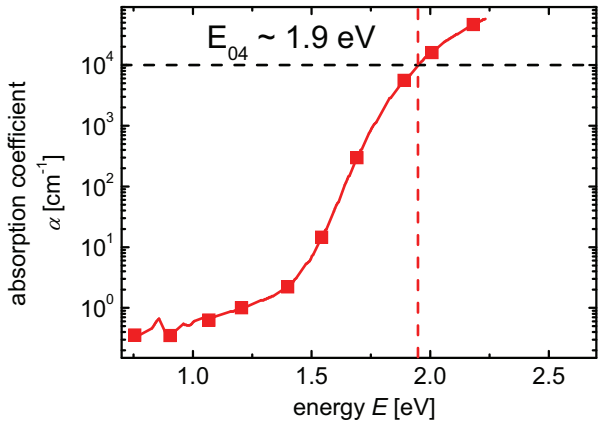


*Figure 3.8 PDS spectra of an a-Si:H films. The $E_{04}$-band gap is indicated.*

### 3.2.4. Infrared spectroscopy

Besides the optical properties of single i-layers also structural characterization is of interest for this work. Fourier transformed infrared spectroscopy (FTIR) is a powerful tool to get information about the film structure. The knowledge of the hydrogen content $C_H$ and the bonding structure of hydrogen provides important information about the material quality. Additionally, under certain restrictions, information about the oxygen concentration can be obtained from the IR spectra [Luc1983]. Furthermore, in this study a so called microstructure factor $R^*$ is determined that is an indicator for the porosity of the material. For these measurements a Nicolet Instruments Corp. Type FT-IR 740 spectrometer is used. The obtained spectra were normalized with a spectrum of a piece of a double side polished float-zone (FZ) silicon wafer taken from the same wafer that was used for the deposition of the films. The physical principle behind the FTIR method is the excitation of binding configurations in the film by irradiation with electromagnetic waves. These excitations lead to an absorption (absorption coefficient $\alpha(\omega)$), specific for the binding configuration.

**Microstructure factor $R^*$ and hydrogen content $C_H$** An absorption spectrum of an a-Si:H film intentionally contaminated with oxygen impurities is shown in Figure 3.9. The absorption peak at about $\omega = 2000$ cm$^{-1}$ represents a so called stretching mode which originates from an excitation of Si-H groups in the bulk [Bey1998]. For the peak at about $\omega = 2100$ cm$^{-1}$, Si-H$_2$ stretching oscillations at internal surfaces (voids) have to be considered which are usually not found in compact material [Mah1987]. From the relation of these two modes a so called microstructure factor $R^*$ is obtained

$$R^* = \frac{I_{2100}}{I_{2000} + I_{2100}}. \tag{3.7}$$

The integrated intensity of one oscillation mode is denoted $I_X$. For thin films this intensity has to be corrected by a factor $b$ of

$$b = \frac{1}{1.72 - 0.0011 \cdot \omega_x \cdot d_{film}} \tag{3.8}$$

if the denominator of $b$ is larger than unity [Lan1992]. A microstructure factor $R^* < 0.1$ is a good indication for high quality material. High $R^*$ values most often result from void-rich material that is not exploitable for solar cell application.

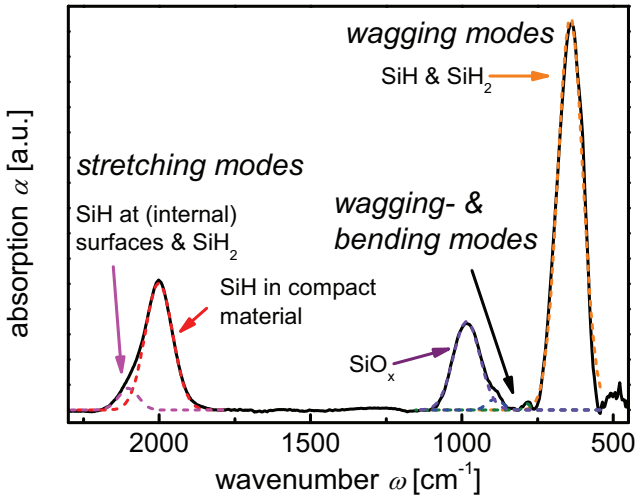


*Figure 3.9 Infrared absorption spectrum of an a-Si:H intrinsic film, contaminated with oxygen. From the absorption modes at 2000-2100 cm$^{-1}$ and at 640 cm$^{-1}$ the hydrogen content of the film is determined. High oxygen concentrations can be seen by modes in the region of 1000 cm$^{-1}$.*

Furthermore, the absorption peak at about 640 cm$^{-1}$ originates from Si-H wagging oscillations. The density of bonded hydrogen $N_H$ can be evaluated from the intensities of the wagging modes at 640 cm$^{-1}$ as well as from the stretching modes at

2000 and 2100 $cm^{-1}$, both related to Si-$H_x$ oscillations [Bey1998]. The relative amount of hydrogen $C_H$ in the film (at. %) can be derived as

$$C_H = \frac{N_H}{N_H + N_{Si}}. \tag{3.9}$$

The density of silicon is assumed to be $N_{Si} = 5\times10^{22}$ $cm^{-3}$ [Lan1992].

For the determination of the oxygen concentration a similar procedure can be applied. Here, the $SiO_x$ absorption modes are located between ~ 950 – 1050 $cm^{-1}$ [Luc1983]. Note, oxygen concentrations below 0.5 at. % exhibit very weak absorption and thus, below this limit no reliable measurement can be performed.

### 3.2.5. Secondary ion mass spectrometry

Secondary ion mass spectrometry (SIMS) is a powerful tool for detecting impurity concentrations (oxygen, nitrogen, carbide, boron, phosphorous, fluor, or iron) in silicon thin films and solar cells. For a SIMS measurement, ions ($Cs^+$) with an energy of about 6 kV are accelerated towards the film. The impinging high energy ions in turn lead to a removal of material (sputtering), i.e. secondary ions, atoms, and molecules are released from the film. The composition of the sputtered film can be analyzed be means of a mass spectrometer. To reduce the noise of the measurement ultra high vacuum conditions are necessary.

In this study the concentration of oxygen, nitrogen, carbon and boron (single chamber processes) are investigated using a quadruple instrument (Atomika 4000). The detection limits for oxygen and nitrogen are approximately $5\times10^{17}$ $cm^{-3}$ and $7\times10^{16}$ $cm^{-3}$, respectively, for a sputtering rate > 0.75 nm/s. Details of the set-up used for SIMS measurements are published elsewhere [Mue2000].

An exemplary measurement is shown in Figure 3.10. It is a measurement of a multilayer system of Si layers with different oxygen concentrations. This a-Si:H film is prepared in three steps in which different oxygen flows (base pressures) are chosen. It can be seen that the amounts of nitrogen and carbon do not increase significantly by increasing the oxygen flow. This is a necessary prerequisite for the study of contaminated i-layers. Attention has to be paid for the choice of substrates. Asahi-U and c-Si substrates give approximately the same results whereas the chemically etched ZnO:Al leads to higher impurity concentrations measured by SIMS due to its higher surface roughness [Zas2008].

For amorphous silicon films the detection of impurities is rather simple whereas for microcrystalline silicon one has to avoid post-deposition-oxidation [Smi2004]. Generally, for μc-Si:H, the more porous films tend to incorporate atmospheric contamination after deposition. Thus, there are two possibilities to prevent post-deposition-oxidation. First, the time of exposure to air has to be minimized and, second, microcrystalline films have to be covered by a compact amorphous layer. Thus, μc-Si:H solar cells with an amorphous n-layer are protected against post-oxidation.

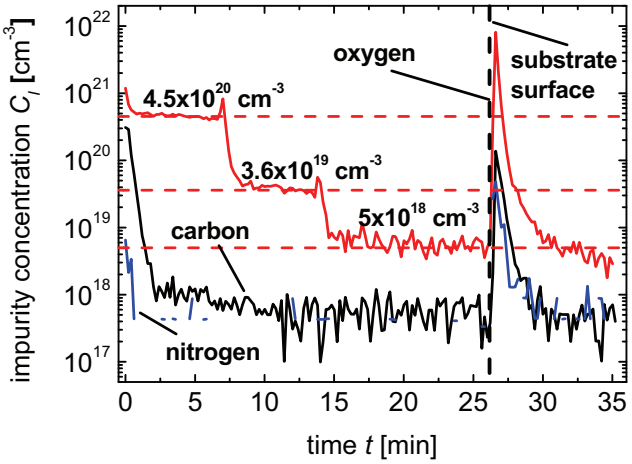


*Figure 3.10 SIMS measurement of a multilayer system containing in its first layer $5\times10^{18}$ oxygen atoms/cm$^3$, in its second layer $3.6\times10^{19}$ oxygen atoms/cm$^3$ and $4.5\times10^{20}$ oxygen atoms/cm$^3$ in its third layer. Note, that the layer which is deposited last is sputtered first by the $Cs^+$ ions. The nitrogen and carbon concentrations remain sufficiently low. The peak after 25 min originates from the float zone silicon (FZ-Si) substrate surface which is oxidized.*

## 3.3. Solar cell characterization

This section summarizes the experimental methods that are used to characterize solar cells with and without illumination.

### 3.3.1. Curren-voltage-characteristics

The IV-characteristics of the solar cells are measured by means of a class A double source WACOM-WXS-140S-Super solar simulator. The measurements are performed under standard conditions, using an AM1.5 spectrum with an intensity of 100 mW/cm$^2$ at a temperature of 25 °C. Two different types of IV-measurements are applied in this study. With the dark IV-characteristics the diode quality factor $n$ and the saturation current density $j_o$ are obtained. On the other hand the cell parameters (efficiency $\eta$, fill factor $FF$, short-circuit current density $j_{SC}$ and open-circuit voltage $V_{OC}$) are determined using IV-curves under illumination. For the properties of the solar cell under irradiation with light of short and long wavelengths, additional filters (BG7 and OG590) are applied. In this way one can study the collection of photo-generated carries close to the p/i-interface (blue light) and in the bulk of the i-layer (red light), respectively.

AM1.5 represents the simulation of the spectral distribution of sunlight that has passed 1.5 times a distance representing the thickness of the atmosphere, which is equivalent to an irradiation under an angle of 48.2 ° to the zenith at midday. An original AM1.5 spectrum and the spectrum delivered by the solar simulator are shown in Figure 3.11. The spectra of filtered light are also shown in Figure 3.11.

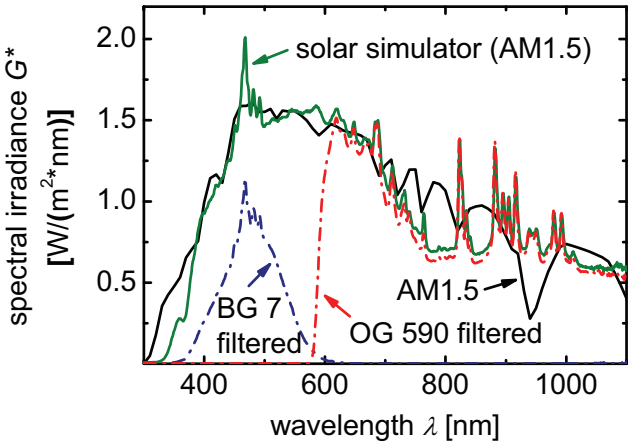


*Figure 3.11 AM1.5 spectrum of the light that has passed 1.5 times the atmosphere, i.e. simulation of solar irradiation incident under an angle of 48.2° corresponding to the zenith (black curve). The solar simulator reproduces a very similar spectrum in the important range of wavelength (green curve) which can be filtered by a BG7 band-pass filter (blue line) or an OG590 cut-on filter (red line).*

**Equivalent circuit of a solar cell** In the ideal case a solar cell can be described by a diode in parallel connection with a current generator (Figure 3.12). In reality further ohmic losses have to be considered. Bad contacts between ZnO and doped Si layers, less conductive p-layers, or the sheet resistance of the ZnO-layer have to be inserted into the model by means of series resistances $R_S$. Shunted cells lead to a very small parallel resistance $R_{SH}$ and the applied voltage leads to a current flow in parallel to the solar cell. Without illumination the current density of a solar cell as a function of the applied voltage can be described recursively in consent with the equivalent circuit in Figure 3.12 by

$$j_{dark}(U) = j_0 \cdot \left[ \exp\left( \frac{e\left(U - j_{dark}(U) \cdot R_S\right)}{nk_B T} \right) - 1 \right] + \frac{U - j_{dark}(U) \cdot R_S}{R_{SH}}. \qquad (3.10)$$

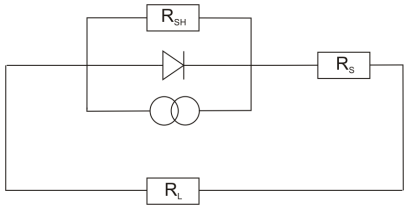


*Figure 3.12 Equivalent electronic circuit diagram of a real solar cell. The cell acts as a diode in parallel connection with a current generator (photocurrent). Unavoidable resistivity losses, i.e. in the cell connection, are taken into account by a series resistance $R_S$, and shunt losses by a parallel resistance $R_{SH}$. The load resistance $R_L$ is indicated as well.*

The first term of this equation represents the diode, the second term the shunt losses. The serial losses are included by the change in voltage which effectively is applied to the diode. $j_0$ is the saturation current density of the diode and $n$ its quality factor. The temperature is given by $T$, $k_B$ is the Boltzmann constant, $e$ is the elementary charge, and $U$ the applied voltage. In this model the value of n ranges between 1 and 2 and represents the recombination paths of the charge carriers. A diode quality factor of 2 indicates a dominant recombination in the part of the solar cell where an electric field is present, i.e. in the bulk material, whereas a diode quality factor of 1 represents a dominant diffusion path and subsequent recombination in the doped layers (no electric field) [Bra2001].

For illuminated p-n diodes the superposition principle is valid. Therefore the voltage independent photo current density and the voltage dependent dark current density, that flow in opposite directions, add up to the total current $j(U) = j_{dark}(U)+j_{photo}$ with $j_{photo} = -j_{SC}$. The short-circuit current density $j_{SC}$ is a measure for the maximum current generation in solar cells (at $U = 0$ V). Consequently, this parameter strongly depends on the amount of absorbed light, i.e. absorption coefficient, cell thickness and light-trapping. In drift controlled devices, like a-Si:H and μc-Si:H p-i-n solar cells the photo current density $j_{photo}(U)$ also dependends on the voltage as well because of the influence of the applied voltage on the internal electric field.

**Fill factor and efficiency of a solar cell** An exemplary IV-characteristic for an a-Si:H solar cell under AM1.5 illumination is shown in Figure 3.13. The solar cell IV-characteristic under illumination is described by a set of parameters which will be introduced in the following. The maximum power density $P_{max} = j_{max}\ U_{max}$ generated by this cell defines the efficiency $\eta = P_{max} / P_{solar\ simulator}$. The open circuit voltage $V_{OC}$ represents the maximum voltage generated by the cell by means of the internal field, i.e. $j(V_{OC}) = 0$ mA/cm² .

A further descriptive parameter for the solar cell quality is defined as the fill factor $FF$ ("rectangularness" of the IV-characteristic under illumination at the maximum power point MPP) giving the ratio of $P_{max}$ and the power output corresponding to $j_{SC}\ V_{OC}$ (dashed rectangle)

$$FF = \frac{j_{\max} \cdot V_{\max}}{j_{SC} \cdot V_{OC}} = \frac{P_{\max}}{j_{SC} \cdot V_{OC}}. \qquad (3.11)$$

The fill factor $FF$ of a solar cell describes the collection efficiency of charge carriers [Rec1998]. The efficiency can also be expressed in terms of $FF$ by the commonly used formula:

$$\eta = \frac{FF \cdot j_{SC} \cdot V_{OC}}{P_{sun\ \ simulator}} \qquad (3.12)$$

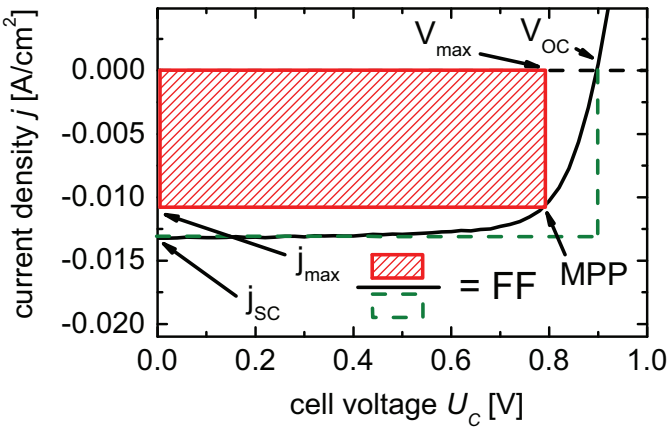


*Figure 3.13 IV-characteristic of an a-Si:H solar cell under illumination. The short circuit current density $j_{sc}$, the open circuit voltage $V_{oc}$, and the fill factor FF are indicated. The current density, the voltage, and the power of the maximum power point MPP are given as well.*

### 3.3.2. Quantum efficiency

A detailed insight into the optical absorption and spectral information of the charge carrier extraction of solar cells is given by spectral resolved quantum efficiency measurements. The quantum efficiency $QE(\lambda)$ describes the probability of a photon of a certain energy to create free charge carriers contributing to the photo current and is given by

$$QE(\lambda) = \frac{j_{photo}(\lambda)}{e \cdot \Phi(\lambda)}. \qquad (3.13)$$

In this equation $j_{photo}(\lambda)$ denotes the photo current density (wavelength dependent) and $\Phi(\lambda)$ the photon flux per unit time, area, and wavelength, respectively. By converting this equation to $j_{photo}(\lambda)$ and by integrating over all wavelengths $j_{SC}$ can be obtained.

In order to use the lock-in technology, experimentally, the solar cell is illuminated with a chopped monochromatic light beam. QE-measurements can also be performed under a bias voltage in order to superimpose an external and the internal electric field. Forward bias conditions lead to measured *QEs* close to the working conditions of the solar cell. A reverse bias reduces the charge carrier recombination and, thus, increases the charge carrier collection. For a high reverse bias voltage all generated charge carriers can be extracted from the solar cell. Finally, a supplementary AM1.5 like bias light can be used in order to saturate defects and extract all generated charge carriers. This is a measurement under intensive light irradiation conditions that is possible due to the lock-in technology. More details of the physical and experimental background can be found in [Met1987] & [Wit1988].

For multijunction solar cells the *QE* of each subcell can be measured separately, i.e. the measurement is based on the series connection of the subcells. All cells are saturated via bias illumination of appropriate wavelengths, except for the subcell of interest. The subcell with the lowest current density, i.e. the only subcell not absorbing in the bias light wavelength range, defines the overall current density. A survey on the spectral response measurements of tandem solar cells is given in [Sch1994].

### 3.3.3. Light-soaking

A serious challenge for a-Si:H solar cells is given by their controversially discussed metastability. Under light irradiation weak bonds tend to break up and create defect states located in the mid-gap, i.e. dangling bonds. This is called Staebler-Wronski effect (SWE) and leads to an undesired decrease of the solar cell efficiency during the exposure to light [Sta1977].

To investigate the long-term stability of solar cells they are illuminated for up to 1000 h under standard conditions, i.e., the solar cells are exposed to an AM1.5 like spectrum of 100 mW/cm² at a temperature of 50 °C. The temperature is chosen according to the general working temperature of solar cells. Furthermore, the cell is light-soaked under open-circuit conditions where generation and recombination rates of the charge carriers are equal. In this way, the degradation behavior of many years of a solar cell under real conditions is simulated in a short time period.

# 4. Atmospheric contamination of a-Si:H films and solar cells

In this chapter the focus is on the influence of atmospheric contaminants (oxygen and nitrogen) on electrical, optical, and structural properties of intrinsic a-Si:H thin-films, and their influence on the performance of p-i-n solar cells, in the initial and degraded states. Therefore, an oxygen, nitrogen, or air leak is simulated by means of a controllable leak at the wall of the recipient. A part of the incorporated oxygen and nitrogen is found to act as donors that shift the Fermi-level towards the conduction band. This effect reduces the performance of solar cells if a critical impurity concentration is exceeded. For an oxygen leak a critical oxygen concentration of $C_{O,crit} = 2\times10^{19}$ cm$^{-3}$ in the i-layer is found, for nitrogen the critical concentration is $C_{N,crit} = 4\times10^{18}$ cm$^{-3}$. The critical concentrations do not change upon light soaking. For an air leak it is shown that, even though the nitrogen content in air is higher than the oxygen content, predominantly oxygen incorporation is decisive for the cell deterioration. Note, $C_{O,crit}$ is approximately one order of magnitude higher than $C_{N,crit}$. It is also shown, that close to the i/n-interface a concentration higher than the critical impurity concentration $C_{I,crit}$ can be tolerated in the i-layer. Close to the p/i-interface the critical impurity concentrations in the i-layer are at the above mentioned values.

## 4.1. Introduction

In general, in a-Si:H p-i-n solar cells the device quality is known to depend strongly on the properties of the intrinsic absorber layer (i-layer). In the recent years it has been seen that high efficiency a-Si:H and μc-Si:H solar cells require a very low incorporation rate of impurities like, e.g., oxygen and nitrogen during the deposition of the i-layer [Mor1991], [Rec1998]. For example, in [Tor1998] it has been shown that the cell performance in the red wavelength range can be significantly increased by a decrease of the oxygen concentration in the solar cell, achieved by means of a process gas purifier.

Accompanied to studies of contaminated solar cells material studies indicate that oxygen as well as nitrogen have an impact on the electrical and structural properties

of a-Si:H thin films. For oxygen and nitrogen contamination an increase in dark- and photoconductivity [Mor1991] & [Shi1991] as well as in dangling-bond density [Stu1985] is observed.

Morimoto et al. [Mor1991] and Shimizu et al. [Shi1991] developed a model describing the incorporation of oxygen and nitrogen into the i-layer based on conductivity and electron spin resonance (ESR) measurements. The impurities are assumed to lead to donor-like states, shifting the Fermi level towards the conduction band. Post-transit photocurrent spectroscopy of a-Si:H films showed that oxygen donors have to be located at energy levels lower than 0.35 eV below the conduction band edge [Sak2007].

Sources for atmospheric contamination were investigated by Kroll et al. [Kro1994] & [Kro1995] for the deposition of a-Si:H via a 70 MHz PECVD process. In their work they defined two classes of contamination, namely intrinsic and extrinsic contamination sources. Intrinsic contamination is defined as impurities brought into the process by means of contaminated process gas. The process gas can be contaminated due to air leaks of the process gas supply line or leaky MFCs. However, even if there are no real air leaks, in the $SiH_4$ or $H_2$ gas-bottles as well as in the gas supply system are always low concentrations of impurities. The intrinsic contamination of the process gas can be reduced by the application of a gas purifier. Note, a gas purifier only reduces the intrinsic oxygen concentration but not the intrinsic nitrogen concentration.

Extrinsic contamination is defined as contamination that is brought into the process by the recipient. Apparently, an extrinsic impurity source is given by a leak of the recipient. Furthermore there are plenty of virtual chamber leaks that are difficult to avoid. For example, there is outgassing of atmospheric contaminants from the reactor walls. This impact can be reduced by heating up the reactor in order to dissolve as much as possible impurities from the reactor walls. Prior to the deposition of the i-layer the temperature is reduced to the deposition temperature that is needed for high-quality absorber layers. A further extrinsic contamination source is given by the residual gas in the reactor. An indicator for the quantity of contamination from residual gases is given by the base pressure of the recipient. In large-area industrial deposition systems, the incorporation of residual gases is usually higher than in small-area research deposition systems due to a higher base pressure [Rec1998].

Furthermore it has been observed by Kroll et al. [Kro1994] & [Kro1995] that also the deposition conditions influence the incorporation of impurities. A high deposition rate, e.g., achieved via high discharge powers leads to a significant reduction of the oxygen incorporation into a-Si:H. In contrast, the nitrogen incorporation rate is not influenced by the deposition rate. Based on these findings, they suggested a direct oxygen incorporation into the growing film, independent on the discharge power. They assumed nitrogen to be incorporated indirectly, i.e. via gas phase reaction with $SiH_4$ and subsequent incorporation of the nitrogen containing film precursor.

This chapter addresses the influence of oxygen, nitrogen, and air leaks, during the deposition of the i-layer, on the solar cell and material characteristics of a-Si:H. Here, the focus is on the question to what degree high-quality a-Si:H solar cells can be produced under high base pressure conditions. The contaminating gas oxygen, nitrogen, and air were provided to the deposition chamber through a needle valve at a chamber wall (extrinsic contamination), simulating chamber leaks and the outgassing process. The solar cell parameters and material properties for various nitrogen or oxygen concentrations in the i-layer were compared for the different impurities.

## 4.2. Intentional impurity flows & impurity concentrations in the i-layer

For the investigation of the impact of impurities on the solar cells parameters, first, impurity flow rates during deposition and the impurity concentration homogeneity in the i-layer have to be determined. This is described in the following two subsections.

### 4.2.1. Regulation of the intentional impurity flow

In this section the regulation of the intentional impurity flows into the recipient is explained. Due to very small flow rates of oxygen, nitrogen (both purity 5.0), or air their gas flow can not be controlled by MFCs. In this study a measure for the impurity flow is the base pressure $p_b$ prior to deposition that is increased by the leak flow.

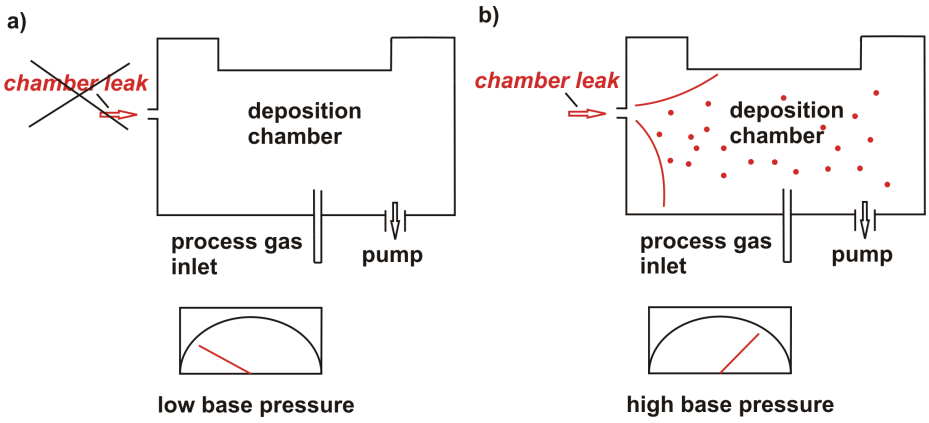


*Figure 4.1 Deposition chamber (I1) without intentional chamber leak (a). The base pressure is low at about $10^{-8}$ Torr. In (b) an intentional leak flow is applied through a needle valve leading to a higher base pressure in the process chamber. Note that no process gases ($SiH_4$ and $H_2$) flow in both cases during the adjustment of the impurity flow.*

Figure 4.1 illustrates the principle of the leak flow regulation in case of the controllable chamber wall leakage. A low base pressure of ~ $10^{-8}$ Torr before deposition proves the low outgassing rate of the system, which is of importance [Kro1995]. It can be concluded that our PECVD deposition chamber meets high purity requirements which are needed as a starting point for our experiment. A metal needle valve is used to control the contaminants flow of oxygen, nitrogen, or air into the chamber while the turbomolecular pump is still connected to the recipient. Due to the impurity flow the pressure in the chamber rises to a now enhanced impurity caused base pressure $p_b$. For the deposition of the i-layer the impurity flow is not changed from this moment on, process gases are added and the deposition pressure is established.

### 4.2.2. Impurity concentration homogeneity

In 3.2.5 the principle of the impurity concentration measurement (SIMS) is explained. However, it turns out that for the application of a chamber wall leak (CWL) the distribution of the impurity concentration is inhomogeneous over the cell area.

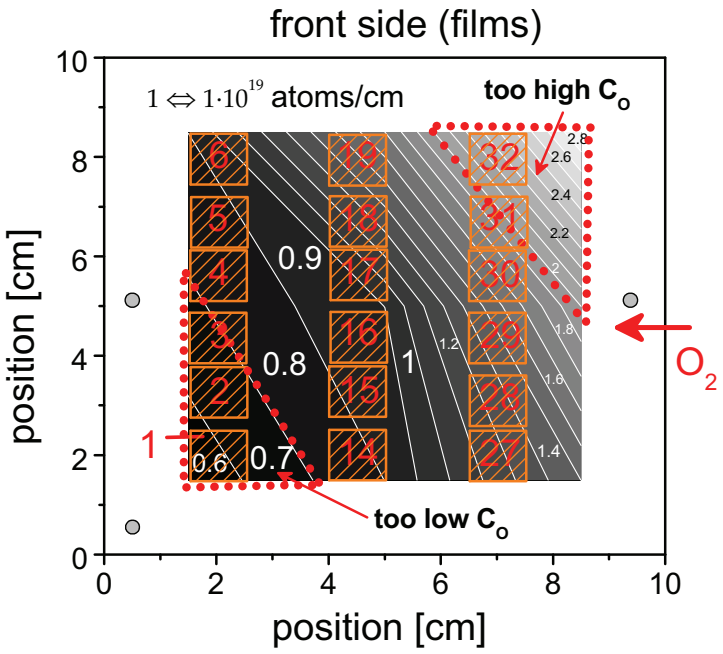


*Figure 4.2 Contour plot of oxygen concentration for a film contaminated with the CWL. The sample is shown from the film side. The position at which the solar cells generally are characterized, are shown by the orange squares and the red numbers within. The white numbers aside symbolize the amount of oxygen relative to a concentration of $10^{19}$ $cm^{-3}$. Cell positions 31 and 32 should not be used due to a too high oxygen concentration and cell positions 1-4 should not be used due to a too low concentration of oxygen compared to the cell average.*

Figure 4.2 represents a contour plot of the distribution of oxygen in the case of the CWL. $X$ and $Y$ represent the position of the film (seen from the front side) in the chamber, the oxygen penetrates from the wall at position $X = 10$ cm and $Y = 5$ cm. The solar cell numbers (1-32) indicate the position of the solar cells that are characterized by means of the solar simulator. From the 18 cells, defined by the back contacts, cells 1-4 should not be used due to a too low impurity concentration compared to the cell average. In contrast far above the average and therefore out of focus are cells 31 and 32. For the other solar cells the oxygen incorporation homogeneity is within the SIMS accuracy.

## 4.3. Process conditions for the i-layer

All i-layers of the solar cells were deposited in the so-called high-flow high-pressure I regime (HFHP I), which is characterized by a deposition gas flow of ~ 370 sccm ($SiH_4/H_2$ of 7.8/360 sccm) and a deposition pressure of 10 Torr at a heater temperature $T_H$ of ~ 200 °C (~ 3/2 $T_S$). The applied discharge power was ~ 0.2 W/cm², yielding a deposition rate of ~ 0.5 nm/s. The applied intentional and variable leak was situated at the deposition chamber wall (chamber wall leak, CWL).

## 4.4. Correlation of base pressure and impurity concentration

Here, the correlation of the impurity flow, given by the base pressure, and the impurity concentration in the absorber layer is studied. This relationship is a measure for the impurity incorporation probability of the corresponding contamination species (oxygen and nitrogen). Figure 4.3 shows the impurity concentration of a-Si:H absorber layers as a function of the base pressure controlled by nitrogen, oxygen and air-leaks. In order to keep the deposition conditions as constant as possible, this study was performed on a multilayer film structure (see Figure 3.10) i.e. a multilayer system composed of i-layers deposited at 3 - 5 different contamination flows. The base pressure was varied from $10^{-8}$ to $10^{-4}$ Torr.

The general trend of the correlation of base pressure and impurity concentration is independent on the impurity species (oxygen and nitrogen). For an increasing base pressure the impurity concentration increases as well. This increase is stronger the higher the base pressure.

| | $C_{crit}$ [cm$^{-3}$] | $p_{b,crit}$ [Torr] |
|---|---|---|
| oxygen | $2\times10^{19}$ | $7\times10^{-6}$ |
| nitrogen | $4\times10^{18}$ | $1\times10^{-5}$ |
| air | $1.7\times10^{19}$ (O)/$1.7\times10^{18}$ (N) | $8\times10^{-6}$ |

*Table 4.1 Critical concentration and critical base pressure for oxygen and nitrogen contamination. For the air leak the critical base pressure and the corresponding oxygen and nitrogen concentrations are given.*

From the solar cell parameters of contaminated solar cells (see *section 4.5*) the critical base pressures and impurity concentrations that lead to a decreased solar cell performance, if exceeded, are known. The critical oxygen and nitrogen concentrations are $2\times10^{19}$ atoms/cm$^3$ and $4\times10^{18}$ atoms/cm$^3$, respectively, see Table 4.1. The critical base pressure for the air leak is indicated in the figure by the dashed vertical line at ~ $8\times10^{-6}$ Torr. Furthermore, from the figure it can be concluded that the oxygen incorporation probability is approximately one order of magnitude higher compared to that for nitrogen. Thus, for a given base pressure the impurity concentration is about 10 times higher for oxygen compared to nitrogen. From Figure 4.3 it is seen that this relation does not change significantly over the whole pressure range. Note, at the same time the solar cell deterioration is found to start at a ~ 10 times higher oxygen concentration compared to that for nitrogen. The two inversely acting effects of incorporation probability and critical impurity concentration lead to the surprising result of a very similar critical base pressure in the range of ~ $10^{-5}$ Torr for oxygen, nitrogen, and air leaks for this deposition regime, see also *section 4.5*.

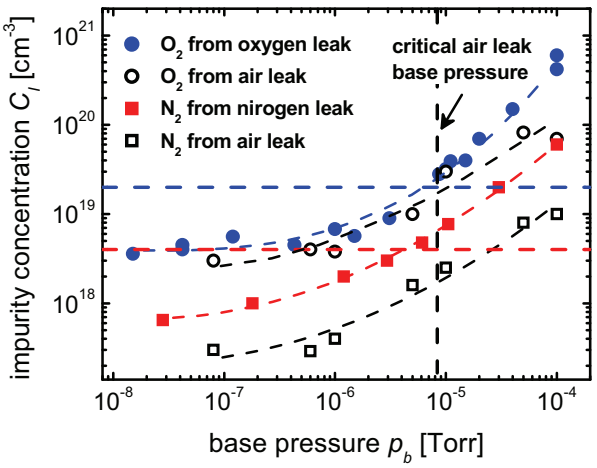


*Figure 4.3 Impurity concentration in the i-layer as a function of the base pressure for oxygen, nitrogen and air contaminated a-Si:H deposited in the HFHP I regime. The critical nitrogen (horizontal red dashed line) and oxygen (horizontal blue dashed line) contamination levels determined from the fill factor under red illumination (see Figure 4.4) are indicated. For the air leak, the critical base pressure is indicated at ~ $8\times10^{-6}$ Torr by the vertical dashed line.*

For the air-leak, surprisingly, the critical oxygen contamination level in the intrinsic layer is reached first. This is caused by the fact that at the critical air leak base pressure the amount of oxygen in the i-layer is at least about one order of magnitude higher than the amount of nitrogen. This aspect is discussed later.

## 4.5. Solar cells based on contaminated i-layers

In order to study the impact of oxygen and nitrogen (via CWL) on complete p-i-n a-Si:H solar cells, cells with intentionally contaminated i-layers are prepared. As already mentioned in *section 4.4* these solar cells show a critical impurity concentration. The levels are $C_{O,crit} = 2\times10^{19}$ cm$^{-3}$ and $C_{N,crit} = 4\times10^{18}$ cm$^{-3}$ for oxygen and nitrogen incorporation, respectively. Above these concentrations the cell efficiency $\eta$ and the fill factor *FF* under AM1.5 and red light illumination decrease. Cells contaminated via air leak deteriorate mainly due to oxygen incorporation.

### 4.5.1. Oxygen & nitrogen leak

Figure 4.4 shows the important parameters obtained by measurements of the initial solar cell parameters (i.e., efficiency $\eta_{ini}$ (a), fill factor *FF* (b) and short-circuit current density $j_{SC}$ under red illumination (c) and the open-circuit voltage $V_{OC}$ (d)) as a function of oxygen and nitrogen concentration (closed symbols).

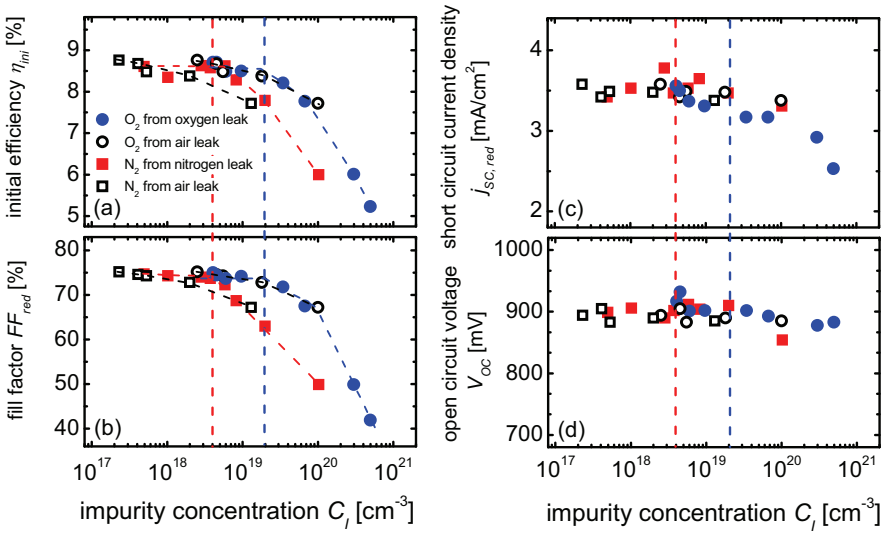


*Figure 4.4 Initial solar cell parameters of p-i-n a-Si:H solar cells deposited in the HFHP I regime as a function of the impurity concentration in the i-layer contaminated by admitting oxygen (blue symbols), nitrogen (red symbols), and air (open symbols) to the deposition process. The dashed lines are guides for the eye. For nitrogen the critical contamination levelt is $4\times10^{18}$ atoms/cm$^3$ and for oxygen it is $2\times10^{19}$ atoms/cm$^3$. The oxygen and nitrogen concentrations obtained from SIMS depth profiles of cell contaminated by an air-leak are shown by the open symbols.*

Below a critical impurity concentration level of $C_{O,crit} = 2\times10^{19}$ cm$^{-3}$ or $C_{N,crit} = 4\times10^{18}$ cm$^{-3}$ the solar cell parameters are not significantly affected. State-of-the-art solar cells can be grown with impurities in the i-layer reaching these concentrations. Exceeding the critical impurity concentration the initial efficiency of solar cells decreases with increasing impurity concentration (oxygen and nitrogen).

Note that the average oxygen concentration for intentionally nitrogen contaminated films is 5-7×$10^{18}$ $cm^{-3}$ and an average nitrogen concentration of 5-7×$10^{17}$ $cm^{-3}$ is observed for cells that are contaminated by means of an oxygen leak.

The critical concentrations can be determined from the initial solar cell efficiencies, but even more sensitively from the fill factor under red illumination versus i-layer impurity concentration since the fill factor is extremely sensitive to the incorporation of defects, donators and acceptors in the bulk material (i-layer) [Rec1998]. Therefore, the critical contamination levels for oxygen and nitrogen are determined from the fill factor under red illumination.

However, there is not a unique criterion for the fill factor under red illumination indicating a bad solar cell. For example, the fill factor of nominally uncontaminated cells depends on the deposition regime. For this study, a fill factor under red illumination of 74 - 75 % is found for uncontaminated solar cells. A drop of this *FF* below 73 % can be taken as an indicator for the onset of solar cell deterioration.

For oxygen contamination resulting from a controllable oxygen leak the solar cell deterioration starts with a slight red fill factor reduction above the critical level of ~ 2×$10^{19}$ oxygen atoms/$cm^3$. Above an oxygen concentration of about $10^{20}$ atoms/$cm^3$, the solar cell quality decreases drastically. For nitrogen contamination resulting from a controllable nitrogen leak the fill factor under red illumination starts to decrease when exceeding a concentration of ~ 4×$10^{18}$ atoms/$cm^3$. The critical level is approximately one order of magnitude lower for nitrogen compared to oxygen.

In related studies of the atmospheric contamination of hydrogenated microcrystalline silicon (μc-Si:H) deposited under conditions similar to the applied deposition regime (HFHP I), similar critical levels have been found, namely 1 - 2×$10^{19}$ atoms/$cm^3$ for oxygen and 6 - 8×$10^{18}$ atoms/$cm^3$ for nitrogen [Kil2009].

In the HFHP I regime, for uncontaminated solar cells values of $j_{SC}$ ~ 13 mA/$cm^2$, $j_{SC,\,red}$ ~ 3.5 mA/$cm^2$, and $V_{OC}$ ~ 900 mV are obtained. The $V_{OC}$ does not change upon contamination, whereas $j_{SC,\,red}$ decreases slightly for increasing oxygen and nitrogen concentration. In contrast, for μc-Si:H the short circuit current density $j_{SC}$ is strongly affected by oxygen incorporation (see *chapter 6* & [Kil2009]).

### 4.5.2. Air leak

In addition to contamination studies with intentional (molecular) oxygen and nitrogen leaks the effect of an air leak is studied as a function of oxygen and nitrogen concentration, respectively. This is also included in Figure 4.4 (open symbols). For the HFHP I regime, the solar cell parameters as a function of the oxygen concentration in the i-layer are nearly the same as for solar cells contaminated only via an oxygen leak. Furthermore, these solar cells show a reduction in performance for nitrogen concentrations below the critical level as demonstrated for contamination with nitrogen only. Thus, in this case the solar cell deterioration seems to be caused primarily by oxygen incorporation from air.

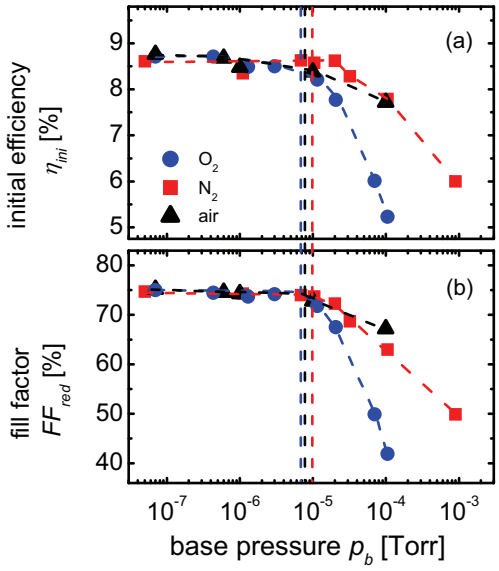


*Figure 4.5 Initial efficiency (a) and fill factor under red illumination (b) as a function of the base pressure varied by a controllable oxygen, nitrogen, or air leak for the same set of solar cells as used in Figure 4.4. The critical oxygen (blue vertical dashed line) and nitrogen (red vertical dashed line) contamination levels are indicated as well as the critical air base pressure (black vertical dashed line).*

Note, the oxygen concentration (~ $2\times10^{19}$ $cm^{-3}$) at which the cell deterioration of the cells contaminated via air leak starts is approximately one order of magnitude higher than the nitrogen concentration (~ $4\times10^{18}$ $cm^{-3}$). At the same time the oxygen content in air is four times smaller than the nitrogen content. Apparently, the incorporation probability of oxygen is significantly higher for oxygen compared to that for nitrogen. Note, if not mentioned otherwise the impurity incorporation probability is defined as the amount of impurities introduced into the reactor compared to the impurity concentration found in the i-layer. Nevertheless, it cannot be excluded that there is an interaction between oxygen and nitrogen, e.g. a formation of doping complexes. An opposite behavior was seen for μc-Si:H solar cells that are contaminated via a chamber wall air leak [Kil2009]. In that study, the cell deterioration was mainly caused by the incorporation of nitrogen.

For industrial applications it might be of interest to determine the critical flow rates of oxygen, nitrogen, and air leaks, respectively. The base pressures are used as a measure for the leak flow rate, since the leak flows are difficult to be measured directly. It should be remarked that this base pressure depends on the pumping configuration but in general, it is possible to link it to the leak flow rate. For this setup, the critical base pressures are ~ $7\times10^{-6}$ Torr and ~ $1\times10^{-5}$ Torr, for oxygen and nitrogen, respectively, whereas an intermediate value of ~ $8\times10^{-6}$ Torr is measured for air, see Table 4.1. Assuming a similar pump rate for nitrogen and oxygen, similar critical oxygen, nitrogen or air-leak flows lead to solar cell deterioration for the

HFHP I regime, see Figure 4.5. This is a remarkable result but can be explained by a compensation of different doping efficiencies and incorporation probabilities for oxygen and nitrogen, respectively.

## 4.6. Material properties

In this section the electrical, optical, and structural properties of a-Si:H intrinsic films are investigated as a function of the impurity concentration. E.g., a doping effect of the impurities should be reflected by the electrical properties of the i-layer. Also, structural changes of the intrinsic material by impurity incorporation are of interest. The question is addressed if the critical impurity concentrations observed for contaminated solar cells are seen for the material properties as well.

For films exceeding the critical impurity concentration (oxygen or nitrogen) an increase in dark $\sigma_{dark}$ and photoconductivity $\sigma_{photo}$ is observed as well as a decrease in activation energy $E_A$. This is caused by an upward shift of the Fermi level due to the doping effect of the incorporated impurities. This effect is similar for oxygen and nitrogen except for the absolute values of the concentrations. In contrast, oxygen concentrations above ~ $10^{20}$ $cm^{-3}$ lead to an increased band gap $E_{04}$ and to a reduced conductivity. This can be explained by the onset of (measurable) alloying. For nitrogen no such effect is observed for the nitrogen flows that are possible to apply with the deposition setup.

### 4.6.1. Electrical properties

The dependence of activation energy $E_A$, dark- and photoconductivity $\sigma_{dark}$ and $\sigma_{photo}$, and photosensitivity $\sigma_{photo}/\sigma_{dark}$ on oxygen and nitrogen concentration is given in Figure 4.6 (a–c). Nominally uncontaminated i-layers show $\sigma_{dark}$ of ~ $10^{-11}$ S/cm, $\sigma_{photo}$ of ~ $10^{-5}$ S/cm, and $E_A$ ~ 0.77 – 0.80 eV, that are values that are commonly found for state-of-the-art solar cell i-layers.

For the series prepared with a controllable oxygen leak at the reactor wall, the dark- and photoconductivity increase when the oxygen concentration exceeds $2\times10^{19}$ atoms/$cm^3$, and drop at oxygen concentrations higher than $2\times10^{20}$ atoms/$cm^3$. $E_A$ decreases from ~ 0.8 eV for uncontaminated films to a minimum of ~ 0.7 eV for contaminated films. At oxygen concentrations higher than $2\times10^{20}$ atoms/$cm^3$ an increase in $E_A$ is observed.

By increasing the nitrogen concentration from $5\times10^{17}$ to $1\times10^{20}$ atoms/$cm^3$, dark- and photoconductivity start to increase and might increase slightly stronger when the nitrogen concentration level exceeds ~ $4\times10^{18}$ atoms/$cm^3$. For nitrogen, $E_A$ decreases from ~ 0.77 eV for uncontaminated films to ~ 0.66 eV for contaminated films. However, for nitrogen the correlation between critical concentration and electrical properties is much weaker compared to that for oxygen. Furthermore, for nitrogen, no drop in conductivity or increase in $E_A$ is observed in contrast to oxygen. However, the same behavior is expected to occur also at higher nitrogen

concentrations but this concentration range is not accessible in the deposition setup used.

Comparing oxygen and nitrogen incorporation it stands out that the dependence of the electrical parameters on the impurity concentration is similar for oxygen and nitrogen contaminated films and is only different in absolute values of concentration.

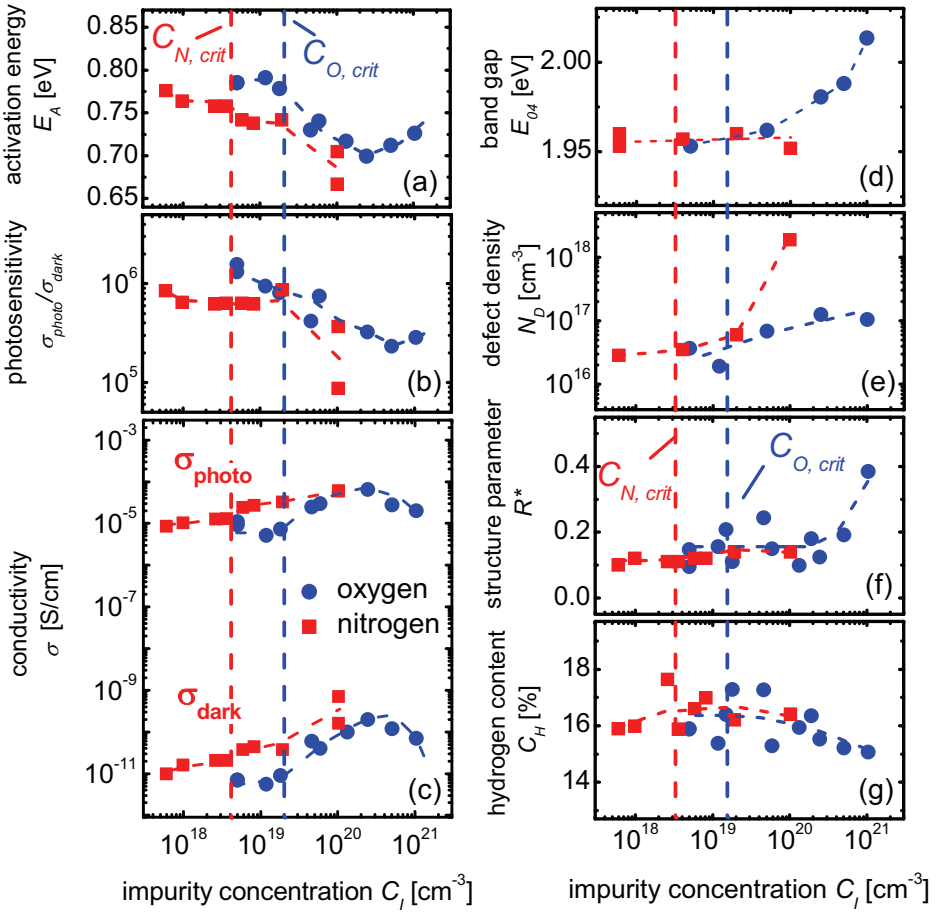


*Figure 4.6 Electrical properties (activation energy $E_A$, photosensitivity $\sigma_{photo}/\sigma_{dark}$, and photo- and dark-conductivities $\sigma_{photo}$ and $\sigma_{dark}$ (a-c)), optical properties (mobility band gap $E_{04}$ and defect density $N_D$ (d,e)) and structural properties (microstructure factor R* and hydrogen content $C_H$ (f,g)) as a function of impurity concentration in the intrinsic a-Si:H films that is varied by the oxygen flow (blue circles) or by the nitrogen flow (red squares) into the deposition chamber. The two dashed lines represent the critical nitrogen (red line) and oxygen (blue line) contamination level for the solar cell performance of $4\times10^{18}$ atoms/cm$^3$ and $2\times10^{19}$ atoms/cm$^3$, respectively. The dashed lines connecting the data points are guides to the eye*

### 4.6.2. Optical properties

Figure 4.6 (d) shows the $E_{04}$ band gap values as a function of the impurity concentration. These data were determined from PDS spectra of the corresponding films. For increasing impurity concentration the $E_{04}$-gap of about 1.96 eV keeps constant for oxygen and nitrogen contaminated films up to a concentration of ~ $10^{20}$ atoms/cm$^3$. For oxygen concentrations > $2\times10^{20}$ atoms/cm$^3$ (i.e., > 0.4 at. %) the band gap increases by some tens of meV. This is assumed to be the onset of (measurable) alloying, i.e. the formation of $SiO_2$ in a significant concentration in the amorphous matrix. This would be in a good agreement with the decreasing dark conductivity as well as the increase of the activation energy in the alloying range shown in Figure 4.6 (a, c). Furthermore this supports the assumption that it is not p-type doping for high oxygen concentrations leading to a decrease in, e.g., dark conductivity.

In Figure 4.6 (e) the defect density $N_D$ of the i-layer is shown as a function of the impurity concentration. The defect density is determined from the mid-gap absorption measured by CPM. An increase in defect density from $2 - 3\times10^{16}$ cm$^{-3}$ to ~ $10^{17}$ cm$^{-3}$ and ~ $10^{18}$ cm$^{-3}$ is seen for oxygen and nitrogen, respectively, for an increasing impurity concentration.

### 4.6.3. Structural properties

Infrared measurements are used to obtain information about the film structure. The microstructure factor $R^*$ and the hydrogen content $C_H$ of single i-layers, that are intentionally contaminated by oxygen and nitrogen impurities, are shown in Figure 4.6 (f, g).

For all nitrogen and low oxygen concentrations (until $2\times10^{20}$ atoms/cm$^3$) the $R^*$ values range between 0.1 and 0.2. Generally, $R^*$ represents the relative amount of IR-modes of Si-$H_2$ at 2100 cm$^{-1}$, located at (internal) surfaces, compared to Si-H modes at 2000 cm$^{-1}$ (bulk). A high value of $R^*$ implies a void-rich structure. However, the strong increase of $R^*$ up to 0.4 at high oxygen concentrations is probably not originated by a void-rich film structure. It probably has to be accorded to Si-H modes that can also be shifted from 2000 cm$^{-1}$ to higher wave numbers due to oxygen that is back-bonded to Si-H groups [Luc1983]. The latter leads to incorrect interpretation of $R^*$ values at high oxygen concentrations. The hydrogen concentration in the i-layer is in the range of 15 to 17 atm. % and seems to decrease slightly with increasing oxygen concentration.

### 4.6.4. Summary

The electrical properties of contaminated i-layers indicate a shift of the Fermi level towards the conduction band for oxygen concentrations above $2\times10^{19}$ cm$^{-3}$ and for nitrogen concentrations above $4\times10^{18}$ cm$^{-3}$. The behavior of oxygen and nitrogen contaminated films is similar, except for a difference in absolute values, that implies

a similar incorporation mechanism. Only for oxygen at high concentrations alloying is observed for electrical as well as optical properties.

## 4.7. Impact of local oxygen distribution in solar cells on critical base pressure

In this section the impact of the local distribution of oxygen in the i-layer is studied. Oxygen that is incorporated in the amorphous i-layer only in the vicinity of the p/i-interface also leads to $C_{O,crit} = 2\times10^{19}$ cm$^{-3}$, as already found for solar cell whose i-layer is homogeneously contaminated. In contrast, for oxygen contamination only in the vicinity of the i/n-interface, a higher oxygen concentration than $C_{O,crit}$ is possible without losses in solar cell efficiency.

### 4.7.1. Realisation of different local oxygen distributions in the i-layer

The partial contamination of the a-Si:H solar cells is obtained via two subsequent i-layer depositions. First, after the deposition of the p-doped layer an uncontaminated part of the i-layer is deposited. Then, the second part of the i-layer is grown with an additional oxygen flow. The thickness of the i-layer was ~ 350 nm which is standard for a-Si:H solar cells. The ratio $X_P$ of thickness of the different i-layers is determined by the ratio of the deposition times for the different i-layers (see Figure 4.7). Due to the order of deposition, the intrinsic layer is only contaminated in the vicinity of the n-layer.

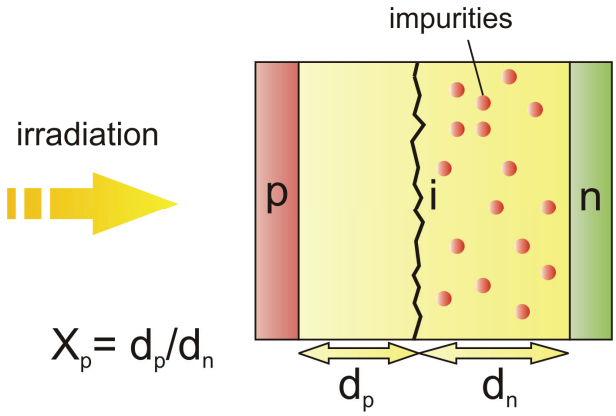


*Figure 4.7 Schematic drawing of a partialy contaminated p-i-n a-Si:H solar cell with the ratio $d_P$ indicating the uncontaminated part of the solar cell. The ratio $X_P$ of the solar cell absorber layer close to the p-layer is deposited without intentional contamination whereas the rest of the i-layer is intentionally contaminated.*

### 4.7.2. Partly contaminated solar cells

Figure 4.8 shows the quality of solar cell as a function of the uncontaminated part of the i-layer $X_P$ and of the oxygen flow (chamber wall leak) influenced base pressure of the contaminated part of the i-layer. As an indicator for the quality the solar cell's

fill factor is taken. For this type of solar cells a fill factor $FF > 73$ % is taken as an indication for a high performance cell whereas a lower fill factor indicates that the presence of donors or defects that deteriorate the solar cell's quality.

From Figure 4.8 it is obvious that only $X_P \sim 40$ % of the absorber layer in the vicinity of the p-layer need oxygen caused base pressures below ~ $7\times10^{-6}$ Torr in order to deposit state-of-the-art solar cells. Approximately at this base pressure the critical oxygen concentration $C_{O,crit} = 2\times10^{19}$ cm$^{-3}$ for homogeneously contaminated i-layers is reached. For the other part of the i-layer a higher base pressure can be tolerated. If $X_P \sim 60$ % of the i-layer in the vicinity of the p-layer has a $C_O < C_{O,crit}$ ($p_b < \sim 7\times10^{-6}$ Torr) the other part of the i-layer can be deposited with base pressures even above $10^{-4}$ Torr. In *section 4.4*, it is shown that a base pressure of $> 10^{-4}$ Torr results in $C_O > 5\times10^{20}$ cm$^{-3}$. For base pressures above ~ $5\times10^{-4}$ Torr for the contaminated part of the i-layer for all reasonable values of $X_P$ a weak solar cell performance is assumed due to the formation of an insulating $SiO_2$ layer.

In an additional experiment only the i-layer in the vicinity of the p/i-interface is contaminated with oxygen and it is found, that contamination in the vicinity of the p-layer directly leads to a critical level of ~ $7\times10^{-6}$ Torr.

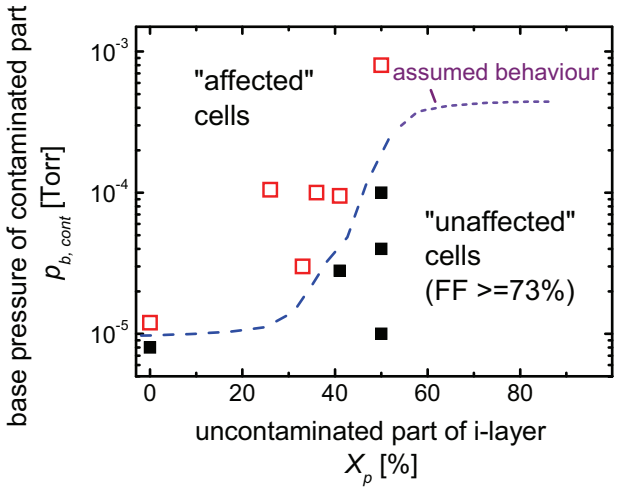


*Figure 4.8 Position of unaffected (open symbols) and affected (solid symbols) solar cells as a function of the base pressure during the growth of the contaminated part of the i-layer versus ratio of the uncontaminated part. The deposition regime is the HFHP I regime. Unaffected cells are those defined by a fill factor above 73 %. The separation line between unaffected and affected solar cells is a guide to the eye.*

In Figure 4.9 two exemplary current voltage curves of partly contaminated a-Si:H solar cells are shown. The base pressure induced by the oxygen leak is $10^{-4}$ Torr for the deposition of the contaminated fraction of the i-layer. The cell with $X_P = 50$ % has an initial efficiency $\eta_{ini} \sim 8.8$ %, $FF \sim 74$ %, $j_{SC} \sim 13.1$ mA/cm$^2$, and $V_{OC} \sim 909$ mV, respectively. This are state-of-the-art properties for solar cells grown in the HFHP I

regime. The other solar cell which is shown has a $X_P$ of about 36 %. Here, the cell characteristics are influenced by the oxygen incorporation; the initial efficiency $\eta_{ini}$ ~ 8.3 %, $FF$ ~ 71.9 %, $j_{SC}$ ~ 12.9 mA/cm², and $V_{OC}$ ~ 898 mV. This can be seen for the IV-measurement of the cell with $X_P$ = 36 % which is slightly shifted towards higher current densities in the vicinity of the maximum power point due to the reduced fill factor compared to the cell with $X_P$ = 50 %.

Similar findings are reported for µc-Si:H [Kil2009]. Here, as well as for a-Si:H, a value of 50 % for $X_P$ together with an oxygen flow above the critical flow (for a completely contaminated solar cell) still does not prevent the deposition of state-of-the-art µc-Si:H solar cells. A contamination at the p-side of the i-layer also leads to cell deterioration when exceeding the critical oxygen flow for a completely contaminated µc-Si:H solar cell.

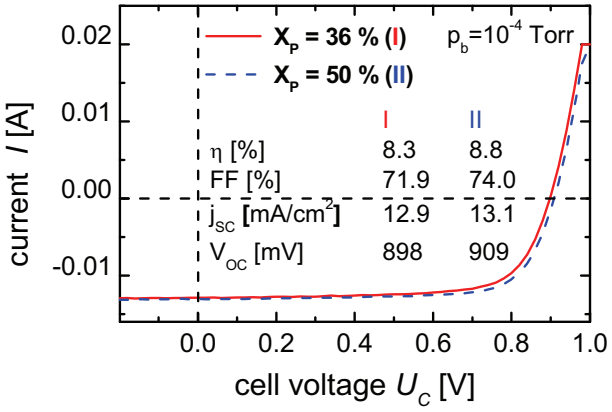


*Figure 4.9 Initial IV-characteristics of two solar cells grown in the HFHP I regime contaminated at an oxygen induced base pressure of $10^{-4}$ Torr. Cell I has an uncontaminated i-layer fraction $X_P$ ~ 36 %, whereas for cell II $X_P$ ~ 50 %. Slight losses in fill factor and, thus, efficiency are seen for cell I compared to cell II.*

## 4.8. Light-induced degradation of contaminated solar cells

In this section the light-induced degradation of oxygen and nitrogen contaminated cells is presented. It is found for oxygen and nitrogen that the critical contamination levels do not change upon light soaking. Quantum efficiency measurements revealed that contamination leads to a decrease in $QE$ in the red wavelength range and to an increase of the $QE$ in the blue wavelength range. Upon light-soaking this effect strengthened but never led to improved stabilized solar cell efficiencies

### 4.8.1. Solar cell parameters

Oxygen and nitrogen contaminated solar cells deposited at a high deposition rate (up to 0.5 nm/s) in the HFHP I regime are studied by means of a light-soaking

experiment. Figure 4.10 shows a comparison of the initial and after 1000 h of light-soaking measured solar cell parameters of contaminated solar cells.

The initial values (full symbols) have already been discussed in *section 4.5*. The open symbols show the solar cell parameters of the degraded solar cells. Generally, the degradation behavior is very similar for oxygen and nitrogen contaminated solar cells. Irrespective of the contamination species, the efficiencies (initial and after-light soaking) decrease with increasing impurity concentration when the critical nitrogen ($4\times10^{18}$ cm$^{-3}$) or oxygen ($2\times10^{19}$ cm$^{-3}$) contamination levels are exceeded. Note, the critical oxygen and nitrogen contamination levels both do not change upon light soaking. Uncontaminated solar cells show a decrease in efficiency of about 27 % from ~ 8.6 % to 6.4 % after light-soaking.

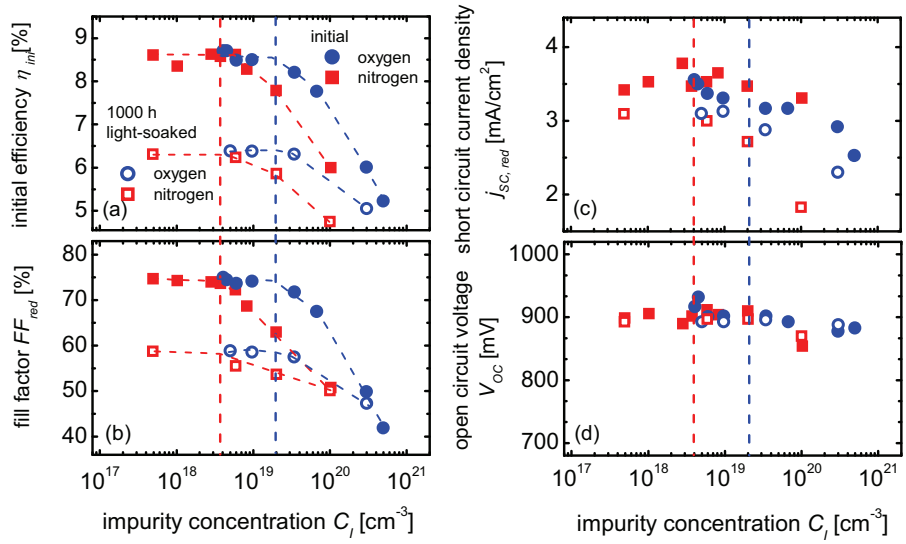


*Figure 4.10 Initial (full symbols, already shown in Figure 4.4) and light soaked (1000 h, open symbols) solar cell parameters under AM1.5 ($\eta_{ini}$ (a), $V_{OC}$ (d)) and red light ($FF_{red}$ (b), $j_{sc,red}$ (c)) illumination for oxygen and nitrogen contaminated intrinsic layers. The oxygen (vertical blue line) and nitrogen (vertical red line) initial critical concentrations are indicated.*

Significant losses in the fill factor, especially under red illumination, are mainly responsible for the decrease in efficiency upon light soaking. Furthermore, for the degraded state, the short-circuit current density under red illumination decreases significantly with increasing impurity concentration for cells contaminated above the critical impurity level. The open-circuit voltage does not change significantly under light exposure, even not for increasing impurity concentration. The large losses in efficiency for uncontaminated solar cells can be explained by the high deposition rate that was used (up to 0.5 nm/s) but the scope of this part of the study is only the effect of the impurities onto the light-induced degradation. The impact of the deposition

rate on impurity incorporation and solar cell stability will be discussed in detail in *chapter 5*.

### 4.8.2. Quantum efficiency

In order to quantify the light-induced degradation and contamination losses with respect to the wavelength dependent quantum efficiency (*QE*), measurements before and after 1000 h light-soaking were performed. Figure 4.11 shows quantum efficiency spectra of a-Si:H solar cells with different oxygen and nitrogen concentrations. In the initial state the QE-measurements are shown for 0 V and without any bias light because there is no difference seen for these two types of measurement. In contrast, due to the largely increased number of defects upon light-soaking these measurements were performed with additional white bias light in order to saturate the defects and extract the generated charge carriers (intensive light conditions).

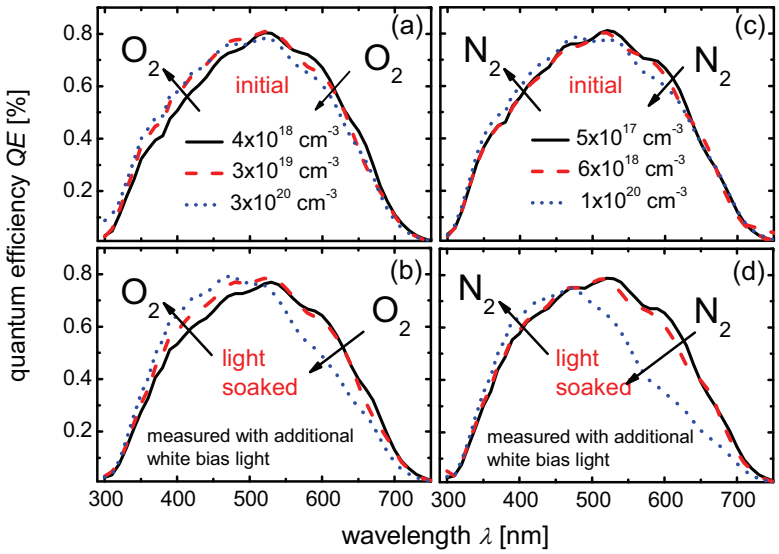


*Figure 4.11 Quantum efficiency (QE) spectra of a-Si:H solar cells with intrinsic layers that are contaminated with oxygen (a, b) and nitrogen (c, d). The QE measurements are performed at 0 V before (a, c) and with at 0 V and additional white bias light after 1000 h of light-soaking (b, d).*

In Figure 4.11 (a) the QE-spectra of three solar cells with different oxygen concentrations are shown – one slightly contaminated below the critical level, one approximately at the critical level and one far above. With increasing oxygen concentration the collection efficiency at long wavelength (around 600 nm) decreases indicating an enhanced recombination of charge carriers generated in the bulk material. In contrast, in the initial state an increase in quantum efficiency is observed for increasing oxygen concentration at short wavelength (400 nm). After light-soaking (see Figure 4.11 (b)) these general trends are even more pronounced, i.e., the

highest oxygenated solar cells exhibit larger collection efficiency losses in the long wavelength range and larger gains in the short wavelength range. This is in correspondence with $j_{SC,\,red}$ (after light-soaking) at high oxygen concentrations, i.e., $j_{SC,\,red}$ decreases from 3.3 mA/cm$^2$ to 2.2 mA/cm$^2$ (see Figure 4.10).

For nitrogen contaminated films the trends are similar to those for oxygen contaminated solar cells (see Figure 4.11 (c, d)) except that the shift sets in already at lower concentrations, i.e. at the critical impurity concentration of nitrogen.

## 4.9. Discussion

The results show that the properties of a-Si:H p-i-n solar cells deteriorate when a critical contamination level of $4\times10^{18}$ atoms/cm$^3$ for nitrogen or of $2\times10^{19}$ atoms/cm$^3$ for oxygen is exceeded in the i-layer. These levels are similar to those observed for μc-Si:H solar cells (see *chapter 6* and [Kil2009]).

### 4.9.1. Incorporation model for oxygen & nitrogen

Based on the results for electric and optical properties of single i-layers (Figure 4.6), a part of the oxygen and nitrogen is assumed to be incorporated into the absorber layer in an electronically active doping configuration. This is assumed due to the observed increase in conductivity when the critical contamination level is exceeded. For solar cells such kind of impurity incorporation leads to a deterioration of the solar cells that is caused mainly due to losses in the fill factor, especially, under red light illumination.

This model of impurity incorporation in doping configurations was proposed by Kinoshita et al. [Kin1996], who considered cells and films deposited from pure silane PECVD plasma. Generally, oxygen and nitrogen are incorporated in electronically inactive twofold-coordinated and threefold-coordinated states, respectively. However, a small fraction of the incorporated impurities is not incorporated in the above mentioned coordination. Threefold-coordinated oxygen ($O_{(3)}^{+}$) and fourfold-coordinated nitrogen ($N_{(4)}^{+}$) are considered to be doping configurations [Mor1991]. Besides, it might be possible as well that OH groups are incorporated in an electrically active state [Woe2010].

Considering the rather high values for the critical concentrations it can be concluded, that, for instance, only a very small fraction of incorporated oxygen is present in a doping configuration. By comparison with phosphorus doping [Bey1984], based on conductivity measurements, one can estimate that at the critical oxygen concentration of $2\times10^{19}$ atoms/cm$^3$ approximately only $10^{16}$ oxygen atoms/cm$^3$ (~ 0.5 ‰) are in doping configurations.

### 4.9.2. Impact of oxygen & nitrogen on solar cells

In the above introduced model of Kinoshita et al. the decrease in solar cell performance is mainly attributed to changes of the internal electric field in the absorber layer (driving force for charge carriers) of the solar cell [Kin1996]. This

model is very convenient to explain the decrease in solar cell performance. However, the physically correct interpretation of the impact of the doping is a reduction of the quasi Fermi level gradient (electrochemical potential) under illumination [Wue2009]. The smaller the gradient the less effective the charge carriers can be extracted from the solar cell. Both models are applicable and lead to the same results. The donors create a positive space charge in the vicinity of the p/i-interface and strengthen the electric field (increase the gradient) at this particular location, whereas the electric field (gradient of the electrochemical potential) over the bulk i-layer is weakened.

This principle is illustrated in Figure 4.12 (a) for an uncontaminated solar cell and (b) for a solar cell which i-layer is homogeneously contaminated. This field distribution would explain why the solar cell properties measured under blue illumination do not suffer as significantly as the cell properties measured under AM1.5 or red light illumination from the impurity incorporation. The generated charge carriers can be even better extracted when generated at the p/i-interface for a moderate contamination. This is confirmed by the increased quantum efficiency (*QE*) measured in the short wavelengths region for an increased impurity concentration (Figure 4.11).

As positive as this effect is for the photo-generated charge carriers at the p/i-interface, as negative it is for the charge carriers created at long wavelength light in the bulk absorber layer. Here, the reduced electric field (smaller gradient) leads to lower extraction efficiencies. This can be demonstrated by the strong sensitivity to impurity incorporation of, for instance, the solar cell fill factor measured under red light illumination (Figure 4.4).

Further aspects supporting the above mentioned model of impurity incorporation are the influence of the i-layer thickness [Kil2009] & [Rec1998] and the impact of the location of the impurities on the contamination sensitivity (see *section 4.7*). For a thin i-layer or an i-layer contaminated only in the vicinity of the n-layer, oxygen and nitrogen contaminations (n-type donors) do not decrease the cell properties in contrast to i-layers contaminated only in the vicinity of the p-layer or thick i-layers. If an n-type donor is incorporated in the vicinity of the n/i-interface, the result is a gradient in n-type donor concentration from the n-layer to the i-layer. The internal field will be influenced, but not significantly enough to deteriorate the solar cell performance (see Figure 4.12 (c)). In turn an n-type donor in the vicinity of the p/i-interface will lead to a p-n-i-n like structure and the internal field over the i-layer is reduced, as shown in Figure 4.12 (d). Note, there still may be a weak field due to the different doping efficiencies of impurities (first n-type like layer) and boron (n-layer).

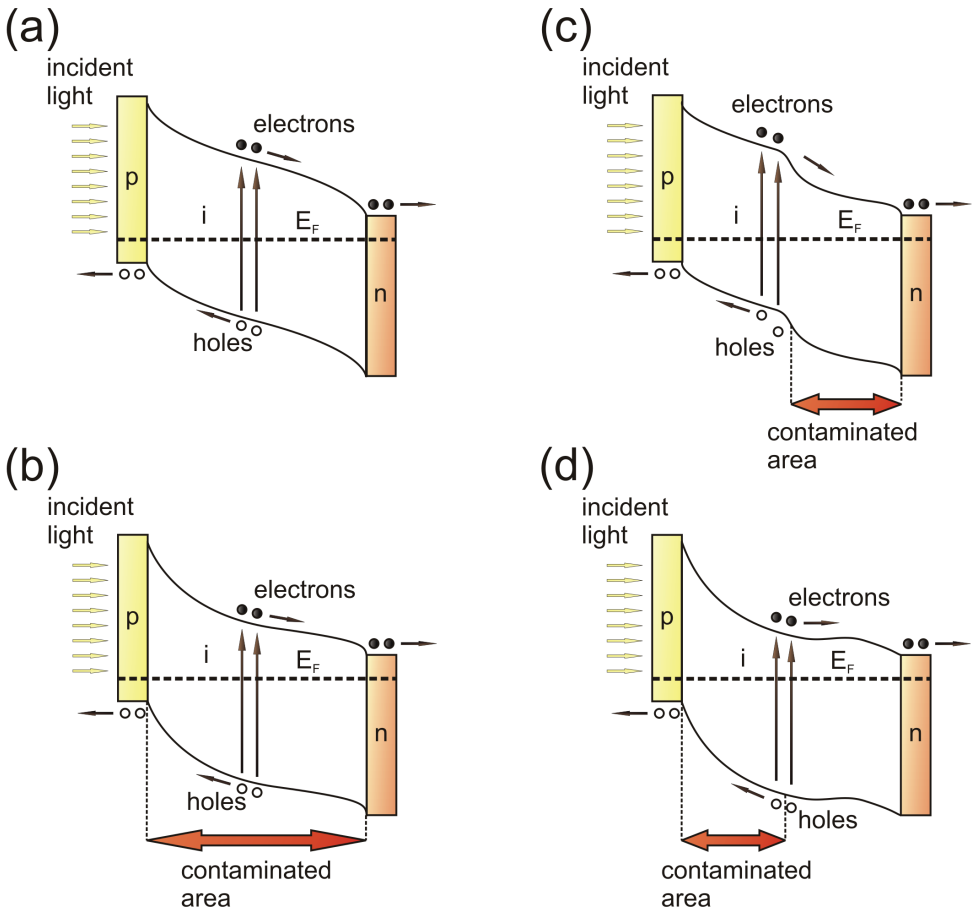


*Figure 4.12 Schematic drawing of the band diagram of (a) uncontaminated, (b) homogeneously contaminated, and partly (c, d) contaminated solar cell. The location of the contamination is indicated by the red arrows below the drawings.*

### 4.9.3. Impact of oxygen & nitrogen on single i-layers

The electrical properties of the i-layers correspond to the properties of the cells over the considered range of impurity concentration. The critical oxygen and nitrogen concentrations are also seen for single i-layers in terms of an increase in charge carrier density and, thus, in dark-conductivity. Also an increase in photoconductivity is seen, which is typical for doping of a-Si:H [Bey1983].

For very high concentrations of oxygen (>$10^{20}$ $cm^{-3}$) the alloying effect becomes significant which is seen in the electrical as well as in the optical data (PDS, see Figure 4.6 (d)). The impact of alloying may also be responsible for the cell deterioration of solar cells contaminated only in the vicinity of the i/n-interface. In this case, strong n-type doping is assumed not to deteriorate the solar cell performance. A decrease in cell efficiency is assumed for base pressures leading to oxygen concentrations above 5×$10^{20}$ $cm^{-3}$. For these concentrations an insulating layer

with a high fraction of $SiO_2$ is seen for single i-layers. In a solar cell such a layer would prevent a sufficient charge current flow, if the layer is thick enough. Corresponding effects are likely to occur for nitrogen concentrations exceeding $10^{20}$ atoms/cm$^3$. It is well known that the optical gap of Si-N alloys increases strongly when the nitrogen concentration exceeds a few atomic percents [Ban2000], [Mor1991], & [Shi1991].

Another explanation of the solar cell deterioration may be defect states in the i-layer of contaminated solar cells that can lead to a suppression of the bulk carrier collection. Also the Fermi-level shift towards the conduction band will lead to an increased concentration of charged defects as observed by the CPM measurements. This increase of charged defect density could in turn lead to a lifetime reduction of the generated carriers and to a deterioration of the solar cell performance.

### 4.9.4. Correlation of base pressure and impurity concentration

Introducing air, oxygen, or nitrogen into the deposition chamber leads to a remarkably similar critical base pressure (see Figure 4.5). Comparing the incorporation of nitrogen and oxygen impurities, the results show that oxygen is more efficiently incorporated than nitrogen (Figure 4.3). For example, at an impurity flow related base pressure of $10^{-5}$ Torr, a concentration of $3\times10^{18}$ atoms/cm$^3$ of nitrogen is found in the solar cell i-layer whereas the amount of oxygen in a corresponding cell is about 10 times higher, i.e. $3\times10^{19}$ atoms/cm$^3$. Thus, the oxygen incorporation probability is about ten times higher than the nitrogen incorporation probability. A reason for this difference may be the higher energy that is necessary to break up molecular nitrogen compared to molecular oxygen, in order to incorporate them (as atoms) into the structure [Mat2002]. There may also be a higher sticking coefficient of oxygen compared to that of nitrogen on the growing a-Si:H surface.

Furthermore, from the critical impurity levels with respect to the solar cell performance it is assumed that the nitrogen doping efficiency is approximately 10 times larger compared to that for oxygen. Thus, the effects of doping efficiency and incorporation probability compensate for oxygen and nitrogen incorporation, leading to a similar critical oxygen and nitrogen base pressure. Since air is mainly composed of oxygen and nitrogen the critical air base pressure is similar to the oxygen and nitrogen critical base pressure.

However, from the solar cell performance as a function of the oxygen and nitrogen concentration for air-leak contaminated cells it is seen, that oxygen is the main cell destructive contaminant, i.e. the critical oxygen concentration is reached first for air-leak contamination. This is surprising since the ratio of oxygen to nitrogen in air is ~1/4. Thus, from the oxygen and nitrogen contamination experiments a ratio of 10/4 of incorporated oxygen to incorporated nitrogen would have been expected since the oxygen incorporation probability is 10 times higher compared to that for nitrogen. Now, assuming a 10 times higher doping efficiency for nitrogen compared to that for oxygen, one would guess nitrogen to be the main

cell destructive contaminant. An explanation can be the preferred incorporation of oxygen in the presence of both species.

As a consequence, it is seen that for air leakages or poor vacuum systems, the oxygen incorporation for the HFHP I deposition regime is a slightly more crucial factor determining the solar cell quality.

### 4.9.5. Light-induced degradation

The impact of light-soaking (1000 h) upon contaminated cells is similar to the behavior of the cells in the intrinsic state. The critical impurity levels for oxygen and nitrogen do not change upon light soaking. This is a remarkable finding since the SWE is thought to create defects via light absorption that, in turn, would pin the Fermi level at mid-gap if the number of light-induced defects is larger compared to that of the defects created by the impurity incorporation. This should lead to a higher critical impurity concentration, but experimentally it is seen that, even if the defects, induced by the SWE, should pin the Fermi level to mid-gap position the impurities are assumed to still influence the internal electric field (gradient of the quasi Fermi levels under illumination) of the p-i-n solar cell.

Another possibility would be that the number of light-induced defects is smaller than the number of impurity caused defects and, thus, could not pin the Fermi level (experimentally not observed in [Kin1996]). This would further imply that the impurity caused defects do not significantly influence the solar cell performance whereas the light induced defects deteriorate the solar cell performance.

A third option is the presence of a "donor reservoir". A part of the donors is not activated building this reservoir and if the Fermi level is shifted to lower energies by the light-induced defects from the reservoir new active donors are released. However, this model also is in contradiction with the pinning of the Fermi level observed for single films after light-soaking by [Kin1996]. Here, no unambiguous interpretation is found yet.

## 4.10. Summary

Oxygen and nitrogen (via CWL) concentrations higher than $2\times10^{19}$ $cm^{-3}$ and $4\times10^{18}$ $cm^{-3}$ lead to a reduction of the initial solar cell efficiency of cells deposited in the HFHP I regime. After light induced degradation these levels remain unchanged and the cell performance is strongly dominated by the impurities. These findings for a-Si:H (and μc-Si:H) solar cells can be explained by a n-type doping character of a part of the incorporated oxygen.

# 5. Influence of the total process gas flow & deposition rate on impurity incorporation

In the foregoing chapter the general impact of oxygen and nitrogen on a-Si:H solar cells was intensively studied. This chapter deals with the fabrication of device quality a-Si:H solar cells at relatively high base pressure conditions (oxygen flows) with low atmospheric contamination and their light-soaking stability. The effect of the total process gas flow (from ~ 110 sccm to ~ 1015 sccm) and deposition rate (from ~ 0.15 nm/s to ~ 0.5 nm/s) on the oxygen incorporation is systematically studied. Here, three deposition regimes were applied. For total flow rates of ~ 112 sccm (LFLP regime) and ~ 368 sccm (HFHP I regime) the critical oxygen concentration is the same as already seen in *chapter 4*, namely ~ $2\times10^{19}$ $cm^{-3}$. This critical level is seen for solar cells as well as for single i-layer electrical characteristics. For a total source gas flow of ~ 1015 sccm (HFHP II regime) the critical oxygen concentration increased to $C_{O,crit}$ ~ $2\times10^{20}$ $cm^{-3}$, which is only observed for solar cells and not for the material (electrical) characteristics. These critical levels are independent upon light-soaking, as already seen in *chapter 4* for the HFHP I regime. The critical oxygen concentration is speculated to depend on the oxygen precursor lifetime, namely $SiO_2$, siloxane, and OH / $H_2O$ molecules. For a deposition regime with a slow oxygen incorporation (HFHP II regime) more of the stable siloxanes are incorporated with respect to the less stable hydrogen-oxygen molecules that are assumed to lead to oxygen in a doping configuration.

Furthermore it is observed that the oxygen incorporation probability is highest for the LFLP regime and lowest for the HFHP II regime, i.e., proportional to the source gas flow. Thus, it is not surprising that the critical base pressures for the three regimes increase with increasing source gas flow. Note, for the highest flow also the critical level increases. This is assumed to be due to, e.g., oxygen dilution in the source gas. Also, an increase in deposition rate (i.e. discharge power) slightly decreases the incorporation probability due to a dilution of the oxygen with respect

to film precursors created by silane dissociation that is enhanced by an increased discharge power.

## 5.1. Introduction

Commonly, values between $2\times10^{19}$ $cm^{-3}$ and $5\times10^{19}$ $cm^{-3}$ are found for the critical oxygen concentration and of $4\times10^{18}$ $cm^{-3}$ for the critical nitrogen concentration in a-Si:H solar cells [Shi1991] & [Iso1996]. In this chapter the focus is on oxygen incorporation from a chamber wall leak and address the questions:

(i) Is the oxygen incorporation dependent on the deposition rate for different deposition regimes? In [Kro1995] it was shown that for a 70 MHz PECVD process the oxygen incorporation is proportional to $1/r_d$ (see *section 4.1*). In their study they used undiluted silane as process gas. In this chapter it is investigated if a similar dependency is also found for a lower applied frequency and for a hydrogen diluted process gas.
(ii) Is the critical oxygen concentration dependent on the deposition conditions?
(iii) Does the critical oxygen concentration change upon light-soaking? For the HFHP I regime the critical level did not change upon light-soaking. Since for this behavior no unambiguous explanation is found it is investigated if the critical concentration changes for the light-soaked state for other deposition regimes that the HFHP I regime.

Therefore, three different deposition regimes (different total process gas flows) and different deposition rates for each regime are studied for their oxygen incorporation. Also, contaminated solar cells and single i-layers are grown in the three deposition regimes. The influence of the deposition parameters on the critical oxygen concentration is investigated. Finally, the impact of 1000 h of light-soaking on the critical oxygen concentration is studied.

## 5.2. Process conditions of the i-layer

For this study three deposition regimes are used and described in the following (see also Table 5.1). The low-flow low-pressure (LFLP) regime is characterized by a low deposition pressure of 3 Torr, a $SiH_4|H_2$ process gas flow of 12|100 sccm, and a heater temperature of 260 °C. The applied discharge powers were 0.01 - 0.03 $W/cm^2$, yielding deposition rates of 0.15 - 0.5 nm/s, respectively. The high-flow high-pressure (HFHP) regimes both had a deposition pressure of 10 Torr and a heater temperature of 200 °C. Their process gas flows were 7.8|360 sccm and 15|1000 sccm for HFHP I & II, respectively. The applied discharge power was approximately 0.13 - 0.2 $W/cm^2$ and the deposition rate was ~ 0.27 – 0.5 nm/s. The intentional oxygen leak was situated at the chamber wall (CWL).

| | $\Phi_{H2}$ [sccm] | $\Phi_{SiH4}$ [sccm] | $p$ [Torr] | $T_H$ [°C] | $P$ [W/cm²] | $r_d$ [nm/s] |
|---|---|---|---|---|---|---|
| LFLP | 100 | 12 | 3 | 260 | 0.01/0.03 | 0.15/0.50 |
| HFHP I | 360 | 7.8 | 10 | 200 | 0.13/0.20 | 0.27/0.50 |
| HFHP II | 1000 | 15 | 10 | 200 | 0.13/0.20 | 0.27/0.44 |

*Table 5.1 Process parameters for the LFLP, HFHP I, and HFHP II regimes, respectively.*

## 5.3. Correlation of base pressure and impurity concentration

It is found that the incorporation probability of oxygen can be reduced via an increase in discharge power or source gas flow. Note, if not mentioned otherwise the impurity incorporation probability is defined as the amount of impurities introduced into the reactor compared to the impurity concentration found in the i-layer. Both ways lead somehow to a dilution of the oxygen that can be incorporated. Thus, not surprisingly, in contrast to the findings in *chapter 4* the critical base pressures, observed for solar cells (see *section 5.4*), differ for each deposition regime.

In order to study the incorporation probability of oxygen as a function of the total process gas flow and deposition rate the oxygen concentration in the i-layer as a function of the base pressure is shown in Figure 5.1. The investigated deposition regimes are the LFLP regime with deposition rates $r_d$ = **0.15** / 0.50 nm/s, the HFHP I regime with $r_d$ = 0.27 / **0.50** nm/s, and the HFHP II regime with $r_d$ = 0.27 / **0.44** nm/s. The most frequently used deposition rates for the three regimes, also in the other chapters, are written with bolt numbers. The deposition rates are adjusted by means of the discharge power.

It is already demonstrated in Figure 4.3 that the base pressure increases for increasing oxygen flow into the deposition chamber, leading to a higher oxygen concentration in the i-layer. This general trend is independent on the total process gas flow and deposition rate. The critical oxygen concentrations for solar cells (see *section 5.4*) are indicated at $2\times10^{19}$ atoms/cm$^{-3}$ and $2\times10^{20}$ atoms/cm$^{-3}$ for the LFLP and HFHP I regimes and for the HFHP II regime, respectively.

### 5.3.1. Impact of source gas flow

For the lowest deposition rate for each deposition regime at base pressures between $10^{-8}$ Torr and $10^{-6}$ Torr the difference in oxygen incorporation probability between the HFHP I & II regimes is negligible while for the LFLP regime an increased oxygen incorporation probability of approximately half an order of magnitude is observed. At base pressure conditions of $10^{-5}$ Torr, the oxygen concentration in the cell is more than one order of magnitude lower for the HFHP I regime compared to the LFLP regime. For the HFHP II regime the oxygen concentration is even by nearly one order of magnitude lower in contrast to the HFHP I regime. The amount of incorporated oxygen for a given base pressure thus is

strongly reduced with increasing total process gas flow that is assumed to dilute the oxygen or to reduce the oxygen in-diffusion into the plasma zone.

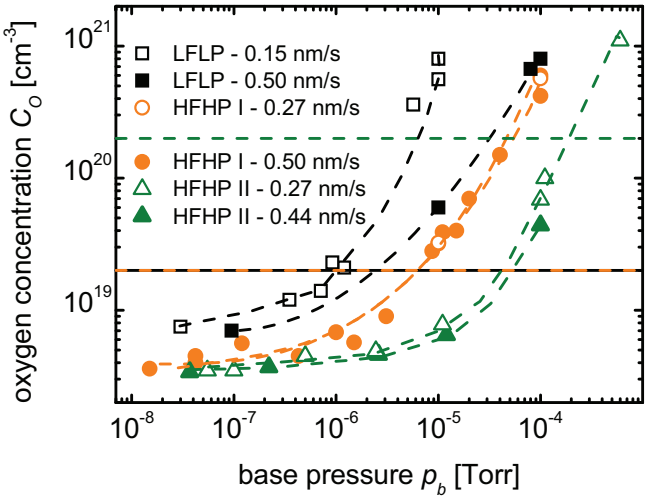


*Figure 5.1 Oxygen concentration in the i-layer as a function of the base pressure for oxygen contaminated a-Si:H multilayer films and solar cells deposited in the LFLP (~ 100 sccm), HFHP I (~ 400 sccm), and HFHP II (~ 1000 sccm) regimes. The critical oxygen contamination levels determined from are indicated by the horizontal dashed lines. For all regimes two different deposition rates are shown (for values see figure legend).*

### 5.3.2. Impact of deposition rate

For the LFLP regime an increase in deposition rate leads to a reduced oxygen incorporation probability, as expected [Kro1995]. They explained this reduction with a dilution of the oxygen compared to silane radicals that are created via dissociation of silane. A higher deposition rate achieved by a higher discharge power would lead to an increase in silane radicals. This dilution increases for the LFLP regime the critical base pressure where solar cell deterioration sets in from $p_{b,crit} \sim 10^{-6}$ Torr to $p_{b,crit} \sim 3\times10^{-6}$ Torr.

For the HFHP regimes a higher deposition rate does not lead to a significantly reduced oxygen incorporation probability. The critical base pressures in this case are $p_{b,crit} \sim 7\times10^{-6}$ Torr and $p_{b,crit} \sim 2\times10^{-4}$ Torr for the HFHP I & II regimes, respectively. Note, the increased critical oxygen concentration for the HFHP II regime also contributes to this enhanced maximum tolerable base pressure of $p_{b,crit} \sim 2\times10^{-4}$ Torr.

| | $r_d$ [nm/s] | $P_{b,crit}$ [Torr] | $C_{O,crit}$ [cm$^{-3}$] |
|---|---|---|---|
| LFLP | 0.15/0.50 | $1\times10^{-6}/3\times10^{-6}$ | $2\times10^{19}$ |
| HFHP I | 0.27/0.50 | $7\times10^{-6}/7\times10^{-6}$ | $2\times10^{19}$ |
| HFHP II | 0.27/0.44 | $2\times10^{-4}/2\times10^{-4}$ | $2\times10^{20}$ |

*Table 5.2 Deposition rates, critical oxygen concentrations, and critical base pressures for the LFLP, HFHP I, and HFHP II regimes, respectively.*

## 5.4. Solar cells based on contaminated i-layers

Solar cells were prepared with different intentionally contaminated i-layers for the LFLP, HFHP I & II regimes. Hereby the deposition conditions are systematically varied, and the deposition rates were 0.15 nm/s – 0.5 nm/s – 0.44 nm/s for LFLP – HFHP I - HFHP II, respectively. In Figure 5.2, the initial solar cell parameters (efficiency $\eta_{ini}$ (a), fill factor *FF* (b), short-circuit current density $j_{SC}$ (c) and the open-circuit voltage $V_{OC}$ (d)) are shown as a function of the oxygen concentration in the i-layer.

For all regimes, initial efficiency and fill factor decrease by increasing the impurity concentration in the i-layer when a critical oxygen contamination level is exceeded. Below this level, the solar cell parameters are not significantly affected. For the LFPL and HFHP I regimes this critical contamination level is found to be ~ $2\times10^{19}$ oxygen atoms/cm$^3$, independent on the regime.

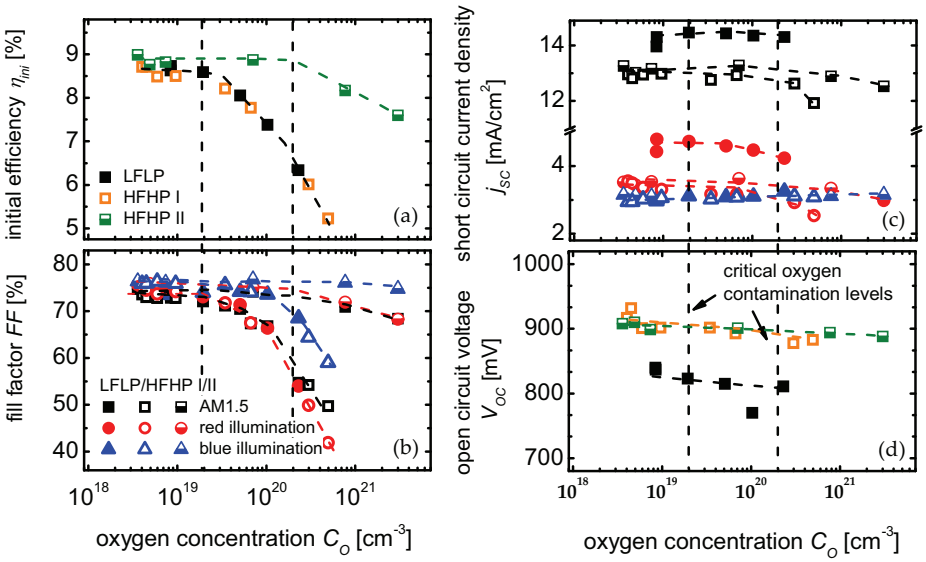


*Figure 5.2 Solar cell parameters of p-i-n a-Si:H solar cells deposited in the LFLP, HFHP I & II regimes as a function of the oxygen concentration in the i-layer. The dashed lines are guides to the eye. For LFLP and HFHP I the critical oxygen contamination level is ~ $2\times10^{19}$ atoms/cm$^3$ and for HFHP II it is ~ $2\times10^{20}$ atoms/cm$^3$.*

However, for the HFHP II regime this level is found to be approximately one order of magnitude higher at ~ $2\times10^{20}$ oxygen atoms/cm$^3$. The $V_{OC}$ for the LFLP regime is about 840 mV and for the HFHP regimes at approximately 900 – 910 mV; $j_{SC}$ is around 14 mA/cm$^2$ for the LFLP regime and around 13 mA/cm$^2$ for the HFHP regimes. These differences in $j_{SC}$ and $V_{OC}$ for the deposition regimes can be directly linked to the material properties as it is shown in the next section. Under red light illumination for the LFLP and HFHP regimes $j_{SC,\,red}$ decreases slightly for increasing oxygen concentration when exceeding the critical contamination level.

## 5.5. Material properties

For the LFLP and HFHP I regimes in the material properties the critical oxygen concentration obtained from solar cells can be seen. In contrast, this is not possible for the HFHP II regime. Figure 5.3 reveals the material properties of i-layers as a function of the oxygen concentration deposited by the three different deposition regimes. Hereby, again, the deposition conditions are systematically varied, and the deposition rates were 0.15 nm/s – 0.5 nm/s – 0.44 nm/s for LFLP – HFHP I - HFHP II, respectively.

### 5.5.1. Electrical properties

The general trends for conductivity, photosensitivity and activation energy with increasing oxygen concentration for LFLP and HFHP I are the same and are already discussed for the HFHP I regime *in chapter 4*. Both regimes indicate at the critical oxygen concentration at around $2\times10^{19}$ cm$^{-3}$ a decrease in conductivity if this concentration is exceeded. The opposite behavior for high oxygen contaminations larger than ~ $10^{20}$ cm$^{-3}$ in the i-layers is attributed to an increased band-gap of the material (Figure 5.3 (d)). The difference between the two regimes is a shift of the absolute values. Quantitatively, it is seen that for the photo- and dark conductivity the values obtained for the LFLP deposited films are by approximately half an order of magnitude higher compared to the HFHP I films (see Figure 5.3 (c)), while activation energy and photosensitivity are lower (see Figure 5.3 (a-b)). For example the activation energy of the LFLP deposited i-layers is approximately 50 meV lower compared to HFHP I grown films.

For the HFHP II regime there are no significant changes in electrical properties of single contaminated i-layers for increasing oxygen concentration.

### 5.5.2. Optical properties

The optical gap increases with increasing oxygen concentration for all regimes, see Figure 5.3 (d). This increase becomes stronger for concentrations above $10^{20}$ cm$^{-3}$, i.e., the onset of measurable alloying. The determined band gaps are 1.93 eV and 1.96 eV for uncontaminated films, grown in the LFLP and HFHP I & II regimes, respectively. The higher band gap for the HFHP regimes is assumed to lead to higher

$V_{OC}$ and lower $j_{SC}$ values for the HFHP regimes compared to those for the LFLP regime.

The absolute density of defects $N_D$ (via CPM) is lowest for the LFLP regime and highest for the HFHP I regime. This effect could be due to the correspondingly increasing deposition rates. A higher deposition rate is thought to cause more defects during the absorber layer growth. $N_D$ also does not change significantly upon oxygen concentration for the HFHP II regime whereas for the two other regimes an increase in $N_D$ with increasing oxygen concentration is seen.

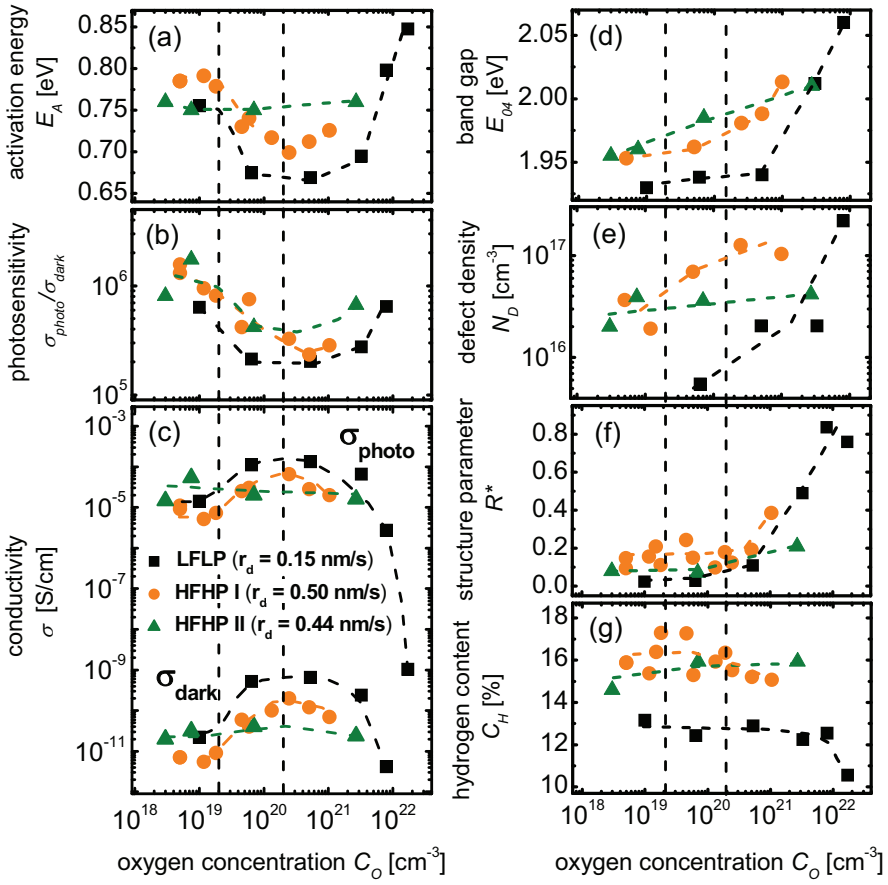


*Figure 5.3 Activation energy $E_A$ (a), photosensitivity (b), photo- and dark conductivity $\sigma_{photo}$, and $\sigma_{dark}$ (c), mobility band gap $E_{04}$ (d), defect density $N_D$ (e), microstructure factor R* (f) and hydrogen content $C_H$ (g) as functions of the oxygen concentration in the intrinsic a-Si:H films deposited by different deposition regimes. The first vertical dashed line represents the critical contamination level at $2\times10^{19}$ atoms/cm$^3$ observed for the LFLP and HFHP I regimes whereas the second is the limit in oxygen concentration of $2\times10^{20}$ atoms/cm$^3$ for the HFHP II regime.*

### 5.5.3. Structural properties

Structural differences for the three regimes were also observed by FTIR measurements. It is found that for the LFLP regime the (bound) hydrogen concentration is ~ 13 % and for the HFHP I & II regimes it is 16 - 17 % and 15 - 16 %, respectively, nearly independent on the oxygen concentration (Figure 5.3 (g)).

Differences were also obtained for the microstructure parameter $R^*$, see Figure 5.3 (f). For the LFLP regime the material tends to be more compact ($R^* \approx 0.03$) compared to the HFHP I & II regimes, where $R^* \approx 0.13$ and $R^* \approx 0.1$, respectively, are observed. This somewhat more porous film structure and the increased hydrogen concentration may be caused by the 3 - 4 times higher deposition rate, or by the lower temperature used in the HFHP regimes compared to the LFLP regime.

## 5.6. Light-induced degradation of solar cells

In the previous section it was demonstrated that a high deposition rate and a high total gas flow lead to less oxygen incorporation in the i-layer of a-Si:H solar cells. Here, the impact of these deposition conditions on the light-soaking stability of solar cells is investigated.

### 5.6.1. Impact of deposition rate on light-induced degradation

First, the impact of the deposition rate (see *section 5.3*) on the light-soaking stability of nominally uncontaminated solar cells (i.e., lowest possible oxygen concentration) deposited by the LFLP and HFHP I & II regimes is studied (see Figure 5.4).

Initially, for all regimes the cell efficiencies are between 8.5 and 9 %. The initial efficiencies of cells deposited with the HFHP regimes are slightly higher compared to those for the LFLP regime. A low deposition rate leads to stabilized solar cell efficiencies of ~ 7 % for the LFLP and HFHP I regimes and to a stabilized efficiency of ~ 7.4 % for the HFHP II regime. For the higher deposition rate investigated a decrease of ~ 0.5 % abs. in stabilized efficiency for all deposition regimes is observed.

The decrease in cell efficiency for increasing light-soaking time is related to losses in *FF* under red-light illumination and slight losses in $j_{SC}$ under red light illumination (the strongest decrease of 0.4 mA/cm² is observed for the HFHP I regime), while $V_{OC}$ values remain constant.

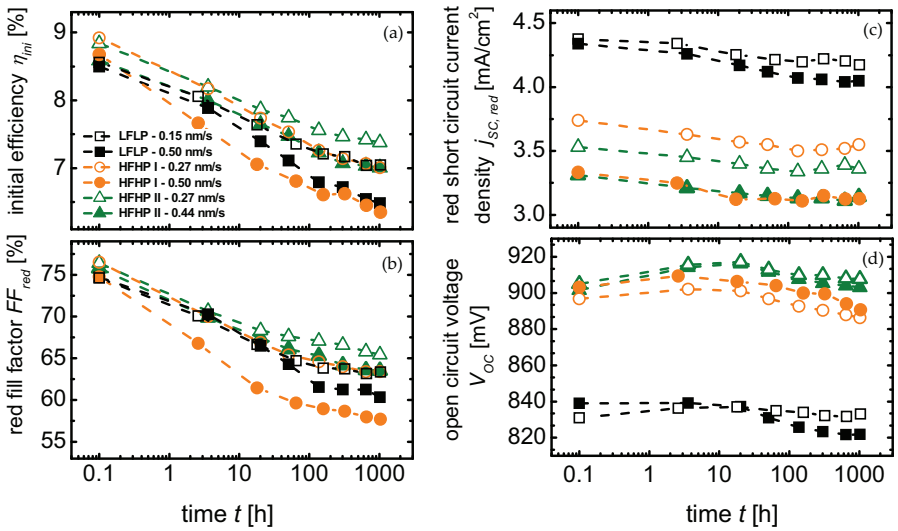


*Figure 5.4 Solar cell parameters of p-i-n a-Si:H solar cells deposited in the LFLP, HFHP I & II regimes at various deposition rates as a function of the light-soaking time. No intentional contamination was applied.*

**Diode quality factor** The solar cell characteristics in the dark (Figure 5.5) are in a good agreement with the solar cell parameters shown in Figure 5.4. The stabilized diode quality factors $n$ are low ($n \sim 1.75$) for cells which have a stabilized efficiency $\eta_{stab} \geq 7$ % and $n \sim 2$ for cells with stabilized efficiencies below 7 %. Initially, the diode quality factor is ~ 1.3, ~ 1.4, and ~ 1.5 for the HFHP II, LFLP, and HFHP I regimes, respectively.

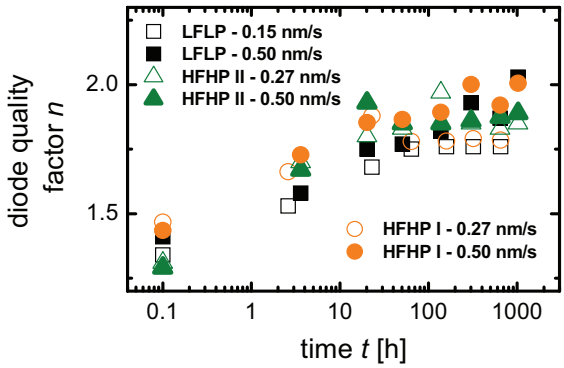


*Figure 5.5 Diode quality factor n as a function of the light exposure time for above mentioned process regimes and deposition rates.*

### 5.6.2. Impact of oxygen concentration on light-induced degradation

A detailed analysis of the influence of oxygen concentration and applied deposition regime on the solar cell parameters of solar cells in the light-soaked (LS) state is presented in Figure 5.6. Here, solar cells fabricated at a low deposition rate of 0.15 and 0.27 nm/s for LFLP and HFHP I & II, respectively are shown. For this figure a different way of visualization is used to compare the light-soaked (LS) properties of different solar cells easily. Note, the light-soaking kinetics are not shown but they are very similar for all deposition regimes and for the HFHP I regime the kinetics are already described in *chapter 4*.

As the $V_{OC}$ values were neither affected significantly by the incorporated oxygen nor by 1000 h of light soaking, variations of the product of $V_{OC}$ and *FF* as a function of the oxygen concentration in the light-soaked state represents differences in FF for the various cells. Nevertheless, attention has to be paid to the absolute $V_{OC}$ values since they differ for the 3 regimes, namely ~ 840 meV and 900 - 910 meV for LFLP and HFHP I & II, respectively. On the x-axis the short-circuit current density $j_{SC}$ (LS) is given. Here, also differences related to deposition regimes become visible. For a given oxygen concentration the $j_{SC}$ for the LFLP regime is always ~ 1 - 2 mA/cm² higher compared to that for the HFHP regimes. The full and dashed lines in the diagram are equi-efficiency lines. The degree of filling of the symbols is proportional the oxygen concentration in the i-layer of the solar cells ($4\times10^{18} \rightarrow 8\times10^{18} \rightarrow 2\times10^{19} \rightarrow 5\times10^{19} \rightarrow 3\times10^{20} \rightarrow 6\times10^{20}$ atoms/cm³).

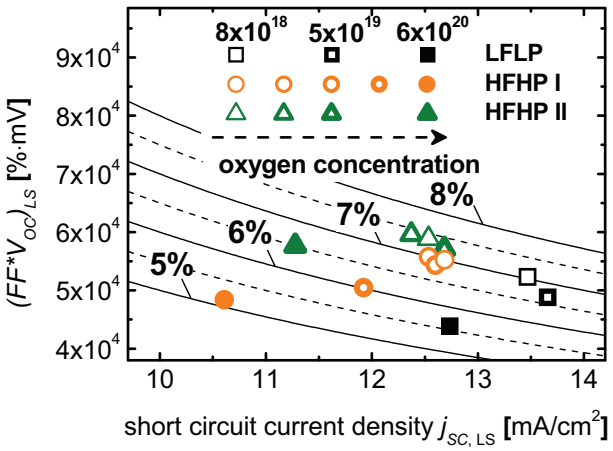


*Figure 5.6 Product of fill factor FF and open circuit voltage $V_{OC}$ as a function of the short circuit current density $j_{SC}$ (after 1000 h of light-soaking) for the same deposition regimes presented in Figure 5.2 (low deposition rates). The lines indicate the solar cell efficiencies. The increasing oxygen concentration is indicated by the increasing line thickness of the symbols [($4\times10^{18} \rightarrow 8\times10^{18} \rightarrow 2\times10^{19} \rightarrow 5\times10^{19} \rightarrow 3\times10^{20} \rightarrow 6\times10^{20}$) atoms/cm³].*

Up to the critical oxygen contamination level of approximately $2\times10^{19}$ atoms/cm$^3$ for the LFLP and HFHP I regimes and ~ $2\times10^{20}$ atoms/cm$^3$ for the HFHP II regime the stable efficiency does not change significantly and remains at 7 and 7.4 %, respectively. Exceeding the critical contamination levels, the stabilized efficiencies drop caused by losses in *FF* and in $j_{SC}$. Thus, for all studied deposition regimes no change in critical concentration upon light-soaking is observed.

The most prominent losses in efficiency, independent of the choice of oxygen concentration, were observed for HFHP I. Here, the $j_{SC}$ is lower for the cell with approximately $6\times10^{20}$ oxygen atoms/cm$^3$ by ~ 2 mA/cm$^2$, whereas for the other regimes this effect was only ~ 1 mA/cm$^2$.

## 5.7. Discussion

The general effect of oxygen incorporation in a-Si:H solar cells is discussed in *section 4.9*. In the following, the scope is on the effects of different deposition conditions on the oxygen impurity. A high deposition rate via high discharge power leads to an oxygen dilution with respect to silane radicals. A high source gas flow rate directly leads to a dilution of the oxygen in the gas phase or to a reduced in-diffusion of the oxygen into the plasma zone. However, for both cases the oxygen incorporation probability is reduced.

The critical oxygen concentration is speculated to depend on the oxygen precursor lifetime, namely $SiO_2$, siloxane, and OH or $H_2O$ molecules. For a deposition regime with slow oxygen incorporation more of the stable siloxanes are incorporated with respect to the hydrogen-oxygen molecules that are assumed to lead to oxygen in a doping configuration. The critical oxygen concentrations do not change upon light-soaking, irrespective of the applied deposition regime.

### 5.7.1. Impact of source gas flow on oxygen incorporation

It is found that the oxygen impurity incorporation probability can be significantly decreased by increasing the total process gas flow, see Table 5.2. By changing from the LFLP regime (total process gas flow of ~ 112 sccm) to the HFHP I (~ 368 sccm) deposition regime, keeping the deposition rate constant at $r_d$ = 0.5 nm/s, a by a factor of 2 - 3 increased impurity flow rate (base pressure) leads to nearly identical oxygen concentrations in the i-layer. Thus, a significant suppression of the oxygen incorporation can be achieved by increasing the total process gas flow from ~ 112 sccm to ~ 368 sccm (see Figure 5.1).

For this less efficient incorporation of impurities in the HFHP I regime compared to that for the LFLP regime, several reasons are conceivable. In particular, a higher flow rate of the process gases ($SiH_4$ and $H_2$) can lead to decreased impurity incorporation for a given base pressure due to a dilution of the impurities in the gas phase. On the other hand the higher process gas flow may prevent the in-diffusion of oxygen into the plasma zone. Thus, the oxygen concentration in the gas phase changes with increasing process gas flow. The oxygen incorporation probability can

be further reduced by means of a total gas flow enhancement by a factor of 2.5. Due to the high source gas flow, a ~ 7 times higher oxygen flow into the deposition chamber during the i-layer growth can be tolerated for the HFHP II ($r_d$ = 0.44 nm/s) regime compared to the HFHP I regime in order to allow an oxygen concentration of $C_O = 2\times10^{19}$ cm$^{-3}$. This can be well explained, again, by a higher dilution of the oxygen gas flow or by a lower in-diffusion rate of oxygen into the plasma zone.

A further outstanding result is the shift of the critical contamination level from ~ $2\times10^{19}$ atoms/cm$^3$ (LFLP and HFHP I) to ~ $2\times10^{20}$ atoms/cm$^3$ (HFHP II). The lower oxygen incorporation probability combined with the higher critical oxygen concentration lead to a toleration of a 20 - 30 times higher base pressure for the HFHP II regime compared to that for the HFHP I without solar cell quality deterioration.

**Critical oxygen concentration for solar cells** It is observed that the critical oxygen contamination level of ~ $2\times10^{20}$ cm$^{-3}$ for the HFHP II regime is one order of magnitude higher compared to that for the LFLP and HFHP I regimes. For an explanation of the higher critical oxygen concentration for the HFHP II regime a simple model is applied in order to estimate the incorporated oxygen fraction with respect to the introduced oxygen [Woe2010]. It turned out that for the LFLP, HFHP I, and HFHP II regimes the incorporated oxygen fractions are 1:$10^5$, 1:$2\times10^5$, and 1:$2.5\times10^6$, respectively. It is assumed that in the vicinity of the leak, amongst others, $SiO_2$, siloxanes, and OH or $H_2O$ is build for every deposition regime. $SiO_2$ will drop as dust or might be incorporated as $SiO_2$ clusters. Siloxanes are suggested to lead to oxygen that is incorporated electronically inactive and oxygen from the hydrogen-oxygen complexes can be incorporated (in part) electronically active. For the doping efficiency the molecule lifetimes are decisive.

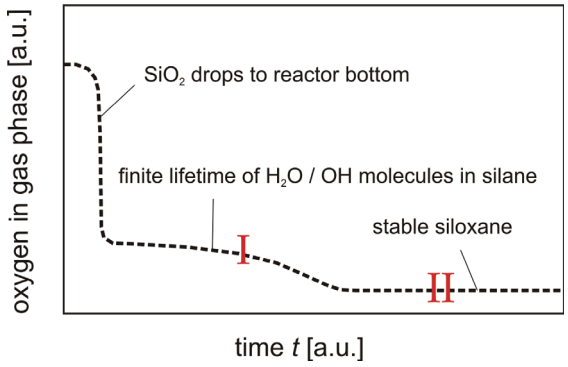


*Figure 5.7 Schematic drawing of the assumed quantity and appearance of oxygen in the gas phase as a function of time.*

If the incorporation is a slow process, the molecule might have already undergone a further reaction before being incorporated. The siloxane is assumed to be stable and, thus, reaches the substrate for every deposition regime whereas the hydrogen-oxygen complexes are less stable than the siloxane molecule. This

assumption induces that, dependent on the time consumption of the oxygen incorporation, the doping efficiency and the incorporation probability of the oxygen changes.

This is illustrated in Figure 5.7. If oxygen is incorporated very fast, there still are OH or $H_2O$ molecules from which oxygen can be incorporated in a doping configuration. This situation is indicated in Figure 5.7 as condition I. If the oxygen incorporation takes more time, e.g., due to a slower in-diffusion of the oxygen into the plasma zone, only oxygen from the stable siloxanes is incorporated into the film. This situation is indicated in Figure 5.7, named condition II. It is assumed that the LFLP and HFHP I regimes lead to condition I and the HFHP II regime leads to condition II. These assumptions are supported by the oxygen incorporation probability that is much lower for the HFHP II regime compared to that for the LFLP and HFHP I regimes, if the lower oxygen incorporation probability is only caused by the different time scales on which the oxygen is incorporated. This model would explain the higher critical oxygen concentration observed for the HFHP II regime compared to those observed for the LFLP and HFHP I regimes. Furthermore, the reduced oxygen incorporation probability for the HFHP II regime would be caused by a slower in-diffusion of the oxygen into the plasma zone.

### 5.7.2. Impact of the deposition rate on the oxygen incorporation

For the LFLP regime an increase in deposition rate from 0.15 to 0.5 nm/s leads to a significant suppression of the oxygen incorporation whereas for the HFHP I & II regimes this effect is only very weak. Kroll et al. [Kro1995] also have seen a decrease of the oxygen incorporation probability as a function of an increasing deposition rate. They explained this reduction with a dilution of the oxygen compared to the silane radicals that are created via dissociation of silane. A higher deposition rate achieved by a higher discharge power leads to an increase in silane radicals. However, they deposited in a VHF (70 MHz) regime without hydrogen dilution at low deposition pressures (0.23 mbar) and total gas flows (40 sccm). The LFLP regime is the most similar deposition regime. Less oxygen is incorporated for a higher deposition rate / discharge power since more of the silane is utilized. The high pressure and hydrogen flow used in the HFHP I & II regimes shorten the free path length of the silicon radicals leading to an increased number of reactions of silane radicals with oxygen. This might reduce the above mentioned effect.

### 5.7.3. Material properties

The material properties of single i-layers show a different behavior for the LFLP and HFHP I regimes compared to that for the HFHP II regime (see Figure 5.3). The material properties of the HFHP I regime are already discussed in *section 4.9*. For the LFLP regime these properties are rather similar. In both regimes the critical oxygen concentration is seen for the electrical properties (increase in conductivity) at $C_O \sim 2\times10^{19}$ atoms/cm$^3$. Differences for the LFLP and HFHP I regimes are found and

the absolute values of $E_A$ are some tens of meV lower and the conductivities are up to a half of an order of magnitude higher for the LFLP regime compared to the HFHP I regime (see Figure 5.3 (a-c)).

One reason for the Different conductivities of the LFLP films compared to the HFHP I films is the higher band-gap for HFHP I of 1.96 eV compared to 1.93 eV found for LFLP (see Figure 5.3 (d)). This is in a good agreement with the solar cell parameters (Figure 5.2) as the $V_{OC}$ for the LFLP regime is about 840 meV and for the HFHP I regime at approximately 900 - 910 meV and as the $j_{SC}$ is ~ 14 mA/cm$^2$ for the LFLP regime and ~ 13 mA/cm$^2$ for the HFHP I regime. The band-gap shift is assumed to be due to the lower heater temperature for the HFHP I regime (200 °C) compared to the LFLP regime (260 °C). Furthermore, differences in hydrogen content observed for LFLP and HFHP I regimes (Figure 5.3 (f)) can be explained in that way. A high temperature during deposition leads to hydrogen effusion and thus to a lower hydrogen content in the absorber layer.

For the HFHP II regime the structural and optical properties do not differ significantly from those seen for the HFHP I regime. However, surprisingly no clear critical contamination is observed for the electrical properties. Nor at $C_O \sim 2\times10^{19}$ atoms/cm$^3$, neither at $C_O \sim 2\times10^{20}$ atoms/cm$^3$. Uncontaminated single i-layers deposited by means of the HFHP II regime have nearly the same $E_A$ and conductivities as contaminated i-layers. Unfortunately it was not possible to investigate this behavior more in detail due to adhesion problems of single i-layers deposited in the HFHP II regime

### 5.7.4. Light induced degradation

A further intention of this work was to prepare device quality a-Si:H solar cells at relatively high base pressure conditions (impurity/oxygen flows) and to investigate their light-soaking stability. The most important result concerning the stability of the solar cells is that, again, the critical oxygen concentration does not change upon light soaking. This was already seen and discussed in *chapter 4*. Thus, the critical concentration can be influenced by means of the deposition regime but not via light-soaking. However, the relative degradation of uncontaminated solar cells depends strongly on the deposition rate. Films deposited in the LFLP, HFHP I, & II regimes with deposition rates lower than 0.3 nm/s have the best stabilized solar cell efficiency of about 7 %, 7 % and 7.4 %, respectively, achieved in this work (Figure 5.4). Cells, deposited at higher rates (~ 0.5 nm/s) lose approximately 0.5 % abs. in stabilized efficiency. This is also represented in a stabilized diode quality factor of $n \sim 1.75$ for solar cells deposited at the lower deposition rate compared to $n \sim 2$ for those deposited at the higher deposition rate.

The negative aspect of high rate films can be partly attributed to, e.g., the increase in the contribution of radicals originating from multiple silicon containing molecules created by a higher applied power density. This is assumed to lead to a film structure suffering more from light irradiation [Gan2004]. Thus, especially for the LFLP regime

the gain in oxygen incorporation suppression for high rate cells is overweighed by an increased solar cell degradation after 1000 h of light-soaking.

## 5.8. Summary

For total flow rates of ~ 112 sccm (LFLP regime) and ~ 368 sccm (HFHP I regime) the critical oxygen concentration is the same as already seen in *chapter 4*, namely ~ $2\times10^{19}$ $cm^{-3}$. For a total source gas flow of ~ 1015 sccm (HFHP II regime) the critical oxygen concentration increased to $C_{O,crit}$ ~ $2\times10^{20}$ $cm^{-3}$. These critical levels are independent upon light-soaking. The critical oxygen concentration is speculated to depend on the oxygen precursor lifetime, namely $SiO_2$, siloxane, and OH or $H_2O$ molecules. For a deposition regime with a low oxygen incorporation probability more of the stable siloxanes are incorporated with respect to the hydrogen-oxygen molecules that are assumed to lead to oxygen in a doping configuration.

Furthermore it is observed that the oxygen incorporation probability is highest for the LFLP regime and lowest for the HFHP II regime, i.e., proportional to the source gas flow. Thus, it is not surprising that the critical base pressures for the three regimes increase with increasing source gas flow. This is assumed to be due to, e.g., oxygen dilution in the source gas. Also, an increase in deposition rate (i.e. discharge power) slightly decreases the incorporation probability.

# 6. Influence of impurity source on impurity incorporation

This chapter addresses the impact of different contamination sources and species on the performance of thin-film a-Si:H and μc-Si:H solar cells. For a-Si:H it is found that the critical oxygen concentration depends on the oxygen source. Incorporated into the i-layer via a chamber wall leak a critical oxygen concentration of ~ $2\times10^{19}$ $cm^{-3}$ is found whereas the incorporation via gas pipe leak leads to $C_{O,crit}$ ~ $2\times10^{20}$ $cm^{-3}$. This is assumed to be due to a formation of different oxygen containing precursors for the two leak sites that lead to different oxygen doping efficiencies in the growing i-layer.

For nitrogen no dependency of the critical concentration on the contamination source is observed. This is assumed to be due to the lack of reactivity of silane and nitrogen.

For μc-Si:H, deposited under standard conditions, also the same critical oxygen concentration of ~ 1 - $2\times10^{19}$ $cm^{-3}$ is found for both contamination sources. It is suggested that due to the high discharge power of ~ 0.5 $W/cm^2$ (for a-Si:H ~ 0.2 $W/cm^2$) the oxygen containing precursors responsible for the lower doping efficiency are completely dissociated. For μc-Si:H deposited at ~ 0.2 $W/cm^2$, contaminated via gas pipe leak, also a higher critical oxygen concentration of ~ 7 - $9\times10^{19}$ $cm^{-3}$ is observed.

## 6.1. Introduction

In the previous chapters the general impact of oxygen and nitrogen incorporation on the solar cell performance is studied. In this chapter the influence of different impurity sources is investigated. This is of importance because in a solar cell production line various leaks for atmospheric contamination are possible. It is distinguished between two major sources of contamination, namely, (a) air leakages and/or outgassing (virtual leakage) of the process chamber, i.e. extrinsic leaks and (b) leaks in the gas pipe or poor quality of the process gas, i.e. intrinsic leaks. In this study oxygen and nitrogen incorporation from these two sources are investigated and compared.

## 6.2. Process conditions of the i-layer

The amorphous i-layers are deposited with the high-flow high-pressure I (HFHP I) regime ($r_d$ = 0.5 nm/s). For details concerning this deposition regime see *section 4.3*. For the deposition of microcrystalline i-layers two regimes were used. For the deposition of μc-Si:H solar cells in the standard (reference) regime the applied discharge power was increased from 0.2 W/cm² to 0.5 W/cm², and the silane concentration was reduced from 7.8 sccm to ~ 2.4 sccm compared to a-Si:H deposition conditions. The second μc-Si:H regime had a lower discharge power of $P$ = 0.2 W/cm², compared to the reference deposition regime. In order to promote a microcrystalline film growth the silane flow was further reduced to~ 1.6 sccm.

The different impurity sources are simulated by admitting the impurity gases via a leak at a chamber wall (CWL) or in the gas pipe line (GPL), respectively (see Figure 3.2). The distance between the chamber wall leak and the plasma zone is approximately $d_{CWL}$ = 25 cm. To avoid unintended contamination, the process gases $SiH_4$ and $H_2$ (both initially with purity 6.0) are additionally led through a gas purifier. The distance of the gas pipe leak to the showerhead electrode, i.e. to the plasma zone, is $d_{GPL}$ = 50 cm. In case of the GPL no additional gas purifier is used.

For μc-Si:H deposition in a previous publication [Kil2009] structural changes to a more amorphous film growth were observed with increasing oxygen concentration. According to this study these changes at higher oxygen concentrations were compensated by a reduced silane flow.

## 6.3. Material properties

In contrast to *chapers 4 & 5* in this chapter, first the material properties are shown. For contaminated a-Si:H solar cells via CWL and GPL it is observed (see *section 6.4*) that the critical oxygen contamination levels are $C_{O,crit}$ ~ $2\times10^{19}$ cm$^{-3}$ and $C_{O,crit}$ ~ $2\times10^{20}$ cm$^{-3}$, respectively.

It is shown, that the material properties of oxygen contaminated films also reveal indications for different critical oxygen concentrations for the CWL and for the GPL, respectively. For nitrogen no differences at all are seen between GPL and CWL (not shown).

In Figure 6.1 the material properties of single i-layers contaminated by the two different oxygen leaks, namely CWL and GPL are shown. The thickness of the single i-layers is ~ 800 nm. Note, in *chapters 4 - 5* the thickness of single i-layers for material studies was 300 - 400 nm since in solar cells the i-layer thickness is also ~ 350 nm. Due to the very low conductivity of the single i-layers the scattering of the conductivity measurements was lower for the thicker films.

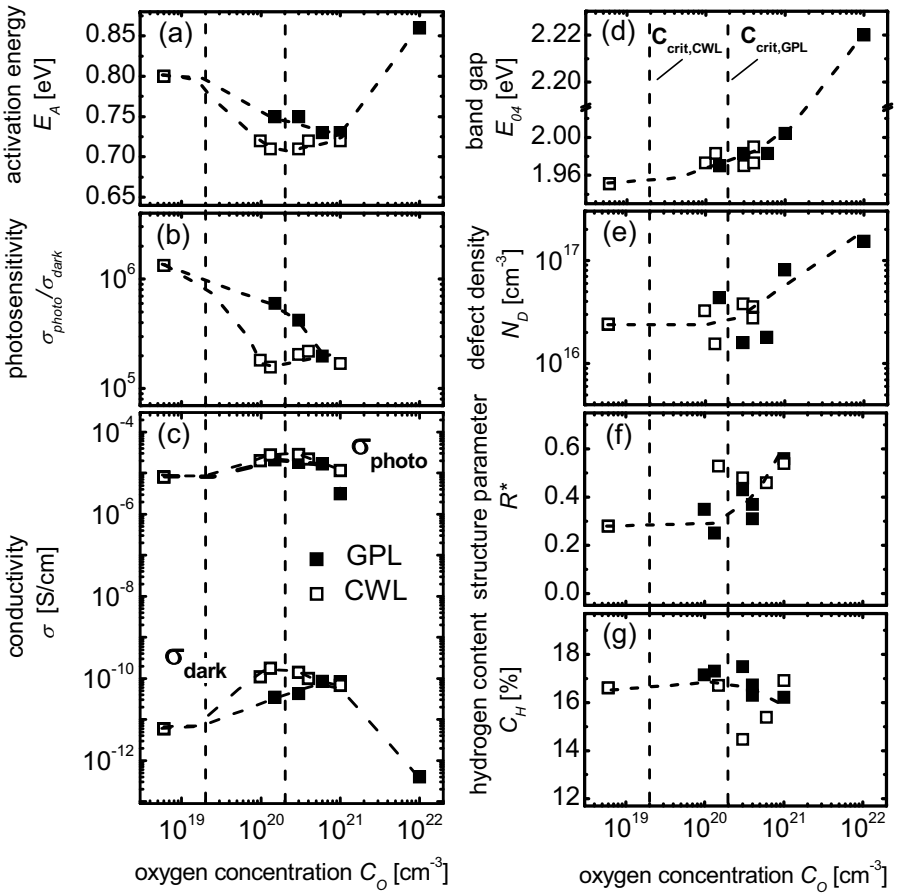


*Figure 6.1 Activation energy $E_A$ (a), photosensitivity (b), $\sigma_{photo}$ and $\sigma_{dark}$ (c), mobility band gap $E_{04}$ (d), defect density $N_D$ (e), microstructure factor R* (f), and hydrogen content $C_H$ (g) as functions of the oxygen concentration in the intrinsic a-Si:H (HFHP I) absorber layer contaminated from different sources. The left vertical dashed line represents the solar cell critical contamination level at $2\times10^{19}$ atoms/cm$^3$ observed for the chamber wall leak (CWL), the right vertical line represents the critical level in oxygen concentration for solar cells of $2\times10^{20}$ atoms/cm$^3$ for the gas pipe (GPL).*

### 6.3.1. Electrical properties

For the CWL, dark- and photoconductivities increase and $E_A$ decreases when exceeding an oxygen concentration of $2\times10^{19}$ atoms/cm$^3$, attributed to by the n-type doping character of a part of the incorporated oxygen. A drop in conductivity and an increase in $E_A$ is present at oxygen concentrations higher than $2\times10^{20}$ atoms/cm$^3$ which is assumed to be related to alloying, i.e. the formation of Si-O-Si bonds leading to an increase of the band gap (see also Figure 6.1 (d)). The decrease in $E_A$ and increase in $\sigma_{dark}$ and $\sigma_{photo}$ for oxygen concentrations above the critical oxygen contamination level

is somewhat delayed for films contaminated via GPL. This is an indication for an increased critical oxygen contamination level for GPL contaminated i-layers.

### 6.3.2. Optical properties

Figure 6.1 (d) shows the $E_{04}$-band gap values as a function of the oxygen concentration. There is no significant difference between the different types of contamination, i.e., $E_{04,GPL}(C_O) = E_{04,CWL}(C_O)$. Like for the band gap, also the defect density $N_D$ as a function of the oxygen concentration, determined by CPM measurements, is similar for the two leak sources (see Figure 6.1 (e)).

### 6.3.3. Structural properties

From IR measurements an increase in microstructure parameter $R^*$ for films with $C_O > 10^{20}$ cm$^{-3}$ is observed, irrespective of the intentional oxygen leak source. This increase is attributed to oxygen incorporation and not to, e.g., a void rich microstructure. The hydrogen content is ~ 17 % - 18 %, irrespective of oxygen concentration and oxygen source.

The similarities and differences for the CWL and GPL concerning the material properties will be discussed later.

## 6.4. Amorphous solar cells based on contaminated i-layers

It is presented in this section that for oxygen contaminated solar cells via CWL or GPL critical oxygen concentrations of $C_{O,crit} = 2\times10^{19}$ cm$^{-3}$ and $C_{O,crit} = 2\times10^{20}$ cm$^{-3}$ are found, respectively. Such a dependency of the critical concentration on the impurity source is not observed for nitrogen incorporation.

### 6.4.1. Oxygen leak

In Figure 6.2 (a-d) the initial solar cell parameters (under AM1.5, red and blue illumination) of oxygen contaminated a-Si:H solar cells are shown as a function of the oxygen concentration, measured by SIMS, for different types of impurity gas leaks. For oxygen introduced via CWL, initial efficiency and fill factor under red illumination start to decrease continuously above $2\times10^{19}$ atoms/cm$^3$. A shift of the critical oxygen contamination level of about one order of magnitude (up to $2\times10^{20}$ atoms/cm$^3$) is observed in the case of GPL. The fill factor under blue illumination, representing the p/i-interface quality, tends to remain unaffected and decrease only at oxygen concentrations significantly higher than $2\times10^{19}$ atoms/cm$^3$ for oxygen introduced through the CWL. For the GPL similar critical oxygen contamination levels are seen for the *FF* under red and blue illumination. Short circuit current density and open circuit voltage are $j_{SC}$ ~ 13 mA/cm$^2$ and $V_{OC}$ ~ 900 mV, respectively. Both parameters are less affected by the oxygen concentration. The most contaminated cells (> $2\times10^{20}$ atoms/cm$^3$) show slight losses in $j_{SC}$ and $V_{OC}$ which is

probably caused by the worsened bulk carrier extraction and alloying effects (see Figure 6.1 (d)).

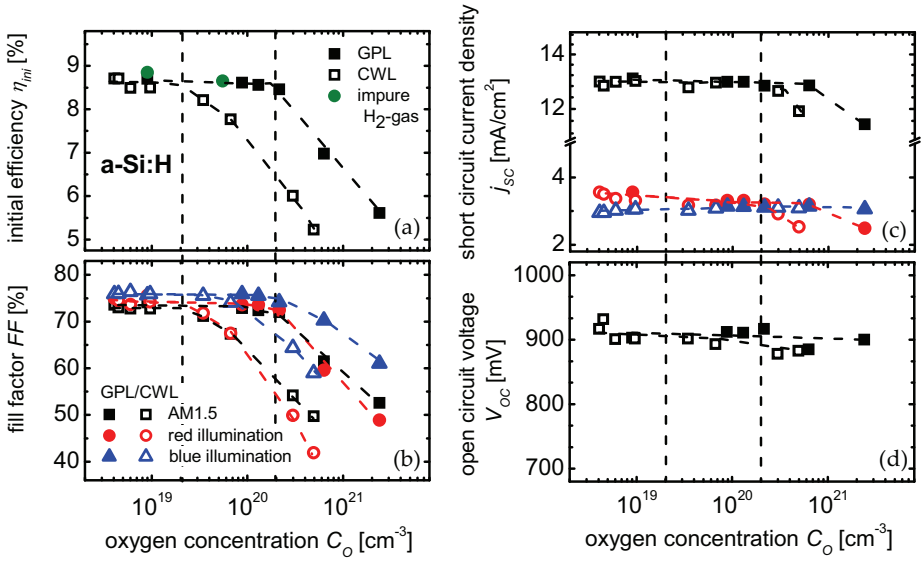


*Figure 6.2 Solar cell parameters of p-i-n a-Si:H solar cells, contaminated via CWL & GPL as a function of the oxygen concentration in the i-layer. The critical contamination level are ~ 2×10$^{19}$ atoms/cm$^3$ and ~ 2×10$^{20}$ atoms/cm$^3$ for CWL and GPL, respectively. Additionally, solar cells deposited by using impure hydrogen gasses with oxygen impurity contents of 0.17 and 3.13 ppm are shown.*

Additionally, the initial cell efficiencies of two a-Si:H solar cells (HFHP I) deposited with impure hydrogen are shown in Figure 6.2 (other parameters not shown for clarity). The two solar cells have oxygen concentrations of $C_O = 9\times10^{18}$ cm$^{-3}$ and $C_O = 6\times10^{19}$ cm$^{-3}$, respectively. These concentrations result from oxygen contents in the hydrogen of 0.17 and 3.13 ppm, respectively. Also, for the higher oxygen concentration state-of-the-art solar cells are deposited which is an indication for a similar behavior compared to that for the GPL. This point will be discussed later.

### 6.4.2. Nitrogen leak

Figure 6.3 (a-d) shows the solar cell IV-parameters measured as a function of the nitrogen concentration in the i-layer, obtained via CWL and GPL. The initial efficiency decreases with increasing impurity concentration when the critical nitrogen contamination level of about 4×10$^{18}$ atoms/cm$^3$ is exceeded, irrespective of the contamination source. The fill factor under AM1.5, red, and blue illumination starts to decrease continuously above a nitrogen concentration of ~ 4×10$^{18}$ atoms/cm$^3$. The $j_{SC}$ and $V_{OC}$ values are similar to that of oxygen contaminated films (as seen above), i.e., $j_{SC}$ ~ 13 mA/cm$^2$ and $V_{OC}$ ~ 900 mV. These values are not significantly affected when the nitrogen concentration is enhanced.

Here, one can conclude that in contrast to oxygen contamination, for nitrogen the decrease in solar cell performance is independent of the source of contamination.

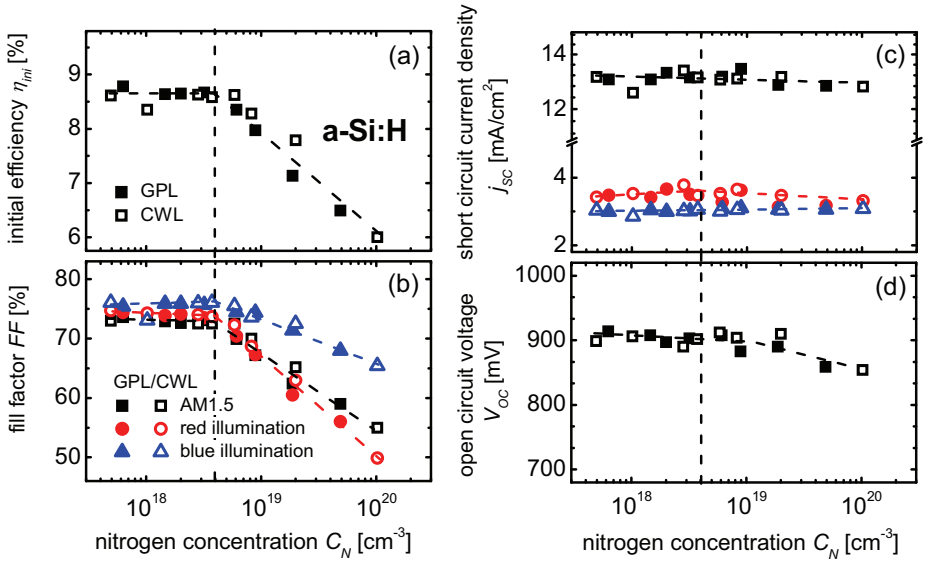


*Figure 6.3 Solar cell parameters as a function of the nitrogen concentration in the i-layer of a-Si:H solar cells obtained via CWL (open symbols) and GPL (solid symbols). The critical contamination level is at ~ 4×10$^{18}$ atoms/cm$^3$ for CWL and GPL.*

## 6.5. Microcrystalline solar cells based on contaminated i-layers

In this section it is shown, that for µc-Si:H thin-film solar cells the impact of different types of oxygen sources and of the applied discharge power on the cell performance is examined. For a high discharge power of $P$ = 0.5 W/cm$^2$ no difference in critical oxygen concentration (1 - 2×10$^{19}$ cm$^{-3}$) is found for different oxygen sources. In turn, for a discharge power of $P$ = 0.2 W/cm$^2$ the contamination via GPL leads to an enhanced critical oxygen concentration of ~ 7 - 9×10$^{19}$ cm$^{-3}$.

### 6.5.1. Impact of applied discharge power on oxygen incorporation

In the case of microcrystalline material the critical oxygen concentration level of 1 - 2×10$^{19}$ atoms/cm$^2$ does not depend on the contamination source (0.5 W/cm$^2$ deposition, see Figure 6.4). It should be noted, that the critical contamination level can not that easily be detected via the fill factor losses in this case compared to a-Si:H cells since the short-circuit current density strongly decreases for increasing impurity concentration, too. The fill factor and $j_{SC}$ decrease from 70 % to 46 % and 20 mA/cm$^2$ to 10 mA/cm$^2$ , respectively, upon an increase in oxygen concentrations from 10$^{19}$ atoms/cm$^3$ to 10$^{21}$ atoms/cm$^3$. For µc-Si:H solar cells also the $V_{OC}$ increases slightly with increasing oxygen concentration. This can be explained by the fact that the amorphous to microcrystalline transition regime is affected by the oxygen flow.

Consequently, the silane flow is reduced since high oxygen flow rates are applied during deposition in order to keep the crystalline volume fraction constant at approximately 60 – 70 % and, thus, to keep the $V_{OC}$ more or less independent of the oxygen concentration in the range of ~ 500 - 520 mV.

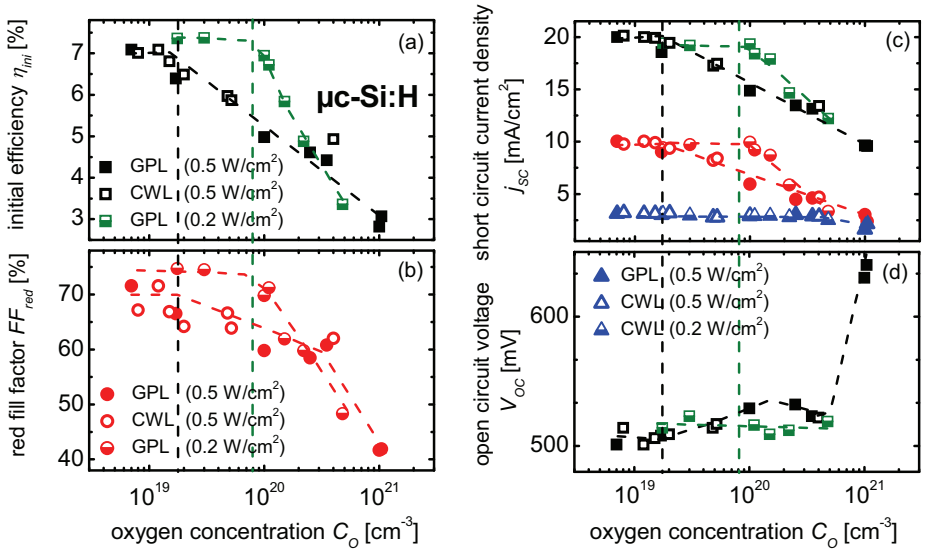


*Figure 6.4 Solar cell parameters (under AM1.5, blue, and red illumination) of p-i-n µc-Si:H solar cells contaminated via CWL & GPL as a function of the applied discharge power and of the oxygen concentration in the i-layer. The CWL & GPL (0.5 W/cm² deposition) critical oxygen contamination levels are identical at ~ 2×10¹⁹ atoms/cm³ (vertical dashed lines) The critical oxygen concentration of the 0.2 W/cm² deposition (GPL) is indicated at 7 - 9×10¹⁹ cm⁻³.*

However, if there is a dependency of the critical oxygen concentration on the discharge power this impact will be seen best for the case of the GPL since for a-Si:H an increased critical oxygen concentration was found for cells contaminated via GPL. Applying a deposition regime with reduced silane flow of ~ 1.6 sccm and reduced discharge power (0.2 W/cm²), an increased critical oxygen concentration is seen also for µc-Si:H, contaminated via GPL. The critical oxygen concentration level is shifted to 7 - 9×10¹⁹ atoms/cm³. Note, these deposition conditions lead to unfavorable low deposition rates of 0.27 nm/s. The dependency of the critical contamination levels on the discharge power will be discussed in *section 6.8*.

## 6.6. Correlation of base pressure and impurity concentration

In this section it is demonstrated that the critical base pressures of a-Si:H and µc-Si:H solar cells are different for different impurity sources. For oxygen contamination of a-Si:H and µc-Si:H solar cells it is observed that for the GPL compared to the CWL the oxygen is much more efficiently incorporated. For nitrogen this effect is much weaker.

### 6.6.1. a-Si:H solar cells

In Figure 6.5 the impurity concentration as a function of the base pressure for a-Si:H solar cells is shown for nitrogen and oxygen from the two sources, GPL and CWL. Note, for both leak sources the base pressure is determined with the same procedure described in *section 4.2.1*. Due to the different leak to pump geometries the pumping speeds of the impurities might be different leading to variations in base pressure. This impact is neglected in this study.

| oxygen | $P$ [W/cm$^2$] | $r_d$ [nm/s] | $p_{b,crit}$ [Torr] | $C_{O,crit}$ [cm$^{-3}$] |
|---|---|---|---|---|
| CWL | 0.2 | 0.50 | $7\times10^{-6}$ | $2\times10^{19}$ |
| GPL | 0.2 | 0.50 | $1\times10^{-6}$ | $2\times10^{20}$ |

*Table 6.1 Deposition parameters, critical oxygen concentrations, and critical base pressures for the CWL and for the GPL, respectively.*

Independent on the impurity species (oxygen and nitrogen) the impurity concentration increases with increasing base pressure. The critical oxygen and nitrogen concentrations derived from the solar cell data are indicated. For oxygen they are $2\times10^{19}$ atoms/cm$^{-3}$ for the CWL and $2\times10^{20}$ atoms/cm$^{-3}$ for the GPL, for nitrogen they are $4\times10^{18}$ atoms/cm$^{-3}$ for both, CWL and GPL. For nitrogen the critical contamination level does not depend on the source. The critical oxygen base pressures are found to be $p_b \sim 7\times10^{-6}$ Torr and $p_b \sim 1\times10^{-6}$ Torr for the CWL and for the GPL, respectively, even though GPL leads to an enhanced critical oxygen concentration of $\sim 2\times10^{20}$ atoms/cm$^{-3}$. Thus, the incorporation of oxygen increases strongly when the oxygen is provided to the plasma by means of GPL. In this case, up to more than one order of magnitude higher oxygen concentrations are measured by SIMS for the same oxygen flow (e.g., at a fixed base pressure of about $10^{-6}$ Torr) for GPL compared to CWL.

| nitrogen | $P$ [W/cm$^2$] | $r_d$ [nm/s] | $p_{b,crit}$ [Torr] | $C_{N,crit}$ [cm$^{-3}$] |
|---|---|---|---|---|
| CWL | 0.2 | 0.50 | $1\times10^{-5}$ | $4\times10^{18}$ |
| GPL | 0.2 | 0.50 | $5\times10^{-6}$ | $4\times10^{18}$ |

*Table 6.2 Deposition parameters, critical nitrogen concentrations, and critical base pressures for the CWL and for the GPL, respectively.*

For nitrogen the critical base pressures are $1\times10^{-5}$ Torr and $5\times10^{-6}$ Torr for the CWL and for the GPL, respectively. Consequently the incorporation of nitrogen is found to increase with a factor of about 2 for nitrogen that is introduced directly into the PECVD process together with the $SiH_4$ and $H_2$ gases compared to that introduced via CWL.

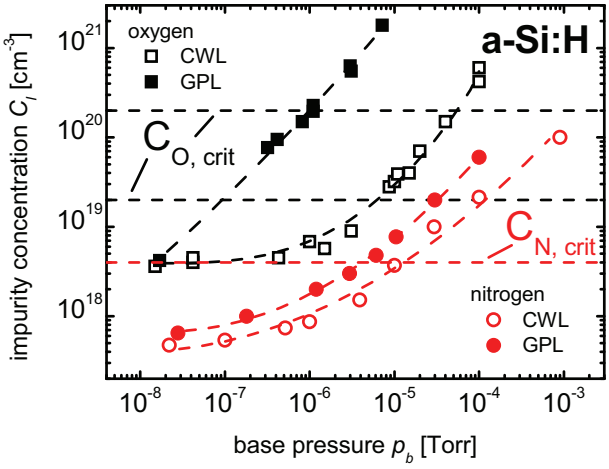


*Figure 6.5 Impurity concentration of amorphous i-layers as a function of the base pressure for oxygen (black squares) and nitrogen (red circles) i-layers contaminated via CWL (open symbols) and GPL (filled symbols). The critical oxygen and nitrogen contamination levels determined from $FF_{red}$ are indicated.*

### 6.6.2. μc-Si:H solar cells

Similar effects as described in the foregoing section for amorphous i-layers are observed for microcrystalline i-layers (deposited at 0.5 W/cm²) that are contaminated with oxygen impurities. The incorporation probability (oxygen incorporation as a function of the base pressure) is nearly the same as that obtained for a-Si:H (see Figure 6.6). Note, if not mentioned otherwise the impurity incorporation probability is defined as the amount of impurities introduced into the reactor compared to the impurity concentration found in the i-layer.

| | $P$ [W/cm²] | $r_d$ [nm/s] | $p_{b,crit}$ [Torr] | $C_{O,crit}$ [cm$^{-3}$] |
|---|---|---|---|---|
| CWL | 0.5 | 0.50 | $4\times10^{-6}$ | $1 - 2\times10^{19}$ |
| GPL | 0.2/0.5 | 0.27/0.50 | $1\times10^{-7}/1\times10^{-7}$ | $7 - 9\times10^{19}$ / $1 - 2\times10^{19}$ |

*Table 6.3 Deposition parameters, critical oxygen concentrations, and critical base pressures for the CWL and for the GPL, respectively.*

The critical oxygen contamination level of $1 - 2\times10^{19}$ atoms/cm$^{-3}$ (indicated by the dashed line in the figure) does not depend on the source of contamination. Critical base pressures are found to be $p_b \sim 4\times10^{-6}$ Torr and $p_b \sim 10^{-7}$ Torr for the CWL and for the GPL, respectively. For the deposition regime with an applied discharge power of 0.2 W/cm² (GPL) the probability of oxygen incorporation is even stronger compared to that for the GPL and discharge power of 0.5 W/cm². For the 0.2 W/cm² regime, even though the critical oxygen concentration is highest ($7 - 9\times10^{19}$ atoms/cm$^{-3}$), the critical oxygen base pressure is only $p_b \sim 10^{-7}$ Torr.

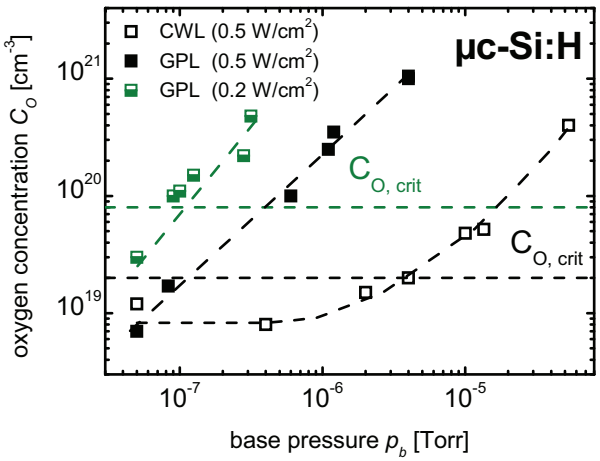


*Figure 6.6 Impurity concentration of µc-Si:H i-layers as a function of the base pressure for solar cells contaminated with oxygen via CWL (open symbols), GPL (0.5 W/cm²) (filled symbols), and GPL (0.2 W/cm²) (green, half-filled symbols). The critical oxygen contamination levels of ~ 1 - 2×10¹⁹ and ~ 7 - 9×10¹⁹ atoms/cm² determined from $FF_{red}$ are indicated.*

## 6.7. Light-induced degradation of solar cells

In Figure 6.7 (a,b) it is shown, that the above described critical contamination levels for the GPL and CWL (both a-Si:H) are not affected by light-soaking (1000 h).

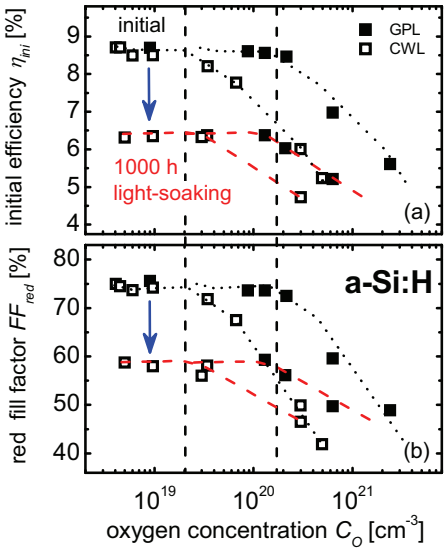


*Figure 6.7 Solar cell parameters measured under AM1.5 and red light illumination ($FF_{red}$) for oxygen contaminated intrinsic layers of a-Si:H solar cells in the initial state and after light soaking (1000 h). The critical oxygen contamination levels for CWL & GPL are not shifted significantly by the light-induced degradation.*

Considering the accuracy of the determination of the oxygen concentration, these levels stay at about $2\times10^{19}$ and $2\times10^{20}$ atoms/cm$^3$ for CWL and GPL, respectively (vertical dashed lines). Moreover, the general trend of the solar cell characteristics as a function of the oxygen concentration does not change as well for both sources after light-soaking. For both sources the reduction in stabilized efficiency is mainly caused by a decrease in fill factor, especially, for red-light illumination. Small reductions are also seen in $j_{SC}$ for CWL & GPL contaminated cells with initial efficiencies smaller than 8.5 % (not shown here).

## 6.8. Discussion

In the foregoing sections the incorporation of impurities in a-Si:H and μc-Si:H solar cells that are introduced together with the process gasses via controllable gas pipe leak (GPL) and chamber wall leak (CWL) is described. For a-Si:H it is found that the critical oxygen concentration depends on the oxygen source. Incorporated into the i-layer via a chamber wall leak (CWL) a critical oxygen concentration of ~ $2\times10^{19}$ cm$^{-3}$ is seen whereas the incorporation via gas pipe leak (GPL) leads to $C_{O,crit}$ ~ $2\times10^{20}$ cm$^{-3}$. For nitrogen no such effect is found.

For μc-Si:H, deposited in under standard conditions (0.5 W/cm$^2$), also only one critical oxygen concentration of ~ 1 - $2\times10^{19}$ cm$^{-3}$ is found. A higher critical oxygen concentration of ~ 7 - $9\times10^{19}$ cm$^{-3}$ is also observed for μc-Si:H deposited at ~ 0.2 W/cm$^2$. These findings are discussed in the following.

### 6.8.1. Solar cells

For oxygen incorporation in a-Si:H solar cells the process of incorporation depends on the source of the leakage (GPL or CWL). Using different oxygen sources for the HFHP I regime the critical oxygen contamination level can be shifted from $2\times10^{19}$ atoms/cm$^3$ (CWL) to $2\times10^{20}$ atoms/cm$^3$ (GPL). In *chapter 5* a similar shift of the critical oxygen contamination level is observed also for the CWL, if the source gas flow is increased from ~ 400 sccm (HFHP I regime) to ~ 1000 sccm (HFHP II regime), see Figure 5.2. Both effects can be explained by the same model. Furthermore, for the deposition of μc-Si:H solar cells it is seen that the critical oxygen concentration does also depend on the applied discharge power. Note, generally the applied power density for μc-Si:H deposition is much higher compared to that for a-Si:H.

**Impurity incorporation model** The higher critical oxygen concentration observed for a-Si:H contaminated via GPL (see Table 6.1) is caused by a lower amount of oxygen incorporated in doping configurations. The incorporation of certain atomic configurations in a-Si alloys during plasma deposition depends on the type of precursors in the gas phase. For example, molecules containing Si-C or Si-N groups are likely to cause Si-C and Si-N groups in the material if a plasma with a power smaller than a level necessary for a complete fractionation of the precursor species with high binding energy is applied. The binding energies of Si-C and Si-N are 4.5 eV

and 4.6 eV, respectively, and exceed that of Si-Si (≈ 2.5 eV) considerably. For Si-O, the binding energy is even higher (8.3 eV) [Ker1977]. Thus, a source of oxygen in non-doping configurations could be given by precursor molecules with Si-O-Si bonding configuration, like siloxane molecules, leading to an enhanced incorporation of oxygen in the non-doping two-fold coordination.

A likely explanation of the observations is that for the gas pipe leak such molecules form due to reactions of oxygen with silane outside of the plasma region since the reactivity of molecular oxygen with silane is very high [Mat2002]. Apparently, less of these molecules would form in case of the chamber wall leak, possibly because in this case the oxygen encounters a more silane-depleted reaction gas with lower probability of siloxane-type molecules to form. Alternatively, it is also possible, that oxygen coming from the chamber wall leak reacts with atomic or molecular hydrogen forming OH or $H_2O$. Atomic hydrogen is a predominant gas species in a silane depleted reactor next to the plasma zone after stabilization of the process conditions. Note, in the plasma zone the silane is even more depleted with respect to the rest of the reactor volume (i.e. the vicinity of the CWL) but nevertheless, in the rest of the reactor the silane depletion is still higher than in the source gas supply line. These species (OH and $H_2O$) are assumed to be precursors for the incorporation of oxygen in doping configurations.

Following these two explanations, the level of silane depletion and the presence of atomic hydrogen, both in the vicinity of the intentional leak, are of importance for the critical oxygen concentration. Explained by this model, the incorporation of oxygen in doping configuration is strongly reduced for GPL in comparison to CWL. Furthermore, irrespective of the oxygen source, alloying is observed by photothermal deflection spectroscopy (PDS, Figure 6.1, (d)) for oxygen concentrations $> 10^{20}$ atoms/cm$^{-3}$ [Woe2008] & [Mor1991]. This might play also an important role for solar cell deterioration, especially if the critical oxygen concentration as $\sim 2\times10^{20}$ atoms/cm$^{-3}$.

For nitrogen contamination the decrease in a-Si:H solar cell performance with increasing impurity concentration does not depend on the source of contamination (see Table 6.2). This behavior indicates that the same incorporation method is present for both types of nitrogen sources. It is known that molecular nitrogen does not react with silane without additional extern energy [Mat2002]. Therefore, high-energy plasma conditions are required for these reactions.

The very encouraging results on a-Si:H solar cells that are described above could not be obtained for the contamination of μc-Si:H solar cell deposited in the standard deposition regime (0.5 W/cm$^2$). On the one hand, the strongly enhanced incorporation probability for GPL compared to CWL (see Figure 6.6) is also observed for μc-Si:H (see Table 6.3). In general, a slight difference is given by the increased incorporation probability of oxygen into μc-Si:H i-layers compared to that for the a-Si:H layer. On the other hand, in contrast to a-Si:H, the critical oxygen contamination level of $2\times10^{19}$ atoms/cm$^3$ that is found for μc-Si:H solar cells deposited at high-flow, high-pressure and at a high discharge power of 0.5 W/cm$^2$ (Figure 6.4) does not depend on the oxygen source. One possible explanation for this result is

given by the higher applied discharge power (0.5 W/cm$^2$ for μc-Si:H and 0.2 W/cm$^2$ for a-Si:H) needed for deposition of μc-Si:H i-layer. This might lead to a dissociation of siloxanes or other species formed in the gas pipe promoting electronically non-active bonding configurations in the solid. As a result the situation is the same for CWL and GPL and no difference in oxygen incorporation is observed.

To obtain an effect similar to that observed for a-Si:H solar cells μc-Si:H cells are deposited in an industrial non-relevant μc-Si:H regime (low deposition rate) with a lower applied discharge power of 0.2 W/cm$^2$. Here, an upward shift of the critical oxygen concentration from 1 - 2×10$^{19}$ for the high discharge power to 7 - 9×10$^{19}$ cm$^{-3}$ for the low discharge power, respectively, is obtained for the GPL (see Figure 6.4). This supports the argument for the absent shift of the critical concentration for cells deposited with a high discharge power of 0.5 W/cm$^2$ that are contaminated via CWL and GPL.

**Material properties** The model of reduced oxygen incorporation in electronically active states for the GPL is supported by the electrical properties of single i-layers (see Figure 6.1 (a-c)). The increase in dark conductivity and decrease in activation energy with increasing oxygen concentration for the CWL i-layers is observed at 2×10$^{19}$ oxygen atoms/cm$^3$. For the GPL this impact of the impurities on the electrical properties seems to be slightly shifted to higher oxygen concentrations in i-layers, namely to $C_O$ ~ 2×10$^{20}$ cm$^{-3}$. Additionally, at ~ 2×10$^{20}$ oxygen atoms/cm$^3$ the electrical properties are the same for both sources of contamination, caused by a dominating alloying effect.

Material properties which are independent of the doping efficiency (e.g., band-gap $E_{04}$, microstructure parameter $R^*$, and hydrogen content $C_H$) are very similar for both sources of contamination (see Figure 6.1 (d-g)). This is not surprising since the fraction of oxygen in doping configuration is assumed to be ~ 0.5 ‰ for the HFHP I regime, i.e. most of the oxygen is incorporated electronically inactive dominating the structural and optical properties.

**Impurity concentration vs. base pressure** The increase in critical oxygen contamination level up to 2×10$^{20}$ atoms/cm$^3$ observed for a-Si:H solar cells intentionally contaminated via GPL is not reflected in an increased tolerable base pressure. Note, in this study also for the GPL the impurity flow rate was determined via the base pressure (see *section 4.2.1*). In reality, this base pressure corresponds to the amount of impurities in the source gas, i.e. to the source gas purity (excluding a gas pipe leak). When inserting the oxygen directly into the plasma via GPL the incorporation probability is strongly increased (see Figure 6.5). As a consequence, the critical base pressure is reduced from 7×10$^{-6}$ Torr to 10$^{-7}$ Torr. This can be explained by the fact that for the CWL there is a higher probability for the oxygen not to reach the plasma zone compared to the case of the GPL. For example, the oxygen could form $SiO_2$–clusters before reaching the plasma zone and drop to the bottom of the reactor.

Nonetheless, using process gasses with a lower purity than 6.0 does not mandatorily affected the solar cell parameters of a-Si:H solar cells and can lead to deposition of state-of-the-art solar cells. This, in turn, could reduce production costs. This fact has also been demonstrated by using oxygen contaminated hydrogen (3.17 ppm → purity ~ 5.5) as process gas, see Figure 6.2.

For nitrogen, the incorporation probability is slightly higher for nitrogen (factor of ~ 2 - 4) for GPL compared to CWL. This difference might be caused by a higher percentage of molecules reaching the plasma region when directly inserted via GPL.

**Light-induced degradation** It is shown in *section 6.7* that after light-soaking (1000 h) the general trends and critical oxygen contamination levels do not change within the accuracy of the measurement (see Figure 6.7). Since there are no fundamentally new results concerning the light-induced degradation for a discussion of the light-soaked cell performance at this place it is referred to *section 5.7.4*. There, the general effects of impurity contamination on the long-term stability are discussed.

## 6.9. Summary

The critical oxygen concentration in thin-film solar cells depends on the source of contamination and on the applied discharge power. These parameters are decisive for the composition of precursors for oxygen incorporation. A high concentration of siloxane compared to OH / $H_2O$ molecules is assumed to promote electronically inactive oxygen incorporation. A high siloxane density can be achieved on various ways. First, if the oxygen is inserted into the gas supply line a high amount of siloxane is formed due to a reaction of oxygen with the non silane-depleted process gas. Second, a low plasma power density does not dissociate the siloxane that is present in the plasma zone. Third, in *chapter 5*, it was seen that, if the in-diffusion of the oxygen precursors (siloxane and OH / $H_2O$) into the plasma zone takes a long time (deposition regime) the longer lifetime of the siloxane compared to that of OH / $H_2O$ leads to an increased siloxane concentration in the plasma zone.

Values between $2\times10^{19}$ and $2\times10^{20}$ $cm^{-3}$ are found for GWL and GPL for a-Si:H, respectively. For μc-Si:H values between $1 - 2\times10^{19}$ and $7 - 9\times10^{19}$ atoms $cm^{-3}$ are found for CWL and GPL, respectively.

For nitrogen due to its lack of reactivity with silane only one constant critical contamination level is found, namely $C_{N,crit} \sim 4\times10^{18}$ $cm^{-3}$, as already seen in *chapter 4*. The critical concentrations do not change upon light-soaking.

Finally, it is successfully demonstrated that good quality a-S:H p-i-n solar cells with initial efficiency $\eta_{ini} = 8.5$ % and fill factor $FF = 72$ % can be deposited with $2\times10^{20}$ oxygen atoms/$cm^3$ in the absorber layer for GPL. In comparison, the same amount of oxygen atoms introduced by CWL results in solar cells with reduced quality ($\eta_{ini} = 6$ %, $FF = 54.2$ %).

# 7. Impurity incorporation mechanisms

In this chapter a deeper insight into the incorporation mechanisms of impurities is provided. This is done considering the impurity distribution coefficient $d_I$ defined as the ratio of solid phase impurity fraction to gas phase impurity fraction for oxygen and nitrogen species. It is seen that the distribution coefficient of nitrogen behaves similar compared to that for arsenic and phosphorus that are also group V elements, like nitrogen. Their distribution coefficients can be nicely interpreted by the model of the distribution coefficient introduced in *chapter 2*. In turn, for oxygen the model is questionable and the effect of alloying requires an expansion of the model. For nitrogen alloying is not excluded, but in this work no such effect is seen.

Furthermore, it is suggested that the oxygen doping efficiency probably is much lower compared to that for nitrogen due to a very irregular incorporation of oxygen in electronically non-active states. In this study it is also found that the different oxygen doping efficiencies observed for the LFLP and HFHP I regimes compared to that for the HFHP II regime might be correlated that the ratio of regular active to non-active incorporated oxygen that must be much lower for the HFHP II regime compared to that for the LFLP and HFHP I regimes. Furthermore, it is seen that it is possible to estimate the critical oxygen base pressure solely by means of the oxygen distribution coefficient. However, further investigations are necessary to confirm and explain this result.

## 7.1. Introduction

The incorporation of arsenic and phosphorus into intrinsic a-Si:H was extensively studied by Winer et al. [Win1990] of which a summary is given in *chapter 2*. For these two impurities they developed a model of the so called distribution coefficient, given by $d_I = X_{S,I}/X_{G,I}$. $X_{G,I}$ is the gas phase fraction of the impurity and $X_{S,I}$ is the solid phase fraction of the impurity. Furthermore, in the model of the distribution coefficient introduced by Winer et al., $d_I$ consists of a regular and of an irregular part. They suggest the regular part to be proportional to the amount of impurities that are

regularly incorporated and are doping or non-doping, depending on the thermodynamical equilibrium.

Apart from the regular incorporation there is an irregular incorporation whose growth mechanisms are controversy discussed and not yet fully understood [Win1990]. This irregular part describes the impurities that can not be electronically active. These configurations are very stable due to their irregular incorporation, e.g., in complexes with hydrogen. Furthermore, their rate is dependent on $X_{G,I}$ which is speculated to be due to a rate limiting impact of the surface attachment and ionisation process of the impurity precursors.

In this chapter this model is applied for the incorporation of oxygen and nitrogen into a-Si:H in order to find out similarities and differences compared to the incorporation of As and P.

## 7.2. Determination of distribution coefficient

The distribution coefficient $d_I = X_{S,I}/X_{G,I}$ is defined by the ratio of solid phase fraction $X_{S,I}$ of the impurity to gas phase fraction $X_{G,I}$ of the impurity. For $X_{S,I}$ the concentration of the impurity (measured by SIMS), silicon (~ $5\times10^{22}$ $cm^{-3}$, [Lan1992]), and hydrogen (measured by means of FTIR) are of interest. To calculate $X_{G,I}$ the gas flow rates of the impurity, silane, and hydrogen are needed, assuming similar pumping speeds and a homogeneous gas mixture for these species. Note, the assumption for a homogeneous mixture of oxygen with the process gas is probably not accurate since in the *chapter 5* it is suggested that oxygen will react with silane before entering the plasma zone. A part of these reaction products ($SiO_2$) drops to the bottom of the reactor in form of dust and, thus, will never homogeneously mix with the process gas. However, this induces that the absolute value of the oxygen distribution coefficient might be underestimated. This aspect has to be considered when comparing the different deposition regimes since different amounts of oxygen might not reach the plasma zone for different deposition regimes.

The flow rates of silane and hydrogen are read out from the mass flow controllers (MFC). Since the impurity flows are very small in this study they could only be quantified by measuring the base pressure (see *section 4.2.1*). In order to determine the impurity flow rates the increase of the base pressure with time t for closed high-vacuum valves is recorded. With this procedure the impurity flow $\Phi$ can be determined if the reactor volume is known. In Figure 7.1 the relation between base pressure (increased by an oxygen flow into the chamber) and the determined oxygen flow is shown. For base pressures below ~ $10^{-7}$ Torr the determination of the oxygen flow was rather uncertain and a minimal oxygen flow of $10^{-4}$ sccm (≈ $1.5\times10^{-6}$ mbar l/s) is assumed since solar cells that are deposited below these base pressures showed very similar oxygen concentrations.

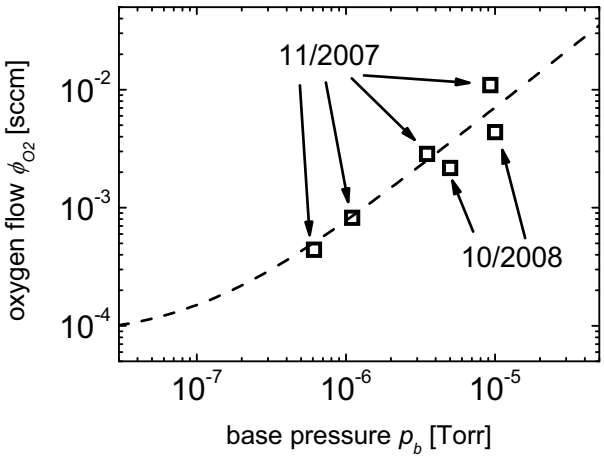


*Figure 7.1 Dependence of the base pressure, caused by an intentional oxygen flow into the chamber and the oxygen flow. Scattering of the data can be explained by a replacement of the vacuum gauge in 2008.*

Sources of this constant oxygen flow may be the outgassing of oxygen from the chamber walls or a small amount of oxygen brought into the process by the source gasses silane or hydrogen. The latter is not detectable by means of the above described procedure but also this flow is present during the fabrication of solar cells. The small difference between the two measurements shown in Figure 7.1 (11/2007 and 10/2008) can be explained by the replacement of vacuum gauges used to establish the desired base pressure. During the study of oxygen contaminated i-layers it has turned out that the oxygen in the chamber slowly abuses the vacuum gauge which therefore has to be changed from time to time. To check the reliability of the vacuum gauge from time to time the relation of impurity concentration in the i-layer to oxygen base pressure is checked. Generally, the applied oxygen flows are rather low, in all cases they are lower than 0.1 sccm.

## 7.3. Nitrogen distribution coefficient

Figure 7.2 shows the distribution coefficient vs. gas phase molecule fraction for nitrogen contamination via chamber wall leak (CWL). The deposition regime is the HFHP I regime with a deposition rate of about 0.4 - 0.5 nm/s. As a guide to the eye, the critical nitrogen gas phase fraction which represents the maximal nitrogen gas phase fraction leading to a deposition of good solar cells is indicated by a red circle.

In order to compare the distribution coefficients of nitrogen, with that of phosphorus and arsenic, values of $d_{reg}$ and $\beta$ obtained in [Win1990] are used to plot their distribution coefficients. For this plot, the deposition rates of a-Si:H contaminated with As and P from $AsH_3$ and $PH_3$ source gases, respectively, are set to $r_d \sim 0.45$ nm/s ($d_I = d_{reg} + \beta\ (X_{G,I})^{1/2}/r_d$ depends on the deposition rate). The regular part of the nitrogen distribution coefficient and the nitrogen irregularity factor $\beta$ are

obtained from a fit of the experimental results shown in Figure 7.2 according to $d_N = d_{reg} + \beta \cdot (X_{G,N})^{1/2}/r_d$. The data are given in Table 7.1.

| | $d_{reg}$ | $\beta$ [nm/s] |
|---|---|---|
| N | 0.9 | 0.0048 |
| P | 3 | 0.0009 |
| As | 8 | 0.0130 |

*Table 7.1 Values for $d_{reg}$ and $\beta$ for N, P, and As. For N the values are experimentally determined, for P and As the values are taken from [Win1990]*

The regular part $d_{reg}$ is smallest for nitrogen ($d_{reg} = 0.9$), larger for phosphorus ($d_{reg} = 3$), and largest for arsenic ($d_{reg} = 8$). The irregularity coefficient of N ($\beta = 0.0048$ nm/s) lies between those of P ($\beta = 0.0009$ nm/s) and As ($\beta = 0.0130$ nm/s). In the periodic table of elements N, P, and As are group-V elements and it is assumed, that their distribution coefficients are comparable. For a discussion of these results it is referred to *section 7.5.1*.

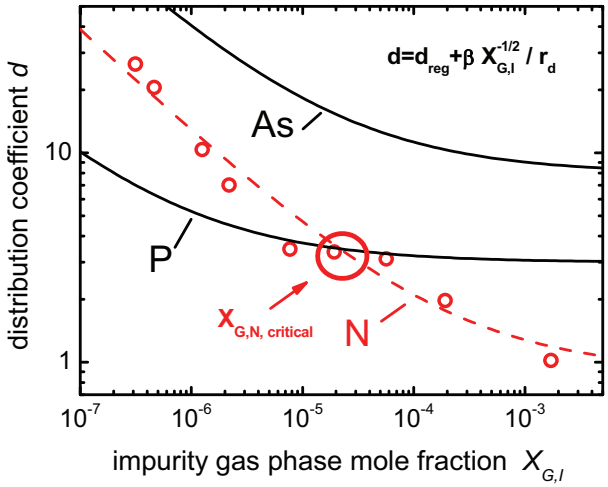


*Figure 7.2 Distribution coefficient for the HFHP I regime as function of the gas phase mole fraction $X_{G,I}$ (open circuits). The critical $X_{G,N}$ at $X_{G,N} \sim 1 - 4\times10^{-5}$ is indicated by the red circle. The dashed line is a fit of the experimental data according to equation given in the graph (for fit values see Table 7.1). The two black lines represent the distribution coefficients of arsenic and phosphorous, taken from [Win1990].*

## 7.4. Oxygen distribution coefficient

For the oxygen distribution coefficient three main results are found and are presented in this section. First, if the model for the distribution coefficient by Winer et al. is applicable for oxygen, for the LFLP and HFHP I regimes the regular part of the distribution coefficient $d_{reg}$ is found to be ten times higher than for the HFHP II regime . Second, the irregularity factor $\beta$ is much higher for oxygen compared to that

for, e.g., As or P. Third, there is an increase in $d_O$ for $C_O > C_{O,crit}$ with an increasing oxygen gas phase fraction in the source gas. This behaviour is not seen for nitrogen, arsenic, and phosphorus. Here, a deviation from the above mentioned model is obvious.

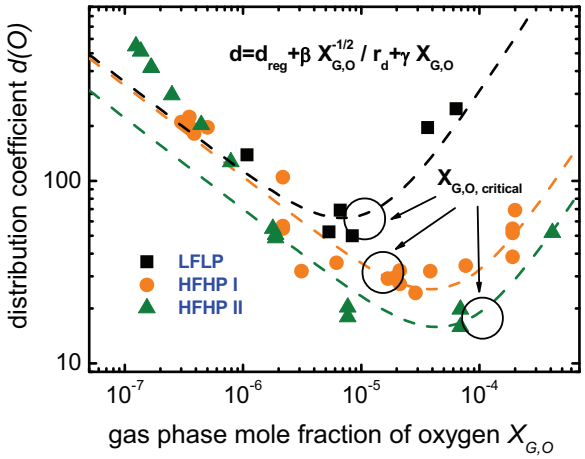


*Figure 7.3 Distribution coefficient for oxygen incorporation in a-Si:H as a function of the gas phase mole fraction of oxygen. The critical $X_{G,O}$ for these three regimes are indicated by the black circles at $X_{G,O} \sim 7 - 13\times10^{-6}$, $X_{G,O} \sim 9 - 19\times10^{-6}$, and $X_{G,O} \sim 7 - 14\times10^{-5}$ for the LFLP, HFHP I & II regimes, respectively. The dashed lines are fits of the experimental data (filled symbols) according to equation (2.5) given in the graph.*

In Figure 7.3 the oxygen distribution coefficient is shown as a function of the oxygen gas phase fraction $X_{G,O}$ for the LFLP, HFHP I & II regimes for standard deposition conditions already used in *chapter 5*. The deposition rates are 0.15 nm/s, 0.5 nm/s and 0.44 nm/s, respectively and the impurities are introduced via CWL. As a guide to the eye, the critical oxygen gas phase fractions which represents the maximal oxygen gas phase fraction leading to a deposition of good solar cells is indicated by black circles. With increasing oxygen gas phase fraction, first the distribution coefficient decreases with increasing $X_{G,O}$ until a minimum is reached. Up to this point the behaviour of the distribution coefficient as a function of $X_{G,O}$ is similar to that for N, P, and As. Above the critical $X_{G,O}$ level the distribution coefficient increases with increasing $X_{G,O}$. This means that there are differences for oxygen incorporation compared to N, P, or As incorporation.

In order to evaluate the applicability of the model by Winer et al. this aspect is implemented into the model by empirically adding a factor $X_{G,O} \times \gamma$ to the equation of the distribution coefficient presented in *chapter 2*. With this implementation the obtained data for the oxygen leak are fitted. The results are presented in the following and they are discussed in *section 7.5.2*

### 7.4.1. Regular distribution coefficient

The regular part of the oxygen distribution coefficient, the irregularity factor $\beta$, and the factor $\gamma$ are obtained from a fit of the experimental results shown in Figure 7.3 according to $d_O = d_{reg} + \beta(X_{G,O})^{1/2}/r_d + X_{G,O} \times \gamma$. The data are given in Table 7.2. $d_{reg}$, proportional to the amount of oxygen incorporated in the a-Si:H intrinsic layer that is independent of the gas phase fraction, is determined from the experimental results obtained at higher gas phase fractions $X_{G,O}$. In this regime the fit is hardly affected by experimental errors like an imprecisely determined irregularity factor $\beta$. One should note that the increase of $d_O$ has an influence on the fit quality of $d_{reg}$, especially for the LFLP regime. Nevertheless, general trends can by seen. Due to these uncertainties only a rough estimate of upper and lower limit for $d_{reg}$ is possible (see Table 7.2).

| | $d_{reg}$ | $\beta$ [nm/s] | $\gamma$ | $C_O$ [cm$^{-3}$] |
|---|---|---|---|---|
| LFLP | 0.10 - 4.0 | ~ 0.02 | $3.0\times10^{-6}$ | ~ $2\times10^{19}$ |
| HFHP I | 0.12 - 3.0 | ~ 0.05 | $2.2\times10^{-5}$ | ~ $2\times10^{19}$ |
| HFHP II | 0.01 - 0.5 | ~ 0.03 | $1.2\times10^{-5}$ | ~ $2\times10^{20}$ |

*Table 7.2 Values for $d_{reg}$, $\beta$, $\gamma$, and $C_O$ for the LFLP, HFHP I, and HFHP II regimes, respectively.*

For the LFLP and HFHP I regimes $d_{reg}$ ranges from $d_{reg} \approx 0.10$ - 4 and $d_{reg} \approx 0.12$ - 3, respectively. Although the range of $d_{reg}$ is rather large, the ratio of the distribution coefficients for the LFLP and HFHP I regimes is approximately one. For the HFHP II regime the limits of the regular distribution coefficient are much smaller, i.e. $d_{reg} \approx 0.01$ - 0.5. Additionally, the ratio of the distribution coefficients for the LFLP or HFHP I regimes to the distribution coefficient for the HFHP II is always approximately ~ 10.

### 7.4.2. Irregularity factor & $\gamma$-factor

For the irregularity factor $\beta$ it is seen that this value is higher for oxygen incorporation compared to that for phosphorus ($\beta = 0.0009$ nm/s), arsenic ($\beta = 0.0130$ nm/s), and nitrogen ($\beta = 0.0048$ nm/s) incorporation. This can be an indication for a lower doping efficiency of oxygen compared to phosphorus, arsenic, and nitrogen but this will be discussed later. The irregularity factor $\beta$ is highest for HFHP I ($\beta = 0.05$ nm/s) and lower for the HFHP II and LFLP regimes ($\beta \sim 0.03$ nm/s & $\beta \sim 0.02$ nm/s).

For LFLP the $\gamma$-factor is by far the highest ($\gamma = 3\times10^6$). For HFHP I & II the values are $\gamma = 2.2\times10^5$ and $\gamma = 1.2\times10^5$, respectively. The responsible growth mechanisms are discussed later.

### 7.4.3. Distribution coefficient as a function of the base pressure

An interesting aspect presented in this section is the correlation between distribution coefficient and base pressure. It is seen in this work that the critical base

pressures corresponds directly to the base pressure at which the distribution coefficient has its minimal value.

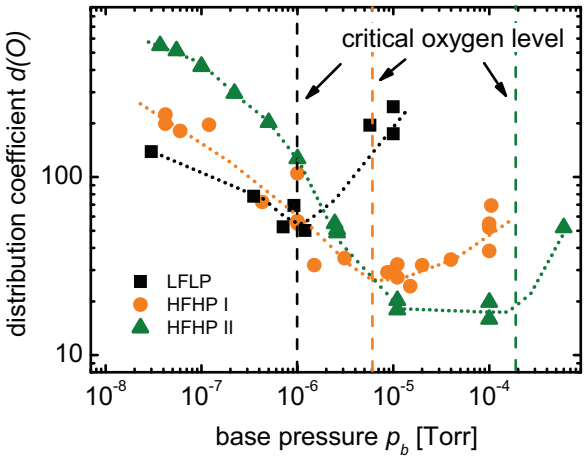


*Figure 7.4 Distribution coefficient for oxygen incorporation in a-Si:H deposited by LFLP, HFHP I & II regimes as a function of base pressure. The critical base pressure for the performance of p-i-n solar cells for the three regimes are indicated by the vertical lines, they are at $10^{-6}$ Torr, $7\times10^{-6}$ Torr, and $2\times10^{-4}$ Torr for LFLP, HFHP I & II, respectively. The dotted lines are guides to the eye.*

In Figure 7.4 the distribution coefficient is shown as a function of the base pressure for the LFLP, HFHP I & II regimes. For the three deposition regimes the general trend of $d_O$ versus base pressure is very similar. For small base pressures the distribution coefficient for oxygen incorporation in a-Si:H decreases rather strongly with increasing base pressure from about 120 (nominally uncontaminated films) to about 40 - 50 for the LFLP regime, form about 200 to 30 for the HFHP I regime and from 500 to even lower values of 10 - 20 for the HFHP II regime, respectively. The lowest values for $d_O$ are obtained approximately at the critical base pressure seen for solar cell performance. In Figure 7.4 these critical oxygen base pressures for solar cell i-layers are marked for the three regimes at approximately $10^{-6}$ Torr, $7\times10^{-6}$ Torr, and $2\times10^{-4}$ Torr for the LFLP, HFHP I & II regimes, respectively. Above the critical base pressure levels the distribution coefficient starts to increase for all regimes. At the critical base pressure levels the distribution coefficient is highest for LFLP and lowest for HFHP II.

## 7.5. Discussion

The results of the foregoing sections show that the nitrogen distribution coefficient $d_N$ seems to be comparable with $d_I$ of other group-V elements like As or P. For oxygen the model of the distribution coefficient is questionable and had to be extended for a description of alloying that is observed for a high oxygen

concentration. A direct comparison of oxygen and nitrogen is difficult due to the significant impact of alloying on the oxygen distribution coefficient.

### 7.5.1. Nitrogen leak

The aim of this chapter was to get a better insight into the doping mechanisms of impurities. Therefore, first, a comparison of the nitrogen distribution coefficient with those found for arsenic and phosphorus by [Win1990] is made. The first observation was that the distribution coefficients of N, P, and As behave in a similar way as a function of the gas phase impurity fraction $X_{G,I}$. This leads to the assumption that also the incorporation of N, P, and As into a-Si:H proceeds on a similar way. This was assumed since these N, P, and As all are group V elements. With these prerequisites the experimental data of the nitrogen distribution coefficient is fitted according to the model of the distribution coefficient developed for the elements As and P by [Win1990]. Thus, if the model is applicable to nitrogen, which is assumed, the incorporation mechanisms of nitrogen can be studied.

It was found that the regular part of the distribution coefficient increases from $d_{reg} = 0.9$, $d_{reg} = 3$, to $d_{reg} = 8$ for N, P, and As, respectively. A look onto the periodic table of elements reveals that nitrogen is the smallest group-V element and arsenic is the biggest. From these results it can be stated that the regular distribution coefficient for Group V elements might be linked to the atomic size of the impurity. Heavy atoms are more likely incorporated in a regular site according to the regular incorporation model by [Win1990] compared to small atoms. For these sites the ratio of doping and non-doping impurities is determined by thermodynamics.

For the irregular incorporation the dependency of $d_{irreg} \sim X_{G;I}^{-1/2}$ is seen for As, P, and also in this study for N. For As and P this dependency is explained by an incorporation from $AsH_3$ and $PH_3$, respectively, as As-$H_n$ or P-$H_n$ complexes. The rate limiting step is assumed to be, e.g., the surface attachment at a-Si:H dangling bond and ionisation process of the $AsH_3$ or $PH_3$ molecule, respectively. This model is explained more detailed in *chapter 2* and leads to the observed $d_{irreg} \sim X_{G;I}^{-1/2}$. Note, in this study the impurity was introduced in form of $N_2$-molecules. It is conceivable that the nitrogen molecule is decomposed in the plasma and reacts to $NH_3$ with the surrounding atomic hydrogen. Next, a similar incorporation mechanism of $NH_3$ compared to that for $AsH_3$ or $PH_3$ might be possible explaining $d_{irreg} \sim X_{G;I}^{-1/2}$. However, in this field more work is needed to fully understand the nitrogen incorporation behaviour. Nonetheless, if also for nitrogen the incorporation of very stable, electronically non-active states can be described like for As and P a comparison of their irregularity factors of these elements makes sense. For arsenic the irregularity factor ($\beta = 0.013$ nm/s) is highest, for nitrogen ($\beta = 0.0048$ nm/s) it is still rather high and for phosphorus ($\beta = 0.0009$ nm/s) it is very low. Consequently, many atoms of the arsenic and nitrogen are incorporated in a non-active, stable configuration.

The high value of $\beta = 0.0048$ nm/s for nitrogen with respect to $\beta = 0.0009$ nm/s for phosphorus might contribute to the low doping efficiency of nitrogen compared to that found for phosphorus. Note, the critical nitrogen concentration is ~ $4\times10^{18}$ cm$^{-3}$ leading to an increase in conductivity of less than one order of magnitude. At a similar concentration of phosphorus the conductivity of the doped a-Si:H film would be increased by a much higher factor [Str1991]. The relation between the solid phase doping efficiency and the distribution coefficient is given according to [Win1990]

$$\eta_{S,\mathrm{I}} = \frac{c}{d_{\mathrm{I}}\sqrt{X_{G,\mathrm{I}}}} = c\cdot\left(d_{reg}\sqrt{X_{G,\mathrm{I}}} + \frac{\beta}{r_d}\right)^{-1}. \qquad (7.1)$$

The constant $c$ accounts for the ratio of doping to non-doping regular sites. If $c$ is similar for different elements this equation implies that low values of $d_{reg}$ and $\beta$ are a prerequisite for a high doping efficiency. Here, the astounding observation is that nitrogen has a lower regular distribution coefficient compared to those of P and As. These findings imply a further statement: Since nitrogen is assumed to have a much lower doping efficiency compared to that for phosphorus the constant $c$ must be larger for phosphorus incorporation, i.e. for thermodynamic equilibrium conditions the ratio of doping to non-doping regular incorporated impurities must be larger for P compared to that for N.

In summary, this model could support the assumption that a part of the incorporated nitrogen is in fact incorporated in an electronically active site. However, the doping efficiency of nitrogen compared to those of phosphorus and arsenic is rather poor and this fact is not completely explained by the distribution coefficient. Further experiments for the determination of the constant $c$ would be necessary.

### 7.5.2. Oxygen leak

For oxygen incorporation the distribution coefficient has a different behaviour as a function of the gas phase impurity fraction compared to that for, e.g., nitrogen. At low $X_{G,\mathrm{I}}$ the behaviour of $d_{\mathrm{O}}$ is comparable to that of nitrogen but above the critical oxygen gas phase fraction $X_{G,\mathrm{I},crit}$ the oxygen distribution coefficient starts to increase with increasing $X_{G,\mathrm{I}}$. Note, $X_{G,\mathrm{I},crit}$ is the maximum of the gas phase fraction of oxygen that allows the deposition of state-of-the-art solar cells. Nevertheless, the oxygen distribution coefficient is fitted the oxygen distribution coefficient as a function of $X_{G,\mathrm{I}}$ according to the model of [Win1990]. To account for the increasing distribution coefficient a factor of $\gamma \times X_{G,\mathrm{I}}$ is added to the distribution coefficient. If this extended model for the oxygen distribution coefficient holds true, the mechanisms of the oxygen incorporation that could lead to this form of the distribution coefficient are the following.

Like for the regular incorporation of As, P, and N, also a regular incorporation of oxygen is conceivable. In this case, the oxygen is incorporated two-fold or three-fold coordinated, i.e. electronically non-active or active, respectively. The occupation of these two regular sites is controlled by thermodynamics. However, also an

electronically active incorporation in four-fold coordination of OH molecules is conceivable [Woe2010]. The irregular part of the distribution coefficient in this case consists of two parts. The first might be explained according to the model of [Win1990]. The inserted $O_2$-molecule might be decomposed and react to $H_2O$. The water molecule can attach to a Si-dangling-bond if ionised. This process would lead to the observed $d_{irreg} \sim X_{G;I}^{-1/2}$ for low $X_{G,I}$. The second part of the irregular incorporation is new to the model and a possible explanation of the additional factor can be the significant alloying observed for high oxygen gas phase fraction. The influence of alloying on the distribution coefficient might be, e.g., caused be a changed material structure. If the oxygen concentration in the material exceeds a certain limit, e.g., the chemical composition of the film might change. Onto this material the oxygen incorporation probability might be different and, thus, lead to a change in the distribution coefficient. It cannot be excluded that the plasma properties might be influenced by a high amount of oxygen in the plasma zone. This would influence the distribution coefficient as well.

However, it is strongly assumed that this picture of oxygen incorporation mechanisms is incomplete. For example, since oxygen and silane are highly reactive, even without plasma, many other precursors that contain oxygen, e.g. siloxanes or $SiO_2$, will form or never reach the plasma zone, respectively. Consequently, for oxygen the incorporation mechanisms are much more complicated as described above.

Nevertheless, if one assumes the application of the distribution coefficient model to oxygen incorporation valid, the LFLP, HFHP I, and HFHP II regimes can be compared and some trends are seen.

It is deduced from Figure 7.3 that the regular distribution coefficient $d_{reg}$ is up to 10 times lower for the HFHP II regime compared to that of the LFLP and HFHP I regimes. Even if the absolute value of $d_{reg}$ is rather difficult to determine, this ratio is clearly seen. This means that for the HFHP II regime the regular incorporation is much lower compared to that for the LFLP and HFHP I regimes.

Furthermore, the irregular impurity incorporation, proportional to the ratio of the irregularity factor $\beta$ and to the deposition rate $r_d$ is similar (with respect to uncertainties of the data fitting) for the three deposition regimes. Note, the irregularity factor for oxygen is about one order of magnitude higher compared to that for nitrogen. Thus, the oxygen incorporation is even more irregular compared to that of nitrogen. Here, one can assume that the solid phase doping efficiency is strongly influenced by the highly irregular oxygen incorporation. This might explain that the solid phase doping efficiency of nitrogen is one order of magnitude higher for nitrogen compared to that for oxygen (HFHP I regime). However, it has to be kept in mind that the oxygen distribution coefficient might be underestimated.

Nevertheless, the $\gamma$-factor that accounts for the significant alloying observed for oxygen incorporation also influences the doping efficiency. However, this happens at high oxygen concentrations that lead to poor solar cell performances that are not wished.

For oxygen, the solid phase doping efficiency is given by

$$\eta_{S,O} = \frac{c}{d_O \sqrt{X_{G,O}}} = c \cdot (d_{reg} \times X_{G,O}^{1/2} + \frac{\beta}{r_d} + \gamma \times X_{G,O}^{3/2})^{-1}. \qquad (7.2)$$

For a similar constant c for the three deposition regimes this would imply a high doping efficiency for the HFHP II regime compared to those found for the LFLP and HFHP I regimes (see d(O) in Figure 7.3). This is obviously not the case if the solar cell deterioration is caused by oxygen incorporated in doping configurations since experimentally for this assumption the doping efficiency of the HFHP II regime is found to be 10 times smaller compared to that for the LFLP and HFHP I regimes. In this case the ratio of regular active to non-active oxygen sites must be much higher for the LFLP and HFHP I regimes compared to that for the HFHP II regime. A further explanation might by the different quantities of oxygen reaching the plasma zone for different deposition regimes. If, as assumed in *chapter 5*, for the HFHP II regime the amount of oxygen reaching the plasma zone is lower, compared to that for the LFLP and HFHP I regimes, also the distribution coefficient for the HFHP II regime would be more underestimated compared to that for the other regimes. To understand this behaviour more work is needed.

**Gas phase doping efficiencies** In the foregoing section for the determination of the solid phase doping efficiency $\eta_{G,O} = c \cdot X_{G,O}^{-1/2}$ was assumed ($d_I = \eta_{G,I} / \eta_{S,I}$). For arsenic and phosphorus this was experimentally observed [Win1990] but for oxygen this assumption might not be valid. Thus, in this section it is assumed $c = 1$ and $\eta_{S,O}$ (LFLP & HFHP I) ~ 10 $\eta_{S,O}$ (HFHP II), as found experimentally, which is at least valid at the corresponding critical oxygen concentrations found for solar cells. Also, in this section, the amount of oxygen reaching the plasma zone is assumed to be similar for the three deposition regimes. An estimation of the gas phase doping efficiency $\eta_{G,O}$ can be made via $d(I) = \eta_G / \eta_S$, equivalent to $\eta_G = d_I \eta_S$. The distribution coefficients for the three regimes are $d_O$ ~ 60, 30, and 15 for the LFLP, HFHP I, and HFHP II regimes, respectively at $X_{G,O,crit}$ (LFLP & HFHP I), i.e. at the gas phase fraction at which $C_O$ ~ $2 \times 10^{19}$ cm$^{-3}$. These results show that the gas phase doping efficiencies of the LFLP and HFHP I regimes differ only by a factor of ~ 1/2 whereas $\eta_G$ is approximately 30 times smaller for the HFHP II regime compared to that for the LFLP and HFHP II regimes.

This result might be explained by different gas species entering the plasma zone: As discussed already in chapter 5 it is likely that due to the low oxygen incorporation probability found for the HFHP II regime there is a higher amount of siloxane entering the plasma zone compared to the precursors leading to oxygen incorporation in electronically active states. Thus, a more siloxane containing gas mixture is expected to enter the plasma zone. Of course, these different oxygen containing species may have different gas phase doping efficiencies. The gas phase doping efficiency of the siloxane-rich gas mixture must be much smaller than the gas

phase doping efficiency of the gas mixture of the LFLP and HFHP I regimes. Maybe between the LFLP and HFHP I regimes there are also slight differences in gas phase doping efficiency caused by different precursor species. This might explain the difference of a factor of two for their $\eta_C$'s at the critical gas phase fractions. However, these differences are very small and are not seen for solar cells or for material properties.

**Distribution coefficient as a function of the base pressure** In Figure 7.4 the distribution coefficient is shown as a function of the (oxygen) base pressure for the LFLP, HFHP I & II regimes. For low base pressures $d_O$ decreases with increasing base pressures followed by an increase with increasing base pressure above the critical base pressure that depends on the chosen deposition regime. Until now it is unclear whether this result is caused by coincidence or not. If not caused by coincidence, the range of the critical base pressure can be estimated for oxygen contamination from the inflection point of the distribution function.

## 7.6. Summary

The regular distribution coefficient is smaller for nitrogen compared to that of As and P, whereas nitrogen possesses a rather high irregularity factor $\beta$ compared to that of P. Thus, nitrogen incorporation is highly irregular, i.e. depends strongly on the gas phase fraction of nitrogen and on the deposition rate. However, the weak doping efficiency of nitrogen compared to that for phosphorus is not fully explained be the model of the distribution coefficient. If the model of $d_I$ is applicable to nitrogen, the formation of $NH_3$ as a precursor for irregular incorporation is assumed.

For oxygen it is questionable, whether the model of Winer et al. is applicable or not since oxygen and silane are highly reactive. Thus, the incorporation mechanism of oxygen is rather complex. However, if one compares the LFLP, HFHP I & II regimes it is seen that the ratio of regular active to non-active incorporated oxygen must be much lower for the HFHP II regime compared to that for the LFLP and HFHP I regimes or the amount of oxygen reaching the plasma zone must be different for the three deposition regimes. Otherwise the gas phase doping efficiency of the HFHP II regime must be much lower compared to the other regimes which might be explained by different oxygen precursors build due to different oxygen incorporation probabilities. Furthermore, it is suggested that the oxygen doping efficiency is much lower compared to that for nitrogen due to the very irregular incorporation of oxygen compared to that of nitrogen.

As a further result of this study the model of Winer et al [Win1990] is empirically extended to the case of alloying with oxygen impurities. This alloying factor most likely $> 0$ for nitrogen impurities at higher concentrations as well. The latter was not investigated in this study.

Finally, it is seen that there possibly is a strong correlation between the critical oxygen base pressure and the oxygen distribution coefficient. However, further investigations are necessary to confirm and explain this result.

# 8. Single-chamber process

In this chapter the recent developments of single-chamber processes for the deposition of a-Si:H solar cells are described. A single-chamber fabrication of a-Si:H solar cells in an inline 40 × 40 cm² deposition setup called "LADA" with an initial efficiency of $\eta_{ini}$ = 10.35 % is achieved. The highest a-Si:H module (40 × 40 cm²) efficiency obtained was $\eta_{ini}$ = 9 %.

To avoid boron cross-contamination, usually a big problem for single-chamber processes, reactor treatments before the i-layer deposition are found to be necessary. In this chapter the impact of different reactor treatments and device designs on the initial and stabilized cell efficiency is investigated. The reactor treatments are systematically studied in terms of their time consumption and boron cross-contamination reduction.

For the LADA system an in-situ "process chamber evacuation" worked very well in terms of cell efficiency and treatment time (~ 15 min). Here, after the deposition of the p-layer the chamber is evacuated to $9\times10^{-7}$ mbar prior to the deposition of the i-layer. However, for the small-area deposition system this treatment did not lead to the deposition of state-of-the-art solar cells which can be attributed to different substrate area to recipient wall area ratios for small and large deposition setups. For both setups an ex-situ $CO_2$-plasma treatment successfully reduced the boron cross contamination but this treatment was very time consuming (~ 30 min) and therefore industrially not preferable. For the small-area deposition setup also an in-situ $H_2O$-flush as a reactor treatment was applied. This treatment is difficult to control but can compete with the LADA recipient evacuation treatment in terms of time consumption (~ 15 min) and boron cross-contamination reduction. The influence of the device design did not have a significant influence on the boron cross-contamination for the device designs applied in this work.

## 8.1. Introduction

Single-chamber processes for thin-film a-Si:H solar cell production can be economically preferable [Kro2004]. All deposition steps for the deposition of hydrogenated silicon layers are subsequently carried out in a single deposition setup.

In mass production many of these single-chamber processes run in parallel and if in one chamber difficulties occur for the rest of the setup the deposition can be continued. For mass production of solar cells with a multi-chamber setup many i-layer deposition chambers are used combined with a few doping layer chambers. Thus, a failure of, e.g., the p-chamber would stop the cell production of many i-layer deposition chambers at the same time. Furthermore, no process time is lost for transportation of the substrate between the process chambers.

However, a major drawback of single-chamber processes is given by the cross-contamination of doping atoms used for the deposition of the p-layer and of the n-layer [Cab1989]. For example, boron from the chamber walls can be etched of by hydrogen during the deposition of the i-layer and then incorporated into the i-layer, i.e. boron recycling [Pla1997]. This contamination has to be avoided or at least reduced to a tolerable level in order to produce state-of-the-art solar cells. Therefore, reactor treatments are necessary before the deposition of the i-layer that have to be as short as possible due to the required high throughput of the deposition system. In-situ treatments in which the substrate can remain in the reactor are preferable. In the literature many different treatments are studied, see Table 8.1.

| reactor treatment | $\eta_{ini}$ [%] | ex-situ treatment | in-situ treatment | $C_{boron}$ [$cm^{-3}$] | reference |
|---|---|---|---|---|---|
| Ar-flush | 10.2 | | X | - | [Rep2004] |
| $CO_2$-plasma | 10.2 | X | | - | [Rep2004] |
| $NH_3$-flush | 9.8 | | X | ~ $10^{17}$ | [Bal2004a] |
| $H_2O$-flush | 10.1 | | X | ~ $10^{17}$ | [Kro2004] |
| $O_2$-plasma | - | X | | ~ $10^{17}$ | [Bal2002] |
| 12 h pumping | - | | X | ~ $10^{17}$ | [Bal2004b] |
| a-Si:H layer | - | X | | ~5 × $10^{17}$ | [Bal2004b] |
| 30 min pumping | 8.7 | | X | > $10^{18}$ | [Kro2004] |
| $H_2$ / Ar-plasma | - | X | | > $10^{18}$ | [Bal2002] |
| $H_2$ / Ar / $O_2$-flush | - | | X | > $10^{18}$ | [Bal2002] |
| no plasma-stop | 7.1 | | X | - | [Kro1999] |

*Table 8.1 Comparison of different reactor treatments before the deposition of the i-layer in a single-chamber process for the fabrication of a-Si:H solar cells.*

Up to now, the best single-chamber solar cell without special reactor treatment (application of only an Ar-purge and short evacuation of recipient) is carried out by Repmann et al. [Rep2004], who achieved $\eta_{ini}$ = 10.2 %. The same author showed that an ex-situ $CO_2$-plasma treatment also leads to $\eta_{ini}$ = 10.2 %. This confirms that no significant losses in initial cell efficiency are seen if no special reactor treatment is applied. However, in the studies of [Bal2002] & [Kro2004] the application of an Ar-flush and a 30 min reactor evacuation, respectively, led to a boron concentration $C_B > 10^{18}$ $cm^{-3}$ in the i-layer and to a reduced initial cell efficiency of $\eta_{ini}$ = 8.7 %. Thus, the reactor design or the deposition parameters might influence the effectivity/necessity of reactor treatments. Furthermore, they also showed that an

$H_2$-flush, an $O_2$-flush, and an a-Si:H cover layer (ex-situ treatment) all lead to a high boron cross-contamination into the i-layer. Thus, not surprisingly for the worst-case condition of no plasma-stop between p-layer and i-layer they obtained poor cell efficiencies of only $\eta_{ini} = 7.1$ % [Kro1999]. On the other hand, low boron cross-contaminations of $C_B \sim 10^{17}$ cm$^{-3}$ are obtained by Kroll et al. and Ballutaud et al. for the application of a very long reactor evacuation time (~ 12 h), the application of an ex-situ $O_2$-plasma, and by the use of an $H_2O$- or $NH_3$-flush (in-situ). These reactor treatments all lead to deposition of state-of-the-art solar cells. The assumed principle of operation for the different reactor treatments applied in this study are illustrated in *section 8.2.2*.

In this work a systematic survey on the different reactor treatments in different deposition setups is done. The intention is to study various treatments for their time consumption, their effectivity, and their influence on the stabilized solar cell performance. Economically, a fast procedure might be better than a longer treatment that yields slightly better solar cell efficiencies. Also, the question is addressed why no special treatment before the deposition of the i-layer leads to state-of-the-art solar cells for one deposition setup and for another one it does not. A further aspect that is investigated is the influence of the solar cell configuration, i.e. the insertion of additional layers between i-layer and p-layer, on the boron cross-contamination and on the stabilized solar cell performance. This impact of additional layers is introduced in *section 8.3.1*, where the solar cell configurations that are applied in this study are presented as well.

First, in this chapter, the development of a-Si:H solar cells grown in the 5K-multi-chamber deposition systems (*section 3.1.2*) with a single-chamber process is described. Second, the findings for the 10 × 10 cm$^2$ deposition system are transferred to the 40 × 40 cm$^2$ deposition system (LADA). For the LADA system (*section 3.1.3*) the recipient treatments are further optimized. Note, in this chapter, the LADA deposition system is referred to "large-area" deposition whereas the 5K-system is the "small-area" system.

## 8.2. Evaluation of reactor treatments (on a 10 × 10 cm$^2$ scale)

This section addresses different reactor treatments, in order to reduce the boron cross-contamination in the i-layer near the p/i-interface. In order to examine the impact of different reactor treatments on their boron reduction and on their time consumption, preliminary experiments are performed in the small-area 5K-multi-chamber PECVD deposition system. In order to simulate a single-chamber process, the p-layer and the i-layer are deposited subsequently in the p-chamber. Only the n-layer is deposited in the n-chamber. The influence of P cross-contamination is not considered in this study.

### 8.2.1. Process conditions for the i-layer

The parameters for deposition of the intrinsic a-Si:H layers in the p-chamber, are the following. Due to the fact that the p-chamber of the 5K-setup is only equipped with a laminar gas flow low total process gas flow is applied ($\Phi_{SiH4}/\Phi_{H2}$ of 24/24 sccm) in order to obtain homogeneous films. The deposition pressure is 1 Torr and the applied discharge power is 0.01 W/cm², yielding a deposition rate of ~ 0.2 nm/s. The substrate temperature is set to ~ 200 °C, i.e., similar to the temperature used for the deposition of the p-layer. In this regime the process gas flows and deposition pressures are even lower than for the LFLP regime discussed in *chapter 5*.

### 8.2.2. Reactor treatments

The aim of these experiments is to find a way to deposit state-of-the-art solar cells with an as short as possible delay between the deposition of the p-layer and i-layer and to transfer successful treatments to the LADA system. Note that generally, for safety reasons, a 5 min Ar-purge is necessary after each deposition if the transport lock of the deposition chamber or the valve to the water reservoir is opened. After Ar-purge three different reactor treatments are studied.

**Process chamber evacuation** For this treatment the reactor is only purged with Ar (5 min) and then evacuated to a specific base pressure (typically ~ $10^{-6}$ Torr). Also Ar-purging and evacuation cycles can be included into this treatment method. Finally, some minutes for the stabilization of the substrate temperature are necessary. Obviously, this is a fast method but it does not work in all deposition setups. This aspect is discussed later.

**$CO_2$-plasma** This method is considered as an ex-situ process, i.e., after an Ar-purge (safety reasons) the substrate is moved out of the p-chamber and a flow of $CO_2$ (36 sccm, i.e., the same flow rate that is used for the p-layer deposition) is applied. Subsequently, a plasma (power of 0.01 W/cm²) is ignited for a time period of a few seconds up to some tens of minutes (standard time ~ 5 min).

The $CO_2$-plasma is assumed to fix the boron in form of carbides and oxides at the chamber wall. An $O_2$-plasma is suggested to have a similar impact on the boron cross-contamination reduction. Of course, in this case only oxides are created that fix the boron at the internal surfaces [Bal2002]. Note, for both treatments the plasma power is necessary in order to induce the reaction between boron and $CO_2/O_2$.

After the plasma an a-Si:H cover layer can be deposited (deposition time of up to some minutes). Such a cover layer is found to reduce the boron concentration in the i-layer a little [Bal2002]. Next, an Ar-purge (5 min) is applied in order to remove the process gas from the reactor before the substrate can be returned into the reactor. The Ar-purges might not be necessary for industrial production but in the deposition chambers used in this study the aim was to prevent the diffusion of process gas

between different chambers of the rector and into the turbomolecular pump. Then, the chamber has to be evacuated for some minutes (standard time ~ 5 min). Finally, the process gas for the i-layer is introduced and the substrate temperature is stabilized within a time of typically ~ 5 min. This treatment is considered as a reference process.

**$H_2O$-vapor flush** This reactor treatment, first shown by [Kro2004], does not require moving the substrate out of the reactor (in-situ treatment). After the Ar-purge (safety reasons) a water-flush is applied for a time of 10 s to 10 min at a pressure of $8\times10^{-2}$ Torr from a water reservoir connected via full metal needle valve to the recipient. By this treatment the boron is assumed to be fixed at the chamber walls in form of oxides. After the water-vapor flush treatment the recipient is evacuated (standard time ~ 5 min) and a temperature stabilization time of some minutes is applied.

### 8.2.3. Effectivity of reactor treatments

In this study the reactor treatment time was systematically varied and the impact of these variations on the solar cell efficiency is studied. Figure 8.1 shows the treatment time between the deposition of the p-layer and the i-layer of the different treatments versus the cell efficiency. It is clearly seen that a process chamber evacuation does not prevent the cross contamination of boron into the i-layer. The low initial cell efficiencies in the range of 4.5 – 6 % result from losses in fill factor and short circuit current density and are attributed to boron cross-contamination. In contrast, state-of-the-art solar cells with the initial efficiencies reaching ~ 8.5 % can be deposited, applying a $CO_2$-plasma or an $H_2O$-vapor flush after the deposition of the p-layer. Note, the process in the p-chamber is optimized for the deposition of the p-layer and not for the deposition of the i-layer (e.g. with respect to the substrate temperature) and thus, the initial cell efficiencies are lower compared to those shown in *chapters 4 - 6*.

However, differences in time consumption are seen for optimized $H_2O$-vapor flush and $CO_2$-plasma treatments, respectively. Solar cells need either a $H_2O$- vapor flush with a minimum in treatment time of ~ 15 min or a $CO_2$-plasma treatment of at least ~ 25 min for an initial efficiency $\eta_{ini} > 8$ %. The $CO_2$-plasma or the $H_2O$- vapor flush on their parts take about 1 - 5 min. Important process steps that are also applied are the Ar-purges (safety reasons, see *section 8.2.2*), the chamber evacuation after the treatment (typically 5 min), and the substrate temperature stabilization (~ 5 min). For the $H_2O$-vapor flush it is observed that it is not easy to control the pressure during the water flush. In the worst case to much water enters the chamber and no further deposition is possible for the next hours.

In summary, the minimum treatment time is shortest for the process chamber evacuation and longest for a $CO_2$-plasma treatment. Disadvantage of the process chamber evacuation method is a low initial cell efficiency, disadvantage for the $CO_2$-plasma treatment is the high time consumption. In turn this treatment is very easy to

control. For the in-situ $H_2O$-vapor flush treatment the time consumption is acceptable but the process is difficult to control. However, the controllability probably is not a problem for industrial application and this reactor treatment is very promising.

For the LADA deposition system the reactor cleaning will be studied and discussed more detailed, especially the $CO_2$-plasma and recipient evacuation treatment, see *section 8.3*. In the LADA deposition system no water flush is installed yet.

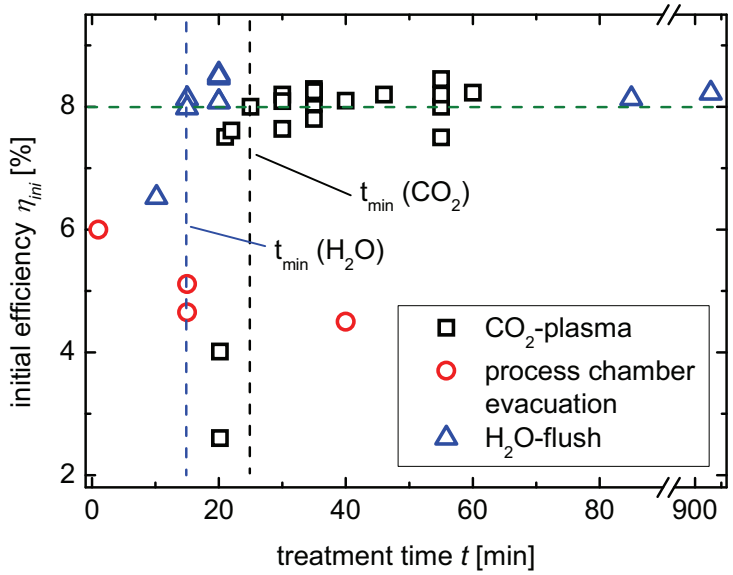


*Figure 8.1 Initial efficiency of a-Si:H solar cells as a function of the treatment time between the deposition of the p-layer and the i-layer for different reactor treatments. The dashed lines indicate the minimum required treatment times for the $H_2O$-flush (~ 15 min) and for the $CO_2$-plasma (~ 25 min).*

## 8.3. Single-chamber processes (on a 40 × 40 cm² scale)

In this section the realisation of a single-chamber process for the deposition of a-Si:H solar cells on a large scale (LADA) is described. Hereby, the impact of different solar cell configurations and reactor treatments before the i-layer deposition on the initial and stabilized cell performance is investigated. In summary a so-called p-$i_1$-$i_2$-n structure turned out to be favourable for the deposition of state-of-the-art solar cells. The $i_1$-layer is deposited under the same conditions as the $i_2$-layer (standard intrinsic layer), except for an increased hydrogen source gas flow. This leads to a slow deposition of high quality i-layer material. Subsequently the standard i-layer is deposited; between these two layers the plasma is not stopped. After the deposition of the p-layer a "process chamber evacuation" treatment was sufficient to reduce the boron cross-contamination to an acceptable level.

### 8.3.1. Interface configurations

In order to reduce the boron cross-contamination from the p-layer deposition into the i-layer, additional interface or buffer layers between the p- and i–layer might be of importance. Such layers can also lead to improved cell properties, such as an increased $V_{OC}$. However, the long term stability might suffer from additional layers. These findings are reported for solar cells that are deposited in a multi chamber system [Rec1997]. In the following, the different p/i-interface configurations used in this study are described.

**p-i-n configuration** In Figure 8.2 a schematic drawing of a simple p-i-n solar cell configuration is shown. The TMB-flow and *SC* used for the deposition of the specific part of the solar cell are indicated (see also Table 8.2).

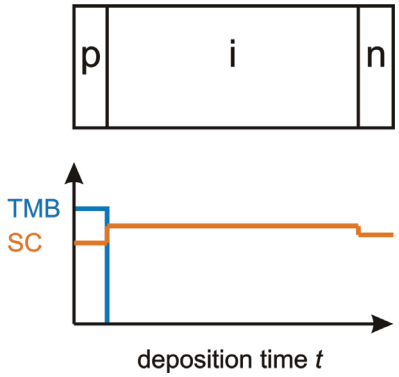


*Figure 8.2 p-i-n solar cell configuration and flow diagram.*

The *SC* for the p-, i-, and n-layer are 8.2, 10.8, and 9.2 %, respectively. These concentrations are changed abruptly between the subsequent layers. The TMB- and $CH_4$ flows (not shown) are constant during the deposition of the p-layer at $\Phi_{TMB} = 7.6$ sccm and $\Phi_{CH4} = 24$ sccm, respectively, and then they are switched of. Note, the source gases TMB and $PH_3$ are diluted in He and $SiH_4$, respectively. Their concentrations are 2.5 % of TMB and 5 % of $PH_3$, respectively. The $PH_3$-flow is not included into this schematic drawing, because for all cell configurations it is constant during the deposition of the a-Si:H n-layer at $\Phi_{PH3} = 15.5$ sccm. This configuration is used as a reference configuration.

| | $\Phi_{SiH4}$ [sccm] | $\Phi_{H2}$ [sccm] | $\Phi_{CH4}$ [sccm] | $\Phi_{TMB}$ [sccm] | $\Phi_{PH3}$ [sccm] |
|---|---|---|---|---|---|
| p-layer | 25.5 | 285 | 24 | 7.6 | - |
| i-layer | 41.4 | 339 | - | - | - |
| n-layer | 55.4 | 549 | - | - | 15.5 |

*Table 8.2 Applied process gas flow rates for the deposition of the p-i-n configuration*

**p-$i_1$-$i_2$-n configuration** Figure 8.3 shows the a-Si:H p-$i_1$-$i_2$-n structure. As a difference to the p-i-n structure, between p-layer and i-layer an additional i-layer is created by depositing the first part of the i-layer under different conditions. This i-layer is called $i_1$-layer and is deposited with a lower silane concentration of $SC \sim 3.9$ %. The lower $SC$ is achieved via an increase in $\Phi_{H2}$ (see also Table 8.3). Between the $i_1$- and $i_2$-layer the plasma is not stopped – only the gas composition is changed.

| | $\Phi_{SiH4}$ [sccm] | $\Phi_{H2}$ [sccm] | $\Phi_{CH4}$ [sccm] | $\Phi_{TMB}$ [sccm] | $\Phi_{PH3}$ [sccm] |
|---|---|---|---|---|---|
| p-layer | 25.5 | 285 | 24 | 7.6 | - |
| $i_1$-layer | 41.4 | 1030 | - | - | - |
| $i_2$-layer | 41.4 | 339 | - | - | - |
| n-layer | 55.4 | 549 | - | - | 15.5 |

*Table 8.3 Applied process gas flow rates for the deposition of the p-$i_1$-$i_2$-n configuration*

The $i_1$-layer leads to an improvement of the $V_{OC}$ that is explained by less recombination of charge carriers near the p/i-interface. Two explanations are given for this effect. First, the $i_1$-layer is deposited at a much lower deposition rate compared to that seen for the $i_2$-layer. This leads to deposition of very high quality material with a low defect density and less degradation upon light soaking [Hru2008]. Since a large fraction of the charge carriers are generated at this particular location there is less charge carrier recombination due to the high quality $i_1$-layer. Second, due to the high hydrogen dilution for the deposition of the $i_1$-layer this layer might have a slightly enhanced band gap compared to that for the $i_2$-layer. A high band gap material acts as a barrier for electrons moving in opposite direction with respect to the photocurrent. In both cases the equilibrium of photocurrent and recombination current is shifted to higher values for $V_{OC}$ [Sak1990], [Yos1988].

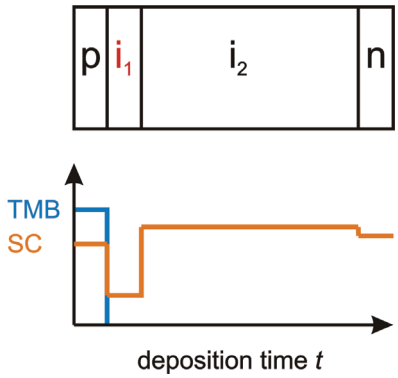


*Figure 8.3 p-$i_1$-$i_2$-n solar cell configuration and flow diagram.*

**p-b-$i_1$-$i_2$-n configuration** The third configuration studied is shown in Figure 8.4. Between the p-layer and the $i_1$-layer another layer is inserted. The so called buffer (b-)layer. Here, after the regular p-layer deposition of 50 s the deposition is continued. Only the TMB-flow is linearly decreased to zero over a time period of 10 s. Then, the deposition is continued, still without plasma-stop, without TMB for 15 s.

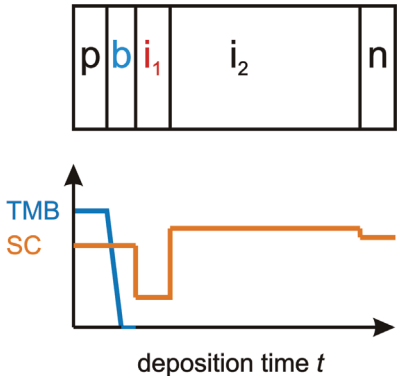


*Figure 8.4 p-b-$i_1$-$i_2$-n solar cell configuration and flow diagram.*

The idea is to additionally reduce the boron concentration in the i-layer by depositing a buffer-layer with a strongly reduced boron concentration compared to the p-layer (see also Table 8.4). Since the $i_1$-layer is deposited with a high hydrogen dilution the etching and, thus, boron recycling effect of the hydrogen is high. Thus, a buffer-layer with a reduced boron concentration may help to reduce the amount of boron etched by hydrogen and incorporated into the $i_1$-layer. Furthermore, in [Rec1997] it is seen that a very thin, slightly p-type doped buffer-layer between p-layer and $i_1$-layer can lead to an improved electrical field distribution in the solar cell, especially after light-induced degradation. Finally, the carbon in the buffer-layer increases its band gap. This increases the open-circuit voltage in the same way explained in the forgoing section.

However, in [Mun2004] it is shown that the insertion of such kind of buffer layers does not improve the long term solar cell performance. The initially increased cell efficiency due to an increased $V_{OC}$ is compensated by a stronger degradation upon light-soaking. This is assumed to be due to an increased number of charged defects in the a-SiC:H buffer-layer. It strengthens the internal field near the p/i-interface but decreases the field over the rest of the i-layer. In the initial state the impact of the weakened electrical field does not influence significantly the charge carrier collection but after light-soaking due to the increased number of recombination centres the electrical field is not strong enough anymore.

| | $\Phi_{SiH4}$ [sccm] | $\Phi_{H2}$ [sccm] | $\Phi_{CH4}$ [sccm] | $\Phi_{TMB}$ [sccm] | $\Phi_{PH3}$ [sccm] |
|---|---|---|---|---|---|
| p-layer | 25.5 | 285 | 24 | 7.6 | - |
| b-layer | 25.5 | 285 | 24 | 7.6 - 0 | - |
| $i_1$-layer | 41.4 | 1030 | - | - | - |
| $i_2$-layer | 41.4 | 339 | - | - | - |
| n-layer | 55.4 | 549 | - | - | 15.5 |

*Table 8.4 Applied process gas flow rates for the deposition of the p-b-$i_1$-$i_2$-n configuration.*

### 8.3.2. Boron cross contamination

In this section the impact of different reactor treatments are investigated by SIMS measurements in order to reduce the boron cross contamination. The influence of the different p/i-interface configurations cannot be determined by means of SIMS since the special resolution of the SIMS measurement is not high enough to resolve the boron contamination of the thin additional layers ($i_1$ and b). In this work three recipient treatments after the p-layer deposition were applied.

**Without plasma-stop (in-situ)** In this case the total treatment time is **0 min**. Between p-layer and i-layer the plasma is not switched of, only the process gas composition is changed. This would be an ideal process but it is to expect that the solar cells suffer strongly from boron cross-contamination.

**Process chamber evacuation (in-situ)** This treatment is an in-situ reactor treatment. After the p-layer deposition an argon purge of **5 min** is applied in order to prevent a contact between the turbomolecular pumps and the process gas. Then, the process chamber is evacuated and the temperature has to be stabilized again due to the different heat transfer by argon, vacuum, and process gas. **(~ 10 min** for $p_b = 9\times10^{-7}$ mbar and $T_S = 180 \pm 2$ °C). Thus, the treatment time in this case is 15 min and might be even shorter for a chamber evacuation to higher base pressures and for a more efficient temperature stabilization. This time might be reduced to ~ 1 - 3 min which would result in a total treatment time of ~ 6 – 8 min.

**$CO_2$-plasma (ex-situ)** After the p-layer deposition the process chamber (PC1) is purged with argon for **5 min**. Then, the substrate is moved out of the process chamber and a dummy carrier is transferred into the PC1-chamber. This consumes ~ **3 min**. Next, a $CO_2$-plasma of **~ 2 – 10 min** is applied in order to bind the boron that is at the chamber walls in form of carbides [Gra2005]. Then, a further argon purge of **5 min** and a substrate transfer back into the process chamber **~ 3 min** are necessary. Finally, some minutes are consumed by evacuating the reactor prior to the deposition of the i-layer and by substrate temperature stabilization **(~ 9 min** for $p_b = 9\times10^{-7}$ mbar and $T_S = 180 \pm 2$ °C). In sum, a total time consumption of ~ 27 – 35 min between the end of the p-layer plasma and the start of the i-layer plasma is

seen. Like for the reactor evacuation treatment also the time for the reactor evacuation and temperature stabilization may be reduced from 9 min to 1 – 3 min. However, this still would lead to a long minimal treatment time of ~ 19 - 21 min. This is the disadvantage of this reactor treatment. It is a very efficient [Kub1994], [Kub1995] in terms of a reduction of the boron cross-contamination but time consuming process. In this study, this reactor treatment served as a reference.

**Boron SIMS-profiles** In order to quantify the boron cross-contamination of the i-layer, SIMS measurements were performed. In Figure 8.5 the boron concentration profiles of a p-$i_1$-$i_2$-p-$i_1$-$i_2$ (a) and of a p-b-$i_1$-$i_2$-p-b-$i_1$-$i_2$ (b) multilayer structure are shown. For the p-$i_1$-$i_2$-p-$i_1$-$i_2$ (a) structure a $CO_2$-plasma, applied after the p-layer deposition, leads to a sharp decrease in boron concentration from $C_B > 10^{20}$ cm$^{-3}$ to $C_B = 2 – 4\times10^{16}$ cm$^{-3}$ in the i-layer. The process chamber evacuation to $9\times10^{-7}$ mbar leads to a less sharp decrease in boron concentration to $C_B = 1 – 3\times10^{17}$ cm$^{-3}$. For the p-b-$i_1$-$i_2$-p-b-$i_1$-$i_2$ (b) structure a $CO_2$-plasma and the process chamber evacuation lead to a sharp decrease to $C_B = 1 – 2\times10^{16}$ cm$^{-3}$ and to a less sharp decrease to $C_B = 0.8 – 1\times10^{17}$ cm$^{-3}$, respectively.

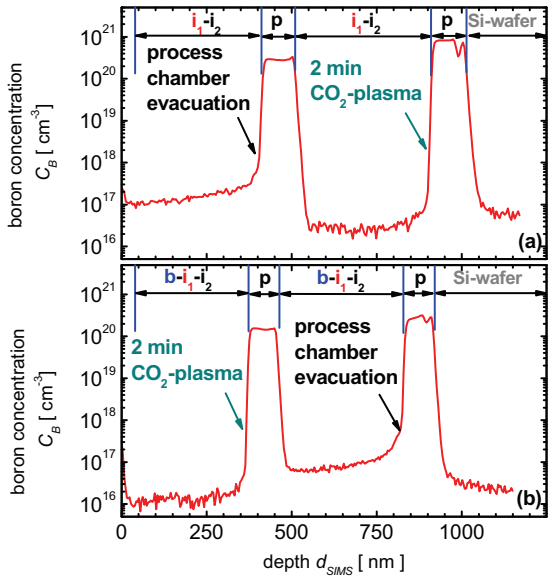


*Figure 8.5 SIMS depth profile of the boron concentration of a p-$i_1$-$i_2$-p-$i_1$-$i_2$ (a) and of a p-b-$i_1$-$i_2$-p-b-$i_1$-$i_2$ (b) sandwich structure deposited on a FZ-Si wafer. The treatment methods after the p-layer deposition are indicated.*

Here, one can conclude that the $CO_2$-plasma reactor treatment reduces the boron concentration to a more than one order of magnitude lower value than the process chamber evacuation. Furthermore, the insertion of a b-layer seems to improve slightly the suppression of boron incorporation, see Figure 8.5 (b). In the literature, values of boron concentrations of $3 – 5\times10^{17}$ cm$^{-3}$ [Kro2004] are found that do not

influence the device performance. Thus, the achieved results for the treatment of the reactor with the process chamber evacuation treatment seems to be very promising.

### 8.3.3. Solar cell characteristics

In this section the influence of the p/i-interface configuration of the solar cell and the rector treatment after the deposition of the p-layer is studied. It is found that a process chamber evacuation after the deposition of the p-layer leads to state-of-the-art solar cells.

**Impact of p/i-interface configuration** In Figure 8.6 (a) the IV-characteristics of a-Si:H solar cells deposited in the p-i-n, p-$i_1$-$i_2$-n, and p-b-$i_1$-$i_2$-n configuration deposited in the single-chamber process are shown. After the deposition of the p-layer or, for the p-b-$i_1$-$i_2$-n configuration, after the deposition of the p-b-layer stack a $CO_2$-plasma is applied in order to deposit reference cells in every configuration. Note, in contrast to *chapters 4-6* for these solar cells a ZnO/Ag back contact is used which increases the current output of the solar cells. The p-i-n configuration leads to high short-circuit current densities of $j_{SC}$ = 15.6 mA/cm² and low open-circuit voltages of $V_{OC}$ = 874 mV, see Table 8.5. The insertion of the $i_1$-layer increases the $V_{OC}$ to 898 mV and $j_{SC}$ remains at ~ 15.6 mA/cm². An additional buffer-layer further increases the $V_{OC}$ to 908 mV but decreases $j_{SC}$ to 15.4 mA/cm². This could be partly attributed to a thicker effective p-layer (+10 s deposition with decreasing TMB-flow). The fill factor of these solar cells is not significantly influenced by the p/i-interface configuration (*FF* ~ 73.5 %) and the initial cell efficiencies are 10.1, 10.3, and 10.3 % for the p-i-n, p-$i_1$-$i_2$-n, and p-b-$i_1$-$i_2$-n configuration, respectively.

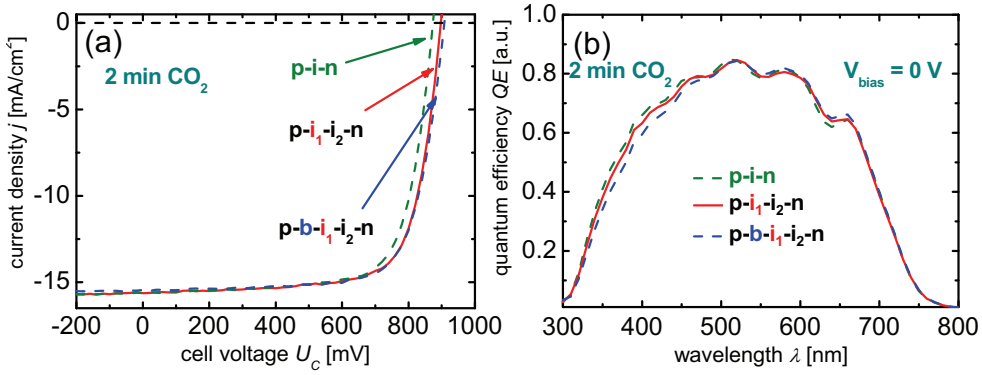


*Figure 8.6 Initial IV-characteristics (a) and quantum efficiency spectra at 0 V bias voltage (b) of solar cells deposited in the three indicated configurations in a single-chamber process. After the p-layer deposition an ex-situ $CO_2$-plasma treatment of 2 min is applied.*

Figure 8.6 (b) shows the quantum efficiency (*QE*) spectra of these configurations. It is seen that the insertion of the $i_1$-layer leads to slight losses in *QE* in the blue

wavelength region. If an additional buffer-layer is added, the losses in the blue wavelength region become more pronounced and also visible in $\Delta j_{SC} = 0.2$ mA/cm². In summary, compared to the p-i-n configuration, the last two configurations are very promising results which are further investigated in terms of reactor cleaning methods and long-term stability.

| | $\eta_{ini}$ [%] | *FF* [%] | $j_{SC}$ [mA/cm²] | $V_{OC}$ [mV] |
|---|---|---|---|---|
| p-i-n | 10.1 | 73.6 | 15.6 | 874 |
| p-$i_1$-$i_2$-n | 10.3 | 73.4 | 15.6 | 898 |
| p-b-$i_1$-$i_2$-n | 10.3 | 73.5 | 15.4 | 908 |

*Table 8.5 Solar cell parameters for different p/i-interface configurations. For all cells a $CO_2$-plasma reactor treatment was applied before the deposition of the i-layer.*

**Impact of reactor treatment** Figure 8.7 reveals the IV-characteristics together with the QE spectra of a-Si:H p-$i_1$-$i_2$-n solar cells deposited by a single-chamber process with application of different reactor treatments before the deposition of the i-layer. Note, for all cells the phosphorus cross-contamination from the n-layer deposition of the foregoing solar cell deposition is prevented by a $CO_2$-plasma treatment after the n-layer.

For the cell deposited without plasma-stop between all layers the $j_{sc}$ is reduced to 12.5 mA/cm² which is also observed for QE-measurements. Especially, in the blue wavelength region the decrease in *QE* is significant indicating a bad p/i-interface. Therefore, no reactor cleaning leads to reduced $\eta_{ini} = 7.57$ % and $FF = 66.7$ %, respectively. For deposition of state-of-the-art solar cells a $CO_2$-plasma treatment or evacuating the reactor is necessary. The difference in solar cell performance between $CO_2$-plasma treatment or process chamber evacuation is negligible, see Table 8.6. Neither the $j_{SC}$, nor the $V_{OC}$ are significantly different for these two reactor treatments. Also the *FF* does not change. This leads to relatively similar initial cell efficiencies of 10.2 and 10.3 % for the process chamber evacuation and for the $CO_2$-plasma method, respectively.

| | $\eta_{ini}$ [%] | *FF* [%] | $j_{sc}$ [mA/cm²] | $V_{OC}$ [mV] |
|---|---|---|---|---|
| $CO_2$-plasma | 10.3 | 73.4 | 15.6 | 898 |
| process chamber evacuation | 10.2 | 74.0 | 15.5 | 895 |
| process chamber evacuation, without plasma-stop between i & n | 10.4 | 73.5 | 15.6 | 900 |
| without plasma-stop | 7.6 | 66.7 | 12.5 | 906 |

*Table 8.6 Solar cell parameters for different reactor treatments. For all cells a p-$i_1$-$i_2$-n configuration was applied.*

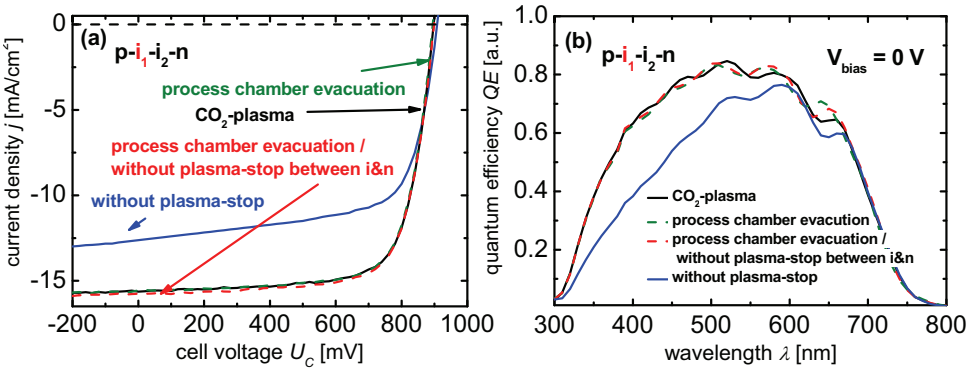


*Figure 8.7 Initial IV-characteristics (a) and quantum efficiency spectra at 0 V (b) of solar cells deposited in the p-i$_1$-i$_2$-n configuration. The various treatments after the p-layer deposition are indicated. Additionally, measurements of a cell deposited without plasma stop only between the i- and n-layer is shown.*

Also the QE-spectra of the solar cells deposited by using these two types of treatments do not differ significantly. Note, generally between i- and n-layer a plasma stop and chamber evacuation is performed. However, in Figure 8.7 also a solar cell is shown, where between p- and i-layer a process chamber evacuation and between i- and n-layer no plasma-stop was done in order to save cell deposition time. This cell is, up to know, the best a-Si:H solar cell deposited by a single-chamber process in the LADA system. Compared to the cell with process chamber evacuation between p- and i-layer and with plasma-stop between i- and n-layer the initial cell efficiency is increased by 0.1 % due to slightly higher $V_{OC}$ and $j_{SC}$ values (at the same total cell thickness).

**Bias voltage dependent QE-measurements – Impact of interface configuration**

A detailed investigation of the p/i-interface for all configurations and treatments is done via bias voltage dependent QE-measurements. If the p/i-interface is weak, an applied bias voltage leads to visible changes in *QE* in the short wavelength region, i.e. in $j_{SC}$. A positive bias voltage weakens the build in electrical field of the solar cell. The charge carrier extraction probability decreases for bad p/i-interfaces. In turn, weak interfaces can be compensated by a negative applied bias voltage [Gra2005].

Figure 5.4 shows the voltage dependent QE-measurements for different cell configurations. For all solar cells after the p-layer a $CO_2$-plasma treatment is performed. The p-i-n configuration with a 2 min $CO_2$-plasma is shown in Figure 5.4 (a). The difference $\Delta j_{SC}$ = 0.75 mA/cm² for a bias voltage range from -0.5 V to +0.5 V is slightly larger than the $\Delta j_{SC}$ of 0.5, 0.4, and 0.48 mA/cm² observed for the p-i$_1$-i$_2$-n (b), p-b-i$_1$-i$_2$-n (c), and p-b-i$_1$-i$_2$-n (d) configurations, respectively. Note, in (d) the $CO_2$-plasma treatment time is extended from 2 to 10 min which has a negative influence on the total short-circuit current density. It can be stated that for all configurations the p/i-interface is of a good quality since the quantum efficiencies do not chance significantly upon different bias voltages.

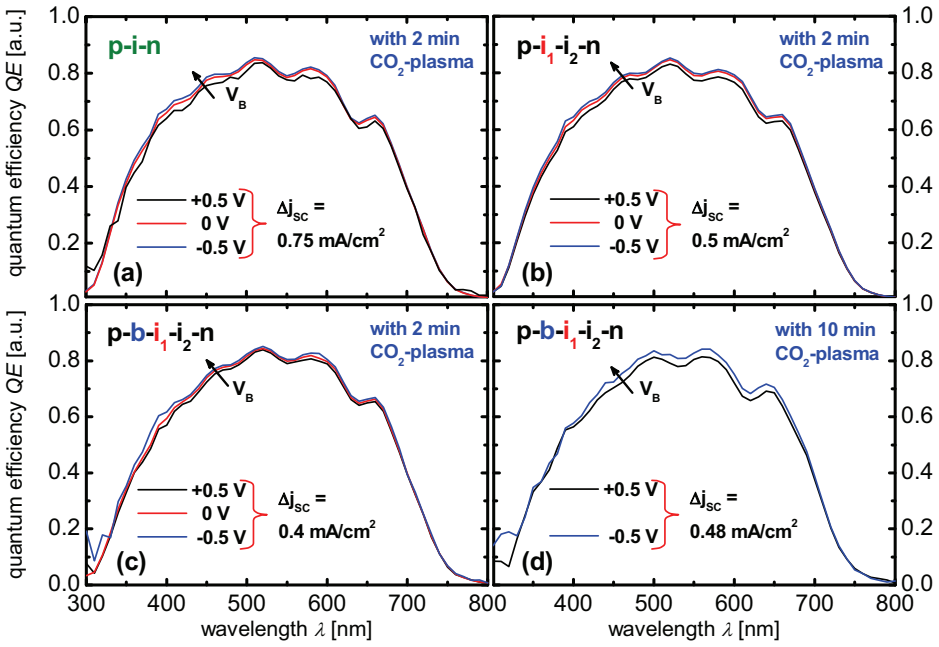


*Figure 8.8 Bias-voltage dependent quantum efficiency as a function of the wavelength. The QE of different solar cell configurations (+$CO_2$-plasma treatment) are compared (see indications in the graph). As an indication for the solar cell quality the variation in $j_{SC}$ between -0.5 V and 0.5 V is indicated.*

**Bias voltage dependent QE-measurements – Impact of reactor treatment** Figure 8.9 shows the bias voltage dependent QE-spectra of a-Si:H p-$i_1$-$i_2$-n solar cells deposited in with a single-chamber process using different reactor treatments. For the p-$i_1$-$i_2$-n configuration a process chamber evacuation after the p-layer deposition leads to $\Delta j_{SC} = 0.59$ mA/cm² (a) which is only 0.09 mA/cm² more compared to the $CO_2$-plasma treatment (Figure 8.9 (b)). This difference is very small and, thus, the process chamber evacuation treatment after the p-layer deposition is appropriate for the deposition of state-of-the-art solar cells.

The cell performance for the p-$i_1$-$i_2$-n configuration and process chamber evacuation is even slightly better if no plasma stop between i- and n-layer is applied (c). This leads to a $\Delta j_{SC}$ of 0.46 mA/cm². In turn, no plasma stop between p-layer and i-layer significantly decreases the p/i-interface quality (p-$i_1$-$i_2$-n configuration shown (d) but similar for other configurations). This is indicated by the high $\Delta j_{SC}$ of 2.23 mA/cm² and, thus, by the low initial cell efficiency of only $\eta_{ini} = 7.57$ %. In conclusion, the recipient evacuation after the p-layer deposition is a necessary step whereas a $CO_2$-plasma treatment is not required. This is a result which is in contrast to the findings for the small-area (5K) deposition setup and this point is discussed later.

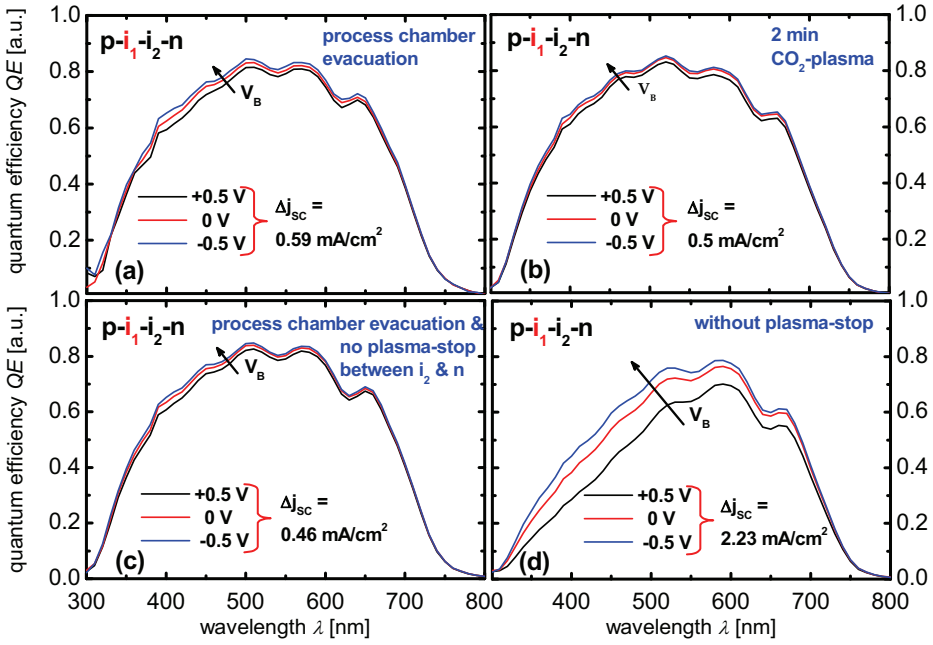


*Figure 8.9 Bias-voltage dependent quantum efficiency as a function of the wavelength. The QE of different treatment methods are compared for the p-i₁-i₂-n configuration (see indications in the graph). As an indication for the solar cell quality the variation in $j_{SC}$ between -0.5 V and 0.5 V is indicated.*

**Treatment time vs. initial cell efficiency for different treatments** An overview of the time consumption of the different recipient treatments is shown in Figure 8.10 as a function of the resulting initial solar cell efficiency. This time indicates the time between the plasma stop after the deposition of the p-layer (or after p-layer and buffer-layer if applied) and the plasma ignition before the deposition of the i-layer plus the time between the plasma stop after the deposition of the i-layer and the plasma ignition before the deposition of the n-layer. Applied solar cell configurations are the p-i₁-i₂-n and the p-b-i₁-i₂-n configuration since these show the highest initial cell efficiencies.

Without plasma stop, of course, no time is consumed but also the initial cell efficiency stays below $\eta_{ini} = 8$ %. The process chamber evacuation as an in-situ reactor treatment needs at least 5 min (Ar-purge between p- and i-layer) if no treatment is done between i- and n-layer. Here, state-of-the-art solar cells with $\eta_{ini} > 10$ % are produced with a total treatment time of 15 min (+ 6 min if a plasma-stop between i- and n-layer is applied). A $CO_2$-plasma requires two times the Ar-purge and transportation time (ex-situ treatment). Thus, a time of 16 min is the minimal time needed. In this work the minimal times leading to state-of-the-art solar cells were in the range of ~ 27 + 6 min. This time surely can be reduced to 27 min if no plasma stop is applied between i-layer and n-layer, since this plasma stop found to be not

necessary. In summary, for the deposition of high quality solar cells it is seen that the reactor evacuation treatment and the $CO_2$-plasma treatment require treatment times of 15 min and 27 min, respectively. The reduction potential of these treatment times will be discussed later.

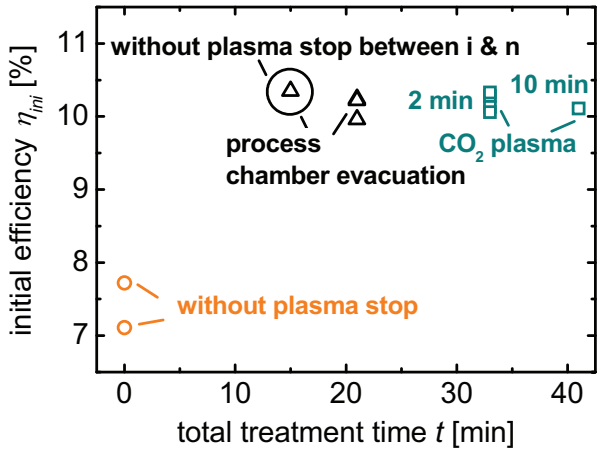


*Figure 8.10 Initial efficiency of a-Si:H solar cells as a function of the total treatment time for different reactor treatments. The time between the deposition of the i-layer and the n-layer is included as well*

**40 × 40 cm² solar modules** In the foregoing sections it turned out that the p-$i_1$-$i_2$-n configuration and the process chamber evacuation treatment show a slight boron cross contamination into the i-layer but the boron concentration is low enough to deposit state-of-the-art solar cells. A successful transfer from a-Si:H solar cells deposited on 10 × 10 cm² TCO coated glass by using a single-chamber process is achieved. This led to the first 40 × 40 cm² solar module, deposited in a single-chamber process using the process chamber evacuation as a reactor treatment after the deposition of the p-layer. Figure 8.11 shows the IV-characteristics of this module. The initial module efficiency is $\eta_{ini}$ = 9 % (aperture area) and the fill factor is $FF$ = 70 %. The whole module consists of 72 cell stripes of 0.5 × 36 cm² aperture area that are connected in series. This leads to $V_{OC}$ = 65 V and $I_{SC}$ = 255 mA (corresponds to $j_{SC}$ = 14.2 mA/cm²). A corresponding 1 × 1 cm² solar cell would have a $V_{OC}$ of 905 mV. Thus, the module has slight losses in $j_{SC}$ and $FF$ compared to single solar cells ($FF$ = 73.5 % and $j_{SC}$ = 15.6 mA/cm²). For comparison, the best 10 × 10 cm² module produced with a multi-chamber process at the IEF-5 so far had an initial efficiency of $\eta_{ini}$ = 9.5 % (2006). The loss mechanisms for the module efficiency compared to that for the cell efficiency are discussed later.

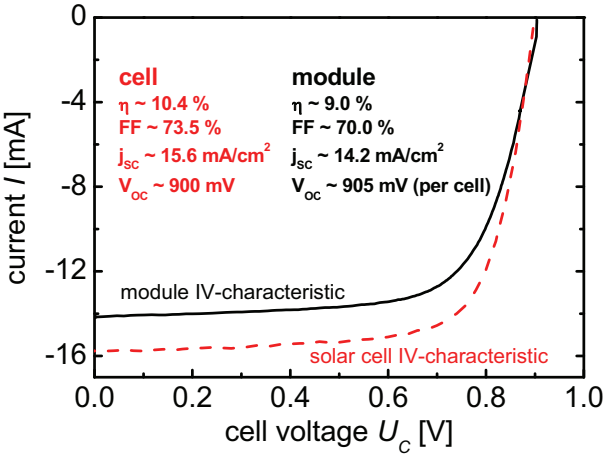


*Figure 8.11 Initial IV-characteristic of the first a-Si:H solar cell module deposited by a single-chamber process on a 40 × 40 cm² Asahi U substrate. The cell is deposited in the p-i₁-i₂-n configuration with only pumping after the p-layer. The module has a high efficiency of 9 %. For comparison, the corresponding properties of a solar cell are shown as well.*

### 8.3.4. Light-induced degradation of solar cells

In this section the long-term stability of the a-Si:H solar cells deposited in different cell configurations and with different recipient treatments are presented. In Figure 8.12 the initial and stabilized solar cell efficiencies after 1000 h of light-soaking are compared for the different solar cell configurations and reactor treatments. In the initial state, solar cells deposited in the p-i₁-i₂-n and in the p-b-i₁-i₂-n configuration showed the best results, namely cell efficiencies of $\eta_{ini}$ ~ 10.3 % compared to $\eta_{ini}$ ~ 10.1 % for the p-i-n configuration. For these cells the $CO_2$-plasma reactor treatment was applied after the deposition of the p-layer. In the degraded state the p-i₁-i₂-n configuration led to cell efficiencies of $\eta_{stab}$ ~ 7.7 - 7.9 %, for the p-b-i₁-i₂-n configuration the stabilized efficiency is $\eta_{stab}$ = 7.4 %. The p-i-n configuration, initially showing an efficiency of $\eta_{ini}$ = 10.1 %, had a stabilized efficiency of $\eta_{stab}$ = 7.6 %, i.e. the relative degradation was lower compared to the other configurations. For all cell configurations the losses upon light-soaking are mainly caused by a decrease in fill factor.

In Figure 8.12 (b) the impact of the reactor treatment on the initial and stabilized efficiencies of p-i₁-i₂-n solar cells is shown. Initially, the $CO_2$-plasma (33 min total treatment time) and process chamber evacuation treatment (21 min) show efficiencies of 10.3 – 10.4 %, irrespective of the applied reactor treatment. Also, a plasma stop between the i-layer and the n-layer (time consumption of ~ 6 min) is not of importance for high-quality solar cells. In turn, between the p-layer and the n-layer this stop is necessary, otherwise initial cell efficiencies below 8 % are the result. For the degraded state these relations do not change. Stable efficiencies in the range of 7.6 – 7.9 % are seen, except for the no plasma-stop before the i-layer method.

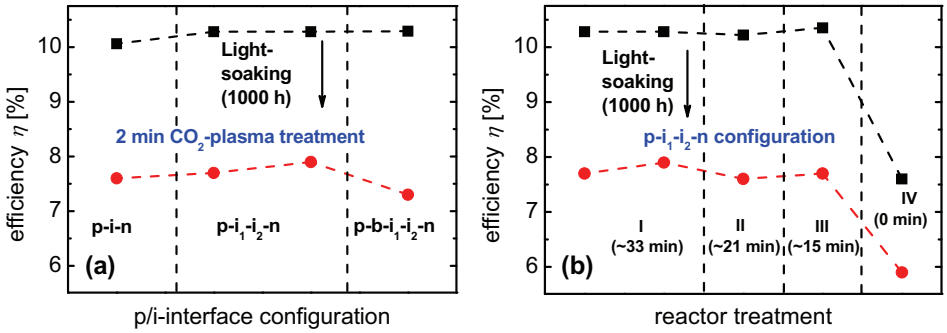


*Figure 8.12 Initial (black squares) and after 1000 h of light-soaking (red circles) efficiencies of solar cells deposited in a single-chamber process. The different configurations (a) and reactor treatments (b) are indicated. Treatments I, II, III, IV are $CO_2$-plasma, process chamber evacuation, process chamber evacuation without plasma-stop between i- and n-layer, and without plasma-stop, respectively.*

## 8.4. Discussion

In the foregoing sections it is shown that state-of-the-art a-Si:H solar cells with a single-chamber process were achieved. The p-$i_1$-$i_2$-n solar cell configuration turned out to have the best initial and stabilized efficiencies compared to the other cell configurations. For this configuration the first 205 s of the i-layer are deposited with a much lower silane concentration compared to that for the rest of the i-layer. As a reactor treatment after the deposition of the p-layer for the LADA deposition system a process chamber evacuation strategy worked very well in terms of cell efficiency and treatment time. Here, after the deposition of the p-layer the chamber is evacuated to $9\times10^{-7}$ mbar prior to the deposition of the i-layer. This process developed for solar cells was successfully applied to the deposition of modules and a module with an initial efficiency of $\eta_{ini} = 9$ % (aperture area) was deposited in a single-chamber process. In the following these results are discussed.

### 8.4.1. Solar cell configuration

For solar cells deposited in a multi chamber deposition setup the impact of layers between the p-layer and the i-layer is controversy discussed in literature [Ary1986], [Xi1994]. A high gap buffer-layer increases the $V_{OC}$ because the buffer-layer acts as a barrier for electrons moving in forward direction. The recombination of charge carriers and, thus, the recombination current is reduced and a higher voltage is necessary to balance photo- and recombination-currents [Sak1990], [Yos1988]. Often, a reduced stabilized efficiency of solar cell with additional layers is reported [Rec1997]. If the additional layer has a higher defect density, e.g., a-SiC:H buffer layers, the defects are positively charged because the Fermi-level near the p/i-interface is near the valence band. This leads to a reduction of the internal electrical field over the solar cell. In the initial state the defect density in the i-layer is

low enough that the weakened electrical field has no significant impact on the solar cell performance. If the number of defects in the i-layer is increased by light-soaking the reduced field over the i-layer (due to the buffer-layer) might be too small for sufficient charge carrier extraction.

The other additional layer investigated in this study is the $i_1$-layer where for the first 205 s of the i-layer the silane concentration is strongly reduced. This is assumed to improve the film quality due to a rather slow deposition rate. This would increase the $V_{OC}$ because also in this case the charge carrier recombination in the vicinity of the p/i-interface is reduced due to a reduced defect density, i.e. reduced number of recombination centers. An advantage compared to the buffer-layer is the unaffected electrical field. A disadvantage is the lower gain in $V_{OC}$ for the $i_1$-layer compared to that for the buffer-layer.

It is seen that, initially, the p-$i_1$-$i_2$-n configuration and the p-b-$i_1$-$i_2$-n configuration lead to the highest initial efficiencies of $\eta_{ini} \sim 10.3$ %, compared to the initial efficiencies of $\eta_{ini} \sim 10.1$ % obtained for a simple p-i-n configuration. The increase is mainly caused by an increase in initial $V_{OC}$, as also seen in literature for multi-chamber solar cells. After light-induced degradation the p-$i_1$-$i_2$-n configuration shows the highest stabilized efficiencies of $\eta_{stab} \sim 7.7 – 7\text{-}9$ % compared to the other configurations (p-b-$i_1$-$i_2$-n $\eta_{stab} = 7.4$ %, p-i-n $\eta_{stab} = 7.6$ %). Irrespective of the solar cell configuration the degradation is mainly caused be losses in fill factor upon light soaking. The losses in $V_{OC}$ and $j_{SC}$ are similar for the investigated solar cells. In this work related to development of single-chamber processes for the deposition of a-Si:H, the $i_1$-layer improves the initial as well as the stabilized efficiencies.

For the $i_1$-layer intrinsic a-Si:H deposited at a low deposition rate of ~ 0.1 nm/s was chosen as a material in order to keep the defect density at a low level compared to the rest of the i-layer. Since the electrical field over the i-layer is not affected by $i_1$-layer the stabilized values are, as expected, the best for this configuration. A further positive effect of the $i_1$-layer might be an increase of the band gap due to the high hydrogen dilution compared to the rest of the i-layer. This effect might also increase the $V_{OC}$ without negative effects on the cell stability.

The impact of the buffer-layer on the stabilized efficiency is negative. This layer with a reduced boron concentration was thought to prevent the etching and recycling of boron from the p-layer during the deposition of the highly hydrogen diluted $i_1$-layer. Indeed, the SIMS profiles show that the in-diffusion of boron is slightly reduced by the insertion of a buffer-layer. However, it is assumed that this layer also leads to a high amount of charged defects decreasing the electrical field over the solar cell. This would be is in a good correlation with the high degradation losses observed for light-induced degradation.

### 8.4.2. Reactor treatment

It is found that there is no unique “best” treatment a given deposition setup. For example, for the LADA deposition setup an evacuation of the process chamber after the deposition of the p-layer is sufficient for the deposition of state-of-the-art solar

cells. In contrast, this reactor treatment does not work sufficiently for the smaller 5K-deposition setup. Here, a water-flush was the best and fastest treatment. Furthermore, in this study the effectiveness of a reactor treatment does not depend on the solar cell configuration. In the following the applied reactor treatment will be discussed. An overview of the applied treatment times and their impact on the solar cell quality is given in Table 8.7.

| | treatment time small-area | State-of-the-art cell quality | treatment time large-area | State-of-the-art cell quality |
|---|---|---|---|---|
| $CO_2$-plasma | 25 min | ✓ | 27 min | ✓ |
| process chamber evacuation | 15 min | × | 15 min | ✓ |
| $H_2O$-flush | 15 min | ✓ | - | - |
| without plasma-stop | - | - | 0 min | × |

*Table 8.7 Treatment times for different reactor treatments and different deposition systems and their impact on the solar cell quality.*

**$CO_2$-plasma** This kind of reactor treatment leads to state-of-the-art solar cells for both deposition setups. Thus, this treatment is not deposition system dependent which is a great advantage of this procedure. The disadvantage of this process is the extremely long treatment time of nearly 30 min. Most of the time is needed for transport and Ar-purging process steps since this treatment is an ex-situ treatment, i.e. not a "real" single-chamber process. Only 2 min the $CO_2$-plasma treatment is applied. The carbon of the $CO_2$ is assumed to bind the boron in form of carbides or oxides [Gra2005], [Bal2002] at the surfaces of the reactor and of the electrode and to prevent the incorporation of the boron into the i-layer. The strong reduction of the boron concentration is observed by SIMS. A $CO_2$-plasma leads to a boron concentration in the i-layer of ~ $2\times10^{16}$ $cm^{-3}$ compared to ~ 1 - $2\times10^{17}$ $cm^{-3}$ for the process chamber evacuation.

**Process chamber evacuation** This reactor treatment represents an in-situ reactor treatment which time consumption can be reduced to some minutes for industrial processes. However, this treatment is strongly deposition system dependent. Possible reasons might be the different chamber sizes, pumping geometries, and material deposited on the recipient surfaces. In the LADA system the chamber is directly pumped at the plasma-area. This probably leads to a better removal of the boron from the plasma area. Furthermore, the LADA system has a lower ratio of substrate-area to surrounding walls area compared to that for the 5K-depoition system. Thus, the boron recycling effect is assumed to be lower for the LADA setup. The last point, material deposited on the recipient walls, has to be further investigated. In this work the deposition history of the LADA system was not very long since this setup was installed in 2009 in contrast to the 5K-deposition system

running since years. This point might be of interest for the LADA system in the future.

**Without plasma-stop** Up to now, "no treatment" is equivalent to "no solution" for the deposition of state-of-the-art solar cells. The boron that is still present in the recipient after the deposition of the p-layer, at the chamber walls as well as in the gas phase. Thus, it is not surprising that it is incorporated into the i-layer. This leads to a strong reduction of the solar cell efficiency by the incorporated boron. The boron is assumed to weaken the electrical field that expands over the i-layer and thus, reduces the charge carrier collection.

**$H_2O$-vapour flush** By this treatment, the boron is bonded at the surface or pumped out in form of stable boron oxides [Kro2004]. The advantage of this treatment is the low treatment time; the disadvantage is its controllability. If too much water-vapor enters the recipient a long evacuation time is necessary to pump out the water. Otherwise, the negative influence of oxygen incorporation leads to cell deterioration, see *chapters 4-6*. However, the controllability should not be a big problem for industrial application.

### 8.4.3. Solar modules

A successful deposition of a solar module with a size of 40 x 40 $cm^2$ and with $\eta_{ini}$ = 9 % (aperture area) was achieved. For comparison, a solar cell deposited with the same process conditions (p-$i_1$-$i_2$-n configuration, process chamber evacuation after the p-layer). Leads to initial cell efficiencies of $\eta_{ini}$ = 10.4 %. Loss mechanisms upon up-scaling procedures from solar cells to solar modules are known [Ben1999] and possible reasons for losses in efficiency in this case are given in the following. Due to the sheet resistance of the TCO there are losses in terms of Joule heat. Furthermore, due to film inhomogeneities there are further decreases of the module efficiency compared to that of the solar cell. Theses inhomogeneities, e.g., in film thickness can result from non-uniform plasma potential distributions or non-uniform source gas distributions. Losses due to the area that is lost for the energy conversion due to the area needed for, e.g., cell interconnection is not considered by the aperture area efficiency. Via these mechanisms it is seen experimentally that the initial module efficiency is ~ 14 % smaller compared to that for the solar cell.

## 8.5. Summary

A single-chamber fabrication of a-Si:H solar cells in an inline 40 × 40 $cm^2$ deposition setup called "LADA" with an initial efficiency of $\eta_{ini}$ = 10.35 % is achieved. The highest initial a-Si:H module (40 × 40 $cm^2$) efficiency found was $\eta_{ini}$ = 9 %.

To avoid boron cross-contamination reactor treatments after the p-layer deposition are found to be necessary. For the LADA system an in-situ "process chamber evacuation" worked very well in terms of cell efficiency and treatment time.

However, for the small-area deposition system this treatment did not lead to the deposition of state-of-the-art solar cells which might be due to the different substrate area to recipient wall area ratios for small and larger deposition setups. For both setups an ex-situ $CO_2$-plasma treatment successfully reduced the boron cross contamination but this treatment was very time consuming. For the small-area deposition setup also an $H_2O$-flush as a reactor treatment was applied. This treatment is difficult to control but can compete with the LADA recipient evacuation treatment in terms of time consumption and boron cross-contamination reduction.

# 9. Conclusion & outlook

In the present work the impact of contamination on the performance of solar cells was investigated. On the one hand contamination can be caused by atmospheric gas like oxygen and nitrogen, e.g., via air-leaks in the deposition setup. On the other hand for single-chamber processes the cross-contamination of doping atoms (boron and phosphorus) into the i-layer of the solar cell can lead to significant cell performance deterioration. An overview of the deposition parameters used and results obtained in the study of atmospheric contamination of solar cells is given in the *appendix* (see Table 11.1 & Table 11.2)

## 9.1. Atmospheric contamination of a-Si:H

The aim of this thesis was to understand the impact of atmospheric contamination on thin-film silicon solar cells. Therefore solar cells and single intrinsic layers (i-layers) were deposited with intentional air, oxygen and nitrogen leaks during the deposition of the i-layer. The applied leaks where either situated at the chamber wall or at the process gas pipeline, representing bad vacuum conditions (leaks, outgassing, weak vacuum pumps) or contaminated process gases (leaks, impure gas), respectively. Also, the influence of source gas flow and deposition rate on the impurity incorporation was studied. Finally, light-soaking experiments were performed.

### 9.1.1. General effect of impurities in a-Si:H solar cells

First, the general impact of oxygen and nitrogen on the performance of a-Si:H solar cells is studied for the so called HFHP I deposition regime. For details concerning the deposition regimes, see *chapters 4 - 6*. In order to intentionally incorporate oxygen or nitrogen an oxygen, nitrogen, or air leak is simulated by means of a controllable leak at the wall of the recipient.

It is seen that a part of the incorporated oxygen and nitrogen is found to be a n-type donor that shifts the Fermi-level towards the conduction band. This finding is supported by the electrical properties of single i-layers. The donors reduce the electrical field over the i-layer of the solar cell and reduce the performance of solar

cells if a critical impurity concentration is exceeded. For an oxygen leak a critical oxygen concentration of $C_{O,crit} = 2\times10^{19}$ cm$^{-3}$ in the i-layer is found applying the HFHP I regime; for nitrogen the critical concentration is $C_{N,crit} = 4\times10^{18}$ cm$^{-3}$. The critical concentrations do not change upon light soaking.

From the critical impurity concentration it is assumed that the doping efficiency of oxygen is approximately 10 times smaller compared to that of nitrogen. Note, based on conductivity measurements only 0.5 ‰ of the $2\times10^{19}$ oxygen-atoms/cm$^3$ are assumed to be in an electronically active configuration. However, the critical oxygen and nitrogen base pressures (proportional to the critical impurity gas flows) are rather similar, namely $7\times10^{-6}$ Torr and $1\times10^{-5}$ Torr, respectively (values to be found back in Table 4.1). This is explained by a 10 times higher oxygen incorporation probability compared to that for nitrogen. The effect of doping efficiency and impurity incorporation probability compensate each other and lead to the similar critical base pressure observed for oxygen and nitrogen incorporation. Consequently, the critical base pressure for an air-leak is also in the same range, namely $8\times10^{-6}$ Torr.

However, from the solar cell performance as a function of the oxygen and nitrogen concentration for air-leak contaminated cells it is seen, that oxygen is the main cell destructive contaminant, i.e. the critical oxygen concentration is reached first for air-leak contamination. This is surprising since the ratio of oxygen to nitrogen in air is ~ 1/4. Thus, from the oxygen and nitrogen contamination experiments a ratio of 10/4 of incorporated oxygen to incorporated nitrogen would have been expected since the oxygen incorporation probability is 10 times higher compared to that for nitrogen. Now, assuming a 10 times higher doping efficiency for nitrogen compared to that for oxygen, one would guess nitrogen to be the main cell destructive contaminant. An explanation can be the preferred incorporation of oxygen in the presence of both species.

For non-homogeneously contaminated cells, close to the i/n-interface a concentration higher than the critical impurity concentration $C_{I,\,crit}$ can be tolerated in the i-layer. Close to the p/i-interface the critical impurity concentrations in the i-layer are similar to the above mentioned values.

### 9.1.2. Impact of source gas flow & deposition rate on impurity incorporation

This section concludes the impact of source gas flow and deposition rate on the incorporation of oxygen and on the corresponding initial and light-soaked solar cell performance. The effect of total process gas flow (from ~ 110 sccm to ~ 1015 sccm) and deposition rate (from ~ 0.15 nm/s to ~ 0.5 nm/s) on the oxygen incorporation has been systematically studied. Here, three deposition regimes were applied.

For total flow rates of ~ 112 sccm (LFLP regime) and ~ 368 sccm (HFHP I regime) the critical oxygen concentration is the same, namely ~ $2\times10^{19}$ cm$^{-3}$. This critical level is seen for solar cells as well as for single i-layer electrical characteristics. For a total source gas flow of ~ 1015 sccm (HFHP II regime) the critical oxygen concentration increased to $C_{O,crit}$ ~ $2\times10^{20}$ cm$^{-3}$, which is only observed for solar cells and not for the

material (electrical) characteristics (values to be found back in Table 5.1 & Table 5.2). These critical levels are independent of light-soaking.

The critical oxygen concentration is speculated to depend on the oxygen precursor lifetime, namely $SiO_2$ clusters, siloxanes ($SiH_3$-O-$SiH_3$), and OH or $H_2O$ molecules that are formed by a reaction of silane and oxygen. It is proposed that for deposition regimes with a low oxygen incorporation probability (HFHP II) more of the stable siloxanes are incorporated with respect to the less stable hydrogen-oxygen molecules that are assumed to lead to oxygen in a doping configuration. In this case a low incorporation probability would be caused by a slower oxygen in-diffusion into the plasma zone, i.e. less oxygen is incorporated via OH or $H_2O$ molecules that as less stable compared to siloxane.

Furthermore it is observed that the oxygen incorporation probability is highest for the LFLP regime and lowest for the HFHP II regime. Thus, it is not surprising that the critical base pressures for the three regimes increase with increasing source gas flow. This is assumed to be due to, e.g., a decreased oxygen in-diffusion into the plasma zone or might be also due to an oxygen dilution in the source gas. An increase in deposition rate (i.e. discharge power) slightly decreases the incorporation probability due to a dilution of the oxygen with silane growth precursors due to an increased silane dissociation rate. For example, in the LFLP regime increasing the deposition rate from 0.15 nm/s to 0.5 nm/s by increasing the discharge power the incorporation probability can be reduced by a factor of three. However, after light-soaking the cell efficiency is about 0.5 % abs. lower compared to cells grown slowly. For the other regimes the suppression of oxygen incorporation via an increased deposition rate was even less but also for the high rate cells the degradation losses were more severe compared to those grown with lower rates.

### 9.1.3. Contamination sources and their influence

This section concludes the impact of different contamination sources and species on the performance of thin-film a-Si:H solar cells. It is found that the critical oxygen concentration depends on the oxygen source. Incorporated into the i-layer via a chamber wall leak a critical oxygen concentration of ~ $2\times10^{19}$ $cm^{-3}$ is found whereas the incorporation via gas pipe leak leads to $C_{O,crit}$ ~ $2\times10^{20}$ $cm^{-3}$ (values to be found back in Table 6.1). This is assumed to be due to a high reaction probability of oxygen and silane in the gas pipe outside of the plasma that is suggested to form a high amount of siloxane entering the deposition zone. The siloxane is assumed to promote the formation of electrically inactive twofold-coordinated oxygen in the i-layer of the solar cells. High quality a-Si:H solar cells were fabricated with gas pipe leak at the high oxygen concentration of $2\times10^{20}$ atoms/$cm^3$ (~ 0.5 at. %).

For nitrogen the decrease in solar cell performance is independent of the sources of contamination (values to be found back in Table 6.2). This can be explained by the lack of reactivity of nitrogen with silane outside of the plasma zone. The critical impurity levels do not change upon light-soaking.

Accompanied to theses solar cell studies also material studies on single contaminated i-layers were made. The two critical levels, found for the contaminated solar cells are seen as well for contaminated i-layers. Above the critical contamination level an increase in dark- and photoconductivity and a corresponding decrease in activation energy were seen. Exceeding an oxygen concentration of approximately 2 - $5\times10^{20}$ $cm^{-3}$ this effect was inversed. This electrical behaviour can be explained by different amounts of impurities incorporated in doping configurations providing additional charge carriers. In contrast, structural and optical film properties are linked to the absolute oxygen concentration and not to the assumed 0.5 ‰ oxygen (CWL) in doping configuration that influence the electrical film properties. Thus, these properties are not influenced by the leak source.

## 9.2. Atmospheric contamination of μc-Si:H

For microcrystalline solar cells grown in a regime similar to the HFHP I regime a source independent critical oxygen concentration of ~ $2\times10^{19}$ $cm^{-3}$ was found. This is assumed to be due to the high discharge power of 0.5 $W/cm^2$, usually used for the standard deposition process for μc-Si:H. Such a high power density leads to a decomposition of the siloxane and, thus, for both leak sources the same critical oxygen concentrations are seen. This assumption is supported by the fact that the deposition of μc-Si:H solar cells at a lower discharge power of 0.2 $W/cm^2$ (regime not suitable for industrial production) contaminated via gas pipe leak led to a critical oxygen concentration of ~ 7 - $9\times10^{19}$ $cm^{-3}$.

## 9.3. Single-chamber process

Based on the experience on impurity incorporation the realisation of a single-chamber process for the fabrication of state-of-the-art solar cells was made. The main aspect was the suppression of boron cross-contamination from the p-layer deposition into the subsequent i-layer. A systematic comparison of different reactor treatments and their time consumption was done. Moreover, the impact of different p/i-interface configurations on the effect of boron cross-contamination was studied.

The influence of the solar cell configuration on the boron cross-contamination is negligible. For the reactor treatment the application of a $H_2O$-flush or a process chamber evacuation to $9\times10^{-7}$ mbar turned out to be most favourable in order to suppress the boron cross-contamination. These two in-situ methods are fast and efficient. A drawback for the $H_2O$-flush is that this treatment is rather difficult to control. The chamber evacuation to $9\times10^{-7}$ mbar worked not in all deposition systems. It is assumed that boron recycling from the chamber walls plays a minor role for large-area deposition setups compared to a small-area deposition system. Finally, with a real single-chamber process initial solar cell and module efficiencies of 10.4 % (1 × 1 $cm^2$) and 9 % (40 × 40 $cm^2$) are achieved, respectively.

## 9.4. Outlook

In order to further investigate the impact of atmospheric contamination on silicon thin-film solar cells at the end of this study a modification of a deposition chamber of the 5K deposition setup was started. Thereby, it will be possible to premix contamination and process gas before admitting them to the reactor. Recently, a simulation study was launched that attempts to clarify the doping effect of the impurities.

At the LADA single-chamber deposition system the aim is to further reduce the time of the reactor treatment. A faster temperature stabilization after the reactor treatment could decrease the treatment time. Furthermore, the influence of the reactor treatment after the deposition of the phosphorous doped n-layer is of interest. Until now, after every deposited n-layer a $CO_2$-plasma treatment was applied. Finally, the development of single-chamber process for the deposition of μc-Si:H and a-Si:H / μc-Si:H tandem solar cells is planned.

# 10. References


**[Ama2001]**

E. Amanatides, S. Stamou, and D. Mataras, J. Appl. Phys. **90**, 5786 (2001)

**[Ama2010]**

Internet presence of Applied Materials inc. (2010), http://www.appliedmaterials.com/products/solar_multimedia.html

**[Ary1986]**

R.R. Arya, A. Catalano, and R.S. Oswald, Appl. Phys. Lett. **49**, 1089 (1986)

**[Ast2009]**

O. Astakhov, R. Carius, F. Finger, Y. Petrusenko, V. Borysenko, and D. Barankov, Phys. Rev. B **79**, 104205 (2009)

**[Ban2000]**

N. Banerji , J. Serra, S. Chiussi, B. León, M. Pérez-Amor, Appl. Surf. Sci. **168**, 52 (2000)

**[Bal2002]**

J. Ballutaud, A.A. Howling, L. Sansonnes, Ch. Hollenstein, U. Kroll, I. Schoenbaecher, C. Bucher, M. Poppeller, J. Weichart, A. Buelech, and F. Jomard, Proceedings of the 29th EPS Conf. On Plasma Phys. And Contr. Fusion (EPS, Mulhouse, France, 2002) p. 2029

**[Bal2004a]**

J. Ballutaud, C. Bucher, Ch. Hollenstein, A.A. Howling, U. Kroll, S. Benagli, A. Shah, and A. Buechel, Thin Solid Films **468**, 222 (2004)

**[Bal2004b]**

J. Ballutaud, "Study of Radio-Frequency Plasma Deposition of Amorphous Silicon for the Improvement of Solar Cells" (PhD-Thesis, Université Paris VI, 2004)

**[Ben1999]**

C. Beneking, B. Rech, S. Wieder, O. Kluth, H. Wagner, W. Frammelsberger, R. Geyer, P. Lechner, H. Ruèbel, H. Schade, Thin Solid Films **351**, 241 (1999)

**[Bey1983]**

W. Beyer and B. Hoheisel, Solid State Commun. **47**, 573 (1983)

**[Bey1984]**

W. Beyer and H. Overhof, in Semiconductors and Semimetals, edited by J.I. Pankove (Academic Press, Orlando, Florida, 1984)

**[Bey1998]**

W. Beyer and M.S. Abo Ghazala, Mat. Res. Soc. Symp. Proc. **507**, 601 (1998)

**[Bra2001]**

T. Brammer, "Die optoelektronischen Eigenschaften von mikro-kristallinen Silizium Solarzellen" (PhD-Thesis, Heinrich Heine Universität Düsseldorf, 2001)

**[Cab1989]**

P.R.i. Cabarrocas, S. Kumar, B. Drévillon, J. Appl. Phys. **66**, 3286 (1989)

**[Car1976]**

D. E. Carlson and C. R. Wronski, Solid State Commun. **17**, 1193 (1976)

**[Das2000]**

A. Dasgupta, A. Lambertz, O. Vetterl, F. Finger, R. Carius, U. Zastrow, and H. Wagner, Proceedings of the 16th European Photovoltaic Solar Energy Conference (WIP, München, Germany, 2000) p. 557

**[Don2007]**

M.N. van den Donkera, A. Gordijn, H. Stiebig, F. Finger, B. Rech, B. Stannowski, R. Bartl, E.A.G. Hamers, R. Schlatmann, and G.J. Jongerden, Solar Energy Materials & Solar Cells **91**, 572 (2007)

**[Fuj1992]**

S Fujikake, H Ohta, A Asano, Y Ichikawa, and H Sakai, Mater. Res. Soc. Symp. Proc. **258**, 875 (1992)

**[Gan2004]**

G. Ganguly, R.S. Oswald, and D.E. Carlson, Appl. Surf. Sci. **221**, 13 (2004)

**[Gra2005]**

U.S. Graf, "Single-chamber process development of microcrystalline Silicon solar cells and high-rate deposited intrinsic layers" (PhD-Thesis, Université de Neuchâtel, 2005)

**[Haa2007]**

C. Haase and H. Stiebig, Appl. Phys. Let **91**, 061116 (2007)

**[Hue2005]**

J. Huepkes, "Untersuchung des reaktiven Sputterprozesses zur Herstellung von aluminiumdotierten Zinkoxid-Schichten für Silizium-Dünnschichtsolarzellen" (PhD-Thesis, RWTH-Aachen, 2005)

**[Hru2008]**

D. Hrunski, B. Rech, T. Repmann, J. Kirchhoff, A. Gordijn, J. Huepkes, and W. Appenzeller, Proceedings of the 23rd European Photovoltaic Solar Energy Conference (WIP, München, Germany, 2008) p. 2292

**[Ich1993]**

Y. Ichikawa, S. Fujikake, T. Takayama, S. Saito, H. Ota, T. Yoshida, T. Ihara, and H. Sakai, Proc. Of the 23rd IEEE PVSEC (IEEE, Piscataway, NJ, 1993) p. 27

**[Ich1994]**

Y. Ichikawa, T. Ihara, T. Hama, Y. Watanuki, S. Kato, H. Ota, and H. Sakai, Proc. of the 1st WCPEC (1994) p.986

**[Ift1998]**

S.M. Iftiquar and A.K. Barua, Solar Energy Materials and Solar Cells **56**, 117 (1998)

**[Iso1996]**

M. Isomura, T. Kinoshita, and S. Tsuda, Appl. Phys. Lett. **68**, 1201 (1996)

**[Jae2007]**

A. Jäger-Waldorf, PV Status Report 2007 (JRC, Brüssel, Belgium, 2007)

**[Jae2009]**

A. Jaeger-Waldorf, in Physics of solar cells: from basics to last developments, (European School, Les Houches, France, 2009)

**[Kai2009]**

I. Kaizuka, G. Watt, P. Huesser, P. Cowley, and R. Bruendlinger, Proceedings of the 24th European Photovoltaic Solar Energy Conference (WIP, München, Germany, 2009) p. 4501

**[Ker1977]**

J. A. Kerr and A. F. Trotman-Dickenson, in CRC Handbock of Chemistry and Physics, (CRC Press, West Palm Beach, Florida, 1977)

**[Kil2009]**

T. Kilper, W. Beyer, G. Braeuer, T. Bronger, R. Carius, M. N. van den Donker, D. Hrunski, A. Lambertz, T. Merdzhanova, A. Mueck, B. Rech, W. Reetz, R. Schmitz, U. Zastrow, and A. Gordijn, J. Appl. Phys. **105**, 074509 (2009)

**[Kin1996]**

T. Kinoshita, M. Isamura, Y. Hishikawa, and S. Tsuda, Jpn. J. Appl. Phys. **35**, 3819 (1996)

**[Klu1996]**

O. Kluth, "Präparation und Charakterisierung von texturierten Metalloxid-Schichtenn für Dünnschichtsolarzellen" (Master-Thesis, RWTH Aachen , 1996)

**[Klu2001]**

O. Kluth, " Texturiertes Zinkoxid für Si-Dünnschichtsolarzellen" (PhD-Thesis, RWTH Aachen , 2001)

**[Kro1994]**

U. Kroll, "VHF-Plasmaabscheidung von amorphem Silizium: Einfluss der Anregungsfrequenz, der Reaktorgestaltung sowie Schichteigenschaften" (PhD-Thesis, Université de Neuchâtel, 1994)

**[Kro1995]**

U. Kroll, J. Meier, H. Keppner, A. Shah, S. D. Littlewood, I. E. Kelly, and P. Giannoulès, J. Vac. Sci. Technol. A **13**, 2742 (1995)

**[Kro1999]**

U. Kroll, D. Fischer, J. Meier, L. Sansonnes, A. Howling, and A. Shah, Mat. Res. Soc. Symp. Proc. **557**, 121 (1999)

**[Kro2004]**

U. Kroll, C. Bucher, S. Benagli, I. Schoenbaechler, J. Meier, A. Shah, J. Ballutaud, A. Howling, Ch. Hollenstein, A. Buechel, and M. Poppeller, Thin Solid Films **451-452**, 525 (2004)

**[Kub1994]**

M. Kubon, N. Schultz, M. Kolter, C. Beneking, and H. Wagner, Proceedings of the 12th European Photovoltaic Solar Energy Conference (WIP, München, Germany, 2008) p. 1268

**[Kub1995]**

M. Kubon, "Präparation und Eigenschaften der p-seitigen Grenzflächen in Solarzellen aus amorphem Silizium" (PhD-Thesis, RWTH Aachen, 1995)

**[Lan1992]**

A.A. Langford, M.L. Fleet, B.P. Nelson, W.A. Langford, and N. Maley, Phys. Rev. B **45**, 13367 (1992)

**[Loe1997]**

A. Loeffl, "Präparation hochleitfähiger transparenter Zinkoxid-schichten mit kontrollierter Texturierung für Dünnschichtsolarzellen" (Master-Thesis, Fachhochschule München, 1997)

**[Luc1983]**

G. Lucovsky, J. Yang, S.S. Chao, J.E. Tyler, and W. Czubatyj, Phys. Rev. B **28**, 3225 (1983)

**[Mah1987]**

A.H. Mahan, P. Raboisson, D.L. Williamson, and R. Tsu, Sol. Cells **21**, 117 (1987)

**[Mat1986]**

A. Matsuda, T. Yamaoka, S. Wolff, M. Koyama, Y. Imanishi, H. Kataoka, H. Matsuura, and K. Tanaka, J. Appl. Phys. **60**, 4025 (1986)

**[Mat1987]**

A. Matsuda and K. Tanaka, J. of Non-Cryst. Sol. **97&98**, 1367 (1987)

**[Mat2002]**

Material Safety Data Sheet, Nitrogen-Silane Mixtures (Chemical Safety Associates, La Mesa, CA, 2002)

**[Met1987]**

J. Metzdorf, Appl. Opt. **26**, 1701 (1987)

**[Mor1991]**

A. Morimoto, M. Matsumoto, M. Yoshita, M. Kumeda, and T. Shimizu, Appl. Phys. Lett. **59**, 2130 (1991)

**[Mot1967]**

N.F. Mott, Adv. Phys. **16**, 49 (1967)

**[Mue2000]**

A. Mueck, U. Zastrow, O. Vetterl, and B. Rech, Proc. of the 12th International Conference on Secondary Ion Mass Spectroscopy (Elservier, Amsterdam, Netherlands, 2000) p. 689

**[Mue2004]**

J. Mueller, B. Rech, J. Springer, and Milan Vanecek, Solar Energy **77**, 917 (2004)

**[Mun2004]**

G. Munyeme, M. Zeman, R.E.I. Schropp, and W.F. van der Weg, phys. stat. sol. **1**, 2298 (2004)

**[Ong2006]**

Y.Y. Ong, B.T. Chen, F.E. H. Tay, and C. Iliescu, Journal of Physics: Conference Series **34**, 812 (2006)

**[Pie2008]**

B. Pieters, "Characterization of Thin-Film Silicon Materials and Solar Cells through Numerical Modeling" (PhD-Thesis, TU Delft, 2008)

**[Pla1997]**

R. Platz, D. Fischer, S. Dubail, A. Shah, Solar Energy Materials and Solar Cells **41**, 475 (1997)

**[Rec1997]**

B. Rech, "Solarzellen aus amorphem Silizium mit hohem stabilem Wirkungs-grad" (PhD-Thesis, RWTH-Aachen, 1997)

**[Rec1998]**

B. Rech, C. Beneking, S. Wieder, U. Zastrow, F. Birmans, W. Appenzeller, O. Kluth, H. Stiebig, J. Foelsch, and H. Wagner, Proc. of the 2nd WCPEC (1998) p. 391

**[Rep2004]**

T. Repmann, W. Appenzeller, B. Sehrbrock, H. Stiebig, and B. Rech, Proceedings of the 19th European Photovoltaic Solar Energy Conference (WIP, München, Germany, 2004) p. 1334

**[Sak1990]**

H. Sakai, T. Yoshida, S. Fujikake, T. Hama, and Y. Ichikawa, J. of Appl. Phys. **67**, 3494 (1990)

**[Sak2007]**

I. Sakata, T. Kaimei, and M. Yamanaka, Phys. Rev. B **76**, 075206 (2007)

**[Sch1993]**

K. Schade and G. Suchaneck, in Solarzellen (Vieweg, Braunschweig/Wiesbaden, Germany, 1993)

**[Sch1994]**

A. Schoenecker, "Messung der spektralen Empfindlichkeit von Hochleistungszellen" (PhD-Thesis, Universität Freiburg, 1994)

**[Shi1991]**

T. Shimizu, M. Matsumoto, M. Yashita, M. Iwami, A. Morimoto, and M. Kumeda, J. Non-Cryst. Solids, **137&138**, 391 (1991)

**[Shi1994]**

H. Shinohara and M. Abe, Proc. of the 1st WCPEC, (1994) p.682

**[Sie1992]**

F. Siebke, "In-Situ Bestimmung der elektronischen Oberflächen- und Volumendefektdichte von amorphem Silizium (a-Si:H) und verwandten Legierungen" (PhD-Thesis, RWTH Aachen, 1997)

**[Sie1997]**

F. Siebke, H. Stiebig, and R. Carius, Solar Energy Materials and Solar Cells **49**, 7 (1997)

**[Smi2004]**

V. Smirnov, S. Reynolds, C. Main, F. Finger, and R. Carius, J. of Non-Cryst. Sol. **338-340**, 421 (2004)

**[Spe1975]**

W.E. Spear and P.G. LeComber, Sol. State Com. **17**, 1193 (1975)

**[Spr2005]**

J. Springer, B. Rech, W. Reetz, J. Müller, and M. Vanecek, Solar Energy Materials and Solar Cells **85**, 1 (2005)

**[Sta1977]**

D. L. Staebler and C.R. Wronski, Appl. Phys. Lett. **31**, 292 (1977)

**[Ste1965]**

H. F. Sterling and R.C.G. Swann, Solid State Electronics **8** 653 (1965)

**[Str1982]**

R.A. Street, Phys. Rev. Lett. **49**, 1187 (1982)

**[Str1985a]**

R.A. Street, J. Non-Cryst. Solids **77&78**, 1 (1985)

**[Str1985b]**

R.A. Street, M. Hack, and W.B. Jackson, Phys. Rev. B**37**, 4209 (1985)

**[Str1991]**

R.A. Street, in Hydrogenated Amorphous Silicon (Cambridge University Press, Cambridge, United Kingdom, 1991)

**[Stu1985]**

M. Stutzmann, W.B. Jackson, and C.C. Tsai, Phys. Rev B **32**, 23 (1985)

**[Stu1987]**

M. Stutzmann, D. K. Biegelsen, and R. A. Street, Phys. Rev. B **35**, 5666 (1987)

**[Taw1982]**

Y. Tawada, K. Tsuge, M. Kondo, H. Okamoto, and Y. Hamakawa, J. Appl. Phys. **53**, 5273 (1982)

**[Tor1998]**

M.P. Torres, PhD-thesis, "Microcrystalline Silicon Deposited by VHF-GP for Thin Film Solar Cells" (PhD-thesis, Université de Neuchâtel, 1998)

**[Tsa1988]**

C.C. Tsai, in Amorphous Silicon and Related Materials, (World Scientific, Singapore, 1988) p. 123

**[Van1981]**

M. Vanecek, J. Kocka, J. Stuchlik, A. Triska, Solid State Commun. **39**, 1199 (1981)

**[Vet2000]**

O. Vetterl, R. Carius, L. Houben, C. Scholten, M. Luysberg, A. Lambertz, F. Finger and H. Wagner, Mat. Res. Soc. Symp. Proc. **609**, 772 (2000)

**[Wit1988]**

T. Wittchen, H.C. Holstenberg, D. Huenerhof, Z.J. Min, and T. Metzdorf, Proc. Of the 20th IEEE PVSEC (IEEE, Piscataway, NJ, 1988) p. 1251

**[Win1990]**

K. Winer, R.A. Street, N.M. Johnson, and J. Walker, Phys. Rev. B **42**, 3120 (1990)

**[Woe2008]**

J. Woerdenweber, T. Merdzhanova, R. Schmitz, A. Mueck, U. Zastrow, L. Niessen, A. Gordijn, R. Carius, W. Beyer, H. Stiebig, and U. Rau, J. Appl. Phys **104**, 094507 (2008)

**[Woe2010]**

J. Woerdenweber, T. Merdzhanova, H. Stiebig, W. Beyer, and A. Gordijn, Appl. Phys. Let. **96**, 103505, (2010)

**[Woe2010]**

J. Woerdenweber, T. Merdzhanova, H. Stiebig, W. Beyer, and A. Gordijn, to be published

**[Wue2009]**

P. Wuerfel, Physics os Solar Cells – From Basic Principles to Advanced Concepts (wiley-vch, Weinheim, Germany, 2009)

**[Yan1994]**

J. Yang, X. Xu, and G. Guha, Mat Res. Soc. Symp. Proc. **336** 687 (1994)

**[Yos1988]**

T. Yoshida, S. Fujikake, H. Shimabukuro, Y. Ichikawa, and H. Sakai, Proc. Of the 20th IEEE PVSEC (IEEE, Piscataway, NJ, 1988) p 335

**[Zem1991]**

M. Zeman, I. Ferreira, M.J. Geerts, and J.W. Metselaar, Solar Energy Materials **21**, 255 (1991)

**[Zas2008]**

U. Zastrow, L. Niessen, private communication (2008)

**[Xi1994]**

J. Xi, D. Shugar, and H. Volltrauer, Proc. of the 1st WCPEC (1998) p. 401

# 11. Appendix

Overview of the deposition parameter and results obtained from the study on atmospheric contamination of a-Si:H and μc-Si:H solar cells.

| | $\Phi_{H2}$ [sccm] | $\Phi_{SiH4}$ [sccm] | $p$ [Torr] | $T_H$ [°C] |
|---|---|---|---|---|
| LFLP | 100 | 12 | 3 | 260 |
| HFHP I | 360 | 7.8 (1.6 – 2.4 for μc-Si:H) | 10 | 200 |
| HFHP II | 1000 | 15 | 10 | 200 |

*Table 11.1 Process parameters for the LFLP, HFHP I, and HFHP II regimes, respectively. Note, for the HFHP I regime also the process parameters for μc-Si:H deposition are given.*

| | $P$ [W/cm²] | $r_d$ [nm/s] | $p_{b,crit}$ [Torr] | $C_{crit}$ [cm$^{-3}$] |
|---|---|---|---|---|
| oxygen - LFLP - a-Si:H | | | (see *chapter 5*) | |
| CWL | 0.01/0.03 | 0.15/0.50 | $1\times10^{-6}$/$3\times10^{-6}$ | $2\times10^{19}$ |
| oxygen - HFHP I - a-Si:H | | | (see *chapters 4, 5 & 6*) | |
| CWL | 0.13/0.20 | 0.27/0.50 | $7\times10^{-6}$ | $2\times10^{19}$ |
| GPL | 0.20 | 0.50 | $1\times10^{-6}$ | $2\times10^{20}$ |
| nitrogen - HFHP I - a-Si:H | | | (see *chapters 4 & 6*) | |
| CWL | 0.20 | 0.50 | $1\times10^{-5}$ | $4\times10^{18}$ |
| GPL | 0.20 | 0.50 | $5\times10^{-6}$ | $4\times10^{18}$ |
| air - HFHP I - a-Si:H | | | (see *chapter 4*) | |
| CWL | 0.20 | 0.50 | $8\times10^{-6}$ | $1.7\times10^{19}$ (O)/$1.7\times10^{18}$ (N) |
| oxygen - HFHP I - μc-Si:H | | | (see *chapter 6*) | |
| CWL | 0.5 | 0.50 | $4\times10^{-6}$ | 1-2×10$^{19}$ |
| GPL | 0.2/0.5 | 0.27/0.50 | $1\times10^{-7}$ | 7-9×10$^{19}$/1-2×10$^{19}$ |
| oxygen - HFHP II - a-Si:H | | | (see *chapter 5*) | |
| CWL | 0.13/0.20 | 0.27/0.44 | $2\times10^{-4}$ | $2\times10^{20}$ |

*Table 11.2 Overview of deposition parameters, critical impurity concentrations, critical base pressures, and leak sources for all applied deposition regimes.*

# 12. Acknowledgements

An dieser Stelle möchte mich bei allen Leuten bedanken, die mir diese Arbeit ermöglicht haben.

*Professor Dr. Matthias Wuttig*: Für die Betreuung und Begutachtung der Arbeit

*Professor Dr. Uwe Rau*: Für die Möglichkeit eine interessante Arbeit an seinem Institut durchführen zu können, die damit zur Verfügung gestellte Ausrüstung und seine hilfreichen Ratschläge. Des Weiteren für die Betreuung und Begutachtung der Arbeit

*Dr. Tsvetelina Merdzhanova*: Für eine sehr gute Betreuung meiner Arbeit und viele interessante und hilfreiche Diskussionen. Danke auch für die Verbesserungsvorschläge bzgl. dieser Arbeit und für eine ständige Hilfsbereitschaft.

*Dr. Aad Gordijn*: Für eine sehr gute Betreuung meiner Arbeit besonders während des letzten Jahres und viele interessante und hilfreiche Anregungen. Danke auch für das Korrekturlesen dieser Arbeit und für eine ständige Hilfsbereitschaft.

*Dr. Wolfhard Beyer*: Für die vielen und sehr hilfreichen Diskussionen.

*Professor Dr. Helmut Stiebig*: Für die Betreuung dieser Arbeit im Rahmen der Kooperation mit der Firma Malibu GmbH.

*Professor Dr. Roger Wördenweber*: Für die sorgfältige Durchsicht meines Manuskripts.

*Dipl. Ing. Ralf Schmitz & Dipl. Ing. Andreas Mück*: Für die Herstellung der Solarzellen und der Einzelschichten in der 5K-Depositionsanlage.

*Lars Nießen & Dipl. Ing. Uwe Zastrow*: Für die vielen SIMS-Messungen.

*Dipl. Ing. Wilfried Reetz & Rebecca van Aubel*: Für die Hilfe bei der Charakterisierung der Solarzellen.

Allen anderen Kollegen, die hier nicht namentlich erwähnt, sind möchte ich danken für viele fruchtbare Diskussion und das sehr angenehme Arbeitsumfeld.

1. **Einsatz von multispektralen Satellitenbilddaten in der Wasserhaushalts- und Stoffstrommodellierung – dargestellt am Beispiel des Rureinzugsgebietes**
   von C. Montzka (2008), XX, 238 Seiten
   ISBN: 978-3-89336-508-1

2. **Ozone Production in the Atmosphere Simulation Chamber SAPHIR**
   by C. A. Richter (2008), XIV, 147 pages
   ISBN: 978-3-89336-513-5

3. **Entwicklung neuer Schutz- und Kontaktierungsschichten für Hochtemperatur-Brennstoffzellen**
   von T. Kiefer (2008), 138 Seiten
   ISBN: 978-3-89336-514-2

4. **Optimierung der Reflektivität keramischer Wärmedämmschichten aus Yttrium-teilstabilisiertem Zirkoniumdioxid für den Einsatz auf metallischen Komponenten in Gasturbinen**
   von A. Stuke (2008), X, 201 Seiten
   ISBN: 978-3-89336-515-9

5. **Lichtstreuende Oberflächen, Schichten und Schichtsysteme zur Verbesserung der Lichteinkopplung in Silizium-Dünnschichtsolarzellen**
   von M. Berginski (2008), XV, 171 Seiten
   ISBN: 978-3-89336-516-6

6. **Politikszenarien für den Klimaschutz IV – Szenarien bis 2030**
   hrsg.von P. Markewitz, F. Chr. Matthes (2008), 376 Seiten
   ISBN 978-3-89336-518-0

7. **Untersuchungen zum Verschmutzungsverhalten rheinischer Braunkohlen in Kohledampferzeugern**
   von A. Schlüter (2008), 164 Seiten
   ISBN 978-3-89336-524-1

8. **Inorganic Microporous Membranes for Gas Separation in Fossil Fuel Power Plants**
   by G. van der Donk (2008), VI, 120 pages
   ISBN: 978-3-89336-525-8

9. **Sinterung von Zirkoniumdioxid-Elektrolyten im Mehrlagenverbund der oxidkeramischen Brennstoffzelle (SOFC)**
   von R. Mücke (2008), VI, 165 Seiten
   ISBN: 978-3-89336-529-6

10. **Safety Considerations on Liquid Hydrogen**
    by K. Verfondern (2008), VIII, 167 pages
    ISBN: 978-3-89336-530-2

11. **Kerosinreformierung für Luftfahrtanwendungen**
von R. C. Samsun (2008), VII, 218 Seiten
ISBN: 978-3-89336-531-9

12. **Der 4. Deutsche Wasserstoff Congress 2008 – Tagungsband**
hrsg. von D. Stolten, B. Emonts, Th. Grube (2008), 269 Seiten
ISBN: 978-3-89336-533-3

13. **Organic matter in Late Devonian sediments as an indicator for environmental changes**
by M. Kloppisch (2008), XII, 188 pages
ISBN: 978-3-89336-534-0

14. **Entschwefelung von Mitteldestillaten für die Anwendung in mobilen Brennstoffzellen-Systemen**
von J. Latz (2008), XII, 215 Seiten
ISBN: 978-3-89336-535-7

15. **RED-IMPACT**
**Impact of Partitioning, Transmutation and Waste Reduction Technologies on the Final Nuclear Waste Disposal**
SYNTHESIS REPORT
ed. by W. von Lensa, R. Nabbi, M. Rossbach (2008), 178 pages
ISBN 978-3-89336-538-8

16. **Ferritic Steel Interconnectors and their Interactions with Ni Base Anodes in Solid Oxide Fuel Cells (SOFC)**
by J. H. Froitzheim (2008), 169 pages
ISBN: 978-3-89336-540-1

17. **Integrated Modelling of Nutrients in Selected River Basins of Turkey**
Results of a bilateral German-Turkish Research Project
project coord. M. Karpuzcu, F. Wendland (2008), XVI, 183 pages
ISBN: 978-3-89336-541-8

18. **Isotopengeochemische Studien zur klimatischen Ausprägung der Jüngeren Dryas in terrestrischen Archiven Eurasiens**
von J. Parplies (2008), XI, 155 Seiten, Anh.
ISBN: 978-3-89336-542-5

19. **Untersuchungen zur Klimavariabilität auf dem Tibetischen Plateau - Ein Beitrag auf der Basis stabiler Kohlenstoff- und Sauerstoffisotope in Jahrringen von Bäumen waldgrenznaher Standorte**
von J. Griessinger (2008), XIII, 172 Seiten
ISBN: 978-3-89336-544-9

20. **Neutron-Irradiation + Helium Hardening & Embrittlement Modeling of 9%Cr-Steels in an Engineering Perspective (HELENA)**
by R. Chaouadi (2008), VIII, 139 pages
ISBN: 978-3-89336-545-6

21. **in Bearbeitung**

22. **Verbundvorhaben APAWAGS (AOEV und Wassergenerierung) – Teilprojekt: Brennstoffreformierung – Schlussbericht**
von R. Peters, R. C. Samsun, J. Pasel, Z. Porš, D. Stolten (2008), VI, 106 Seiten
ISBN: 978-3-89336-547-0

23. **FREEVAL**
Evaluation of a Fire Radiative Power Product derived from Meteosat 8/9 and Identification of Operational User Needs
Final Report
project coord. M. Schultz, M. Wooster (2008), 139 pages
ISBN: 978-3-89336-549-4

24. **Untersuchungen zum Alkaliverhalten unter Oxycoal-Bedingungen**
von C. Weber (2008), VII, 143, XII Seiten
ISBN: 978-3-89336-551-7

25. **Grundlegende Untersuchungen zur Freisetzung von Spurstoffen, Heißgaschemie, Korrosionsbeständigkeit keramischer Werkstoffe und Alkalirückhaltung in der Druckkohlenstaubfeuerung**
von M. Müller (2008), 207 Seiten
ISBN: 978-3-89336-552-4

26. **Analytik von ozoninduzierten phenolischen Sekundärmetaboliten in *Nicotiana tabacum* L. cv Bel W3 mittels LC-MS**
von I. Koch (2008), III, V, 153 Seiten
ISBN 978-3-89336-553-1

27. **IEF-3 Report 2009. Grundlagenforschung für die Anwendung**
(2009), ca. 230 Seiten
ISBN: 978-3-89336-554-8

28. **Influence of Composition and Processing in the Oxidation Behavior of MCrAlY-Coatings for TBC Applications**
by J. Toscano (2009), 168 pages
ISBN: 978-3-89336-556-2

29. **Modellgestützte Analyse signifikanter Phosphorbelastungen in hessischen Oberflächengewässern aus diffusen und punktuellen Quellen**
von B. Tetzlaff (2009), 149 Seiten
ISBN: 978-3-89336-557-9

30. **Nickelreaktivlot / Oxidkeramik – Fügungen als elektrisch isolierende Dichtungskonzepte für Hochtemperatur-Brennstoffzellen-Stacks**
von S. Zügner (2009), 136 Seiten
ISBN: 978-3-89336-558-6

31. **Langzeitbeobachtung der Dosisbelastung der Bevölkerung in radioaktiv kontaminierten Gebieten Weißrusslands – Korma-Studie**
von H. Dederichs, J. Pillath, B. Heuel-Fabianek, P. Hill, R. Lennartz (2009), Getr. Pag.
ISBN: 978-3-89336-532-3

32. **Herstellung von Hochtemperatur-Brennstoffzellen über physikalische Gasphasenabscheidung**
von N. Jordán Escalona (2009), 148 Seiten
ISBN: 978-3-89336-532-3

33. **Real-time Digital Control of Plasma Position and Shape on the TEXTOR Tokamak**
by M. Mitri (2009), IV, 128 pages
ISBN: 978-3-89336-567-8

34. **Freisetzung und Einbindung von Alkalimetallverbindungen in kohlebefeuerten Kombikraftwerken**
von M. Müller (2009), 155 Seiten
ISBN: 978-3-89336-568-5

35. **Kosten von Brennstoffzellensystemen auf Massenbasis in Abhängigkeit von der Absatzmenge**
von J. Werhahn (2009), 242 Seiten
ISBN: 978-3-89336-569-2

36. **Einfluss von Reoxidationszyklen auf die Betriebsfestigkeit von anodengestützten Festoxid-Brennstoffzellen**
von M. Ettler (2009), 138 Seiten
ISBN: 978-3-89336-570-8

37. **Großflächige Plasmaabscheidung von mikrokristallinem Silizium für mikromorphe Dünnschichtsolarmodule**
von T. Kilper (2009), XVII, 154 Seiten
ISBN: 978-3-89336-572-2

38. **Generalized detailed balance theory of solar cells**
by T. Kirchartz (2009), IV, 198 pages
ISBN: 978-3-89336-573-9

39. **The Influence of the Dynamic Ergodic Divertor on the Radial Electric Field at the Tokamak TEXTOR**
von J. W. Coenen (2009), xii, 122, XXVI pages
ISBN: 978-3-89336-574-6

40. **Sicherheitstechnik im Wandel Nuklearer Systeme**
von K. Nünighoff (2009), viii, 215 Seiten
ISBN: 978-3-89336-578-4

41. **Pulvermetallurgie hochporöser NiTi-Legierungen für Implanat- und Dämpfungsanwendungen**
von M. Köhl (2009), XVII, 199 Seiten
ISBN: 978-3-89336-580-7

42. **Einfluss der Bondcoatzusammensetzung und Herstellungsparameter auf die Lebensdauer von Wärmedämmschichten bei zyklischer Temperaturbelastung**
von M. Subanovic (2009), 188, VI Seiten
ISBN: 978-3-89336-582-1

43. **Oxygen Permeation and Thermo-Chemical Stability of Oxygen Permeation Membrane Materials for the Oxyfuel Process**
by A. J. Ellett (2009), 176 pages
ISBN: 978-3-89336-581-4

44. **Korrosion von polykristallinem Aluminiumoxid (PCA) durch Metalljodidschmelzen sowie deren Benetzungseigenschaften**
von S. C. Fischer (2009), 148 Seiten
ISBN: 978-3-89336-584-5

45. **IEF-3 Report 2009. Basic Research for Applications**
(2009), 217 Seiten
ISBN: 978-3-89336-585-2

46. **Verbundvorhaben ELBASYS (Elektrische Basissysteme in einem CFK-Rumpf) - Teilprojekt: Brennstoffzellenabgase zur Tankinertisierung - Schlussbericht**
von R. Peters, J. Latz, J. Pasel, R. C. Samsun, D. Stolten
(2009), xi, 202 Seiten
ISBN: 978-3-89336-587-6

47. **Aging of $^{14}$C-labeled Atrazine Residues in Soil: Location, Characterization and Biological Accessibility**
by N. D. Jablonowski (2009), IX, 104 pages
ISBN: 978-3-89336-588-3

48. **Entwicklung eines energetischen Sanierungsmodells für den europäischen Wohngebäudesektor unter dem Aspekt der Erstellung von Szenarien für Energie- und $CO_2$ - Einsparpotenziale bis 2030**
von P. Hansen (2009), XXII, 281 Seiten
ISBN: 978-3-89336-590-6

49. **Reduktion der Chromfreisetzung aus metallischen Interkonnektoren für Hochtemperaturbrennstofzellen durch Schutzschichtsysteme**
von R. Trebbels (2009), iii, 135 Seiten
ISBN: 978-3-89336-591-3

50. **Bruchmechanische Untersuchung von Metall / Keramik-Verbundsystemen für die Anwendung in der Hochtemperaturbrennstoffzelle**
von B. Kuhn (2009), 118 Seiten
ISBN: 978-3-89336-592-0

51. **Wasserstoff-Emissionen und ihre Auswirkungen auf den arktischen Ozonverlust**
**Risikoanalyse einer globalen Wasserstoffwirtschaft**
von T. Feck (2009), 180 Seiten
ISBN: 978-3-89336-593-7

52. **Development of a new Online Method for Compound Specific Measurements of Organic Aerosols**
by T. Hohaus (2009), 156 pages
ISBN: 978-3-89336-596-8

53. **Entwicklung einer FPGA basierten Ansteuerungselektronik für Justageeinheiten im Michelson Interferometer**
von H. Nöldgen (2009), 121 Seiten
ISBN: 978-3-89336-599-9

54. **Observation – and model – based study of the extratropical UT/LS**
by A. Kunz (2010), xii, 120, xii pages
ISBN: 978-3-89336-603-3

55. **Herstellung polykristalliner Szintillatoren für die Positronen-Emissions-Tomographie (PET)**
von S. K. Karim (2010), VIII, 154 Seiten
ISBN: 978-3-89336-610-1

56. **Kombination eines Gebäudekondensators mit H2-Rekombinatorelementen in Leichwasserreaktoren**
von S. Kelm (2010), vii, 119 Seiten
ISBN: 978-3-89336-611-8

57. **Plant Leaf Motion Estimation Using A 5D Affine Optical Flow Model**
by T. Schuchert (2010), X, 143 pages
ISBN: 978-3-89336-613-2

58. **Tracer-tracer relations as a tool for research on polar ozone loss**
by R. Müller (2010), 116 pages
ISBN: 978-3-89336-614-9

59. **Sorption of polycyclic aromatic hydrocarbon (PAH) to Yangtze River sediments and their components**
by J. Zhang (2010), X, 109 pages
ISBN: 978-3-89336-616-3

60. **Weltweite Innovationen bei der Entwicklung von CCS-Technologien und Möglichkeiten der Nutzung und des Recyclings von $CO_2$**
Studie im Auftrag des BMWi
von W. Kuckshinrichs et al. (2010), X, 139 Seiten
ISBN: 978-3-89336-617-0

61. **Herstellung und Charakterisierung von sauerstoffionenleitenden Dünnschichtmembranstrukturen**
von M. Betz (2010), XII, 112 Seiten
ISBN: 978-3-89336-618-7

62. **Politikszenarien für den Klimaschutz V – auf dem Weg zum Strukturwandel, Treibhausgas-Emissionsszenarien bis zum Jahr 2030**
hrsg. von P. Hansen, F. Chr. Matthes (2010), 276 Seiten
ISBN: 978-3-89336-619-4

63. **Charakterisierung Biogener Sekundärer Organischer Aerosole mit Statistischen Methoden**
von C. Spindler (2010), iv, 163 Seiten
ISBN: 978-3-89336-622-4

64. **Stabile Algorithmen für die Magnetotomographie an Brennstoffzellen**
von M. Wannert (2010), ix, 119 Seiten
ISBN: 978-3-89336-623-1

65. **Sauerstofftransport und Degradationsverhalten von Hochtemperaturmembranen für CO2-freie Kraftwerke**
von D. Schlehuber (2010), VII, 139 Seiten
ISBN: 978-3-89336-630-9

66. **Entwicklung und Herstellung von foliengegossenen, anodengestützten Festoxidbrennstoffzellen**
von W. Schafbauer (2010), VI, 164 Seiten
ISBN: 978-3-89336-631-6

67. **Disposal strategy of proton irradiated mercury from high power spallation sources**
by S. Chiriki (2010), xiv, 124 pages
ISBN: 978-3-89336-632-3

68. **Oxides with polyatomic anions considered as new electrolyte materials for solid oxide fuel cells (SOFCs)**
by O. H. Bin Hassan (2010), vii, 121 pages
ISBN: 978-3-89336-633-0

69. **Von der Komponente zum Stack: Entwicklung und Auslegung von HT-PEFC-Stacks der 5 kW-Klasse**
von A. Bendzulla (2010), IX, 203 Seiten
ISBN: 978-3-89336-634-7

70. **Satellitengestützte Schwerewellenmessungen in der Atmosphäre und Perspektiven einer zukünftigen ESA Mission (PREMIER)**
von S. Höfer (2010), 81 Seiten
ISBN: 978-3-89336-637-8

71. **Untersuchungen der Verhältnisse stabiler Kohlenstoffisotope in atmosphärisch relevanten VOC in Simulations- und Feldexperimenten**
von H. Spahn (2010), IV, 210 Seiten
ISBN: 978-3-89336-638-5

72. **Entwicklung und Charakterisierung eines metallischen Substrats für nanostrukturierte keramische Gastrennmembranen**
von K. Brands (2010), vii, 137 Seiten
ISBN: 978-3-89336-640-8

73. **Hybridisierung und Regelung eines mobilen Direktmethanol-Brennstoffzellen-Systems**
von J. Chr. Wilhelm (2010), 220 Seiten
ISBN: 978-3-89336-642-2

74. **Charakterisierung perowskitischer Hochtemperaturmembranen zur Sauerstoffbereitstellung für fossil gefeuerte Kraftwerksprozesse**
von S.A. Möbius (2010) III, 208 Seiten
ISBN: 978-3-89336-643-9

75. **Characterization of natural porous media by NMR and MRI techniques: High and low magnetic field studies for estimation of hydraulic properties**
by L.-R. Stingaciu (2010), 96 pages
ISBN: 978-3-89336-645-3

76. **Hydrological Characterization of a Forest Soil Using Electrical Resistivity Tomography**
by Chr. Oberdörster (2010), XXI, 151 pages
ISBN: 978-3-89336-647-7

77. **Ableitung von atomarem Sauerstoff und Wasserstoff aus Satellitendaten und deren Abhängigkeit vom solaren Zyklus**
von C. Lehmann (2010), 127 Seiten
ISBN: 978-3-89336-649-1

78. **18th World Hydrogen Energy Conference 2010 – WHEC2010 Proceedings**
**Speeches and Plenary Talks**
ed. by D. Stolten, B. Emonts (2010)
ISBN: 978-3-89336-658-3

78-1. **18th World Hydrogen Energy Conference 2010 – WHEC2010 Proceedings**
**Parallel Sessions Book 1:**
**Fuel Cell Basics / Fuel Infrastructures**
ed. by D. Stolten, T. Grube (2010), ca. 460 pages
ISBN: 978-3-89336-651-4

78-2. **18th World Hydrogen Energy Conference 2010 – WHEC2010 Proceedings**
**Parallel Sessions Book 2:**
**Hydrogen Production Technologies – Part 1**
ed. by D. Stolten, T. Grube (2010), ca. 400 pages
ISBN: 978-3-89336-652-1

78-3. **18th World Hydrogen Energy Conference 2010 – WHEC2010 Proceedings**
**Parallel Sessions Book 3:**
**Hydrogen Production Technologies – Part 2**
ed. by D. Stolten, T. Grube (2010), ca. 640 pages
ISBN: 978-3-89336-653-8

78-4. **18th World Hydrogen Energy Conference 2010 – WHEC2010 Proceedings**
**Parallel Sessions Book 4:**
**Storage Systems / Policy Perspectives, Initiatives and Cooperations**
ed. by D. Stolten, T. Grube (2010), ca. 500 pages
ISBN: 978-3-89336-654-5

78-5. **18th World Hydrogen Energy Conference 2010 – WHEC2010 Proceedings**
**Parallel Sessions Book 5:**
**Stategic Analysis / Safety Issues / Existing and Emerging Markets**
ed. by D. Stolten, T. Grube (2010), ca. 530 pages
ISBN: 978-3-89336-655-2

78-6. **18th World Hydrogen Energy Conference 2010 – WHEC2010 Proceedings**
**Parallel Sessions Book 6:**
**Stationary Applications / Transportation Applications**
ed. by D. Stolten, T. Grube (2010), ca. 330 pages
ISBN: 978-3-89336-656-9

78 Set (complete book series)

**18th World Hydrogen Energy Conference 2010 – WHEC2010 Proceedings**
ed. by D. Stolten, T. Grube, B. Emonts (2010)
ISBN: 978-3-89336-657-6

79. **Ultrafast voltex core dynamics investigated by finite-element micromagnetic simulations**
by S. Gliga (2010), vi, 144 pages
ISBN: 978-3-89336-660-6

80. **Herstellung und Charakterisierung von keramik- und metallgestützten Membranschichten für die $CO_2$-Abtrennung in fossilen Kraftwerken**
von F. Hauler (2010), XVIII, 178 Seiten
ISBN: 978-3-89336-662-0

81. **Experiments and numerical studies on transport of sulfadiazine in soil columns**
by M. Unold (2010), xvi, 115 pages
ISBN: 978-3-89336-663-7

82. **Prompt-Gamma-Neutronen-Aktivierungs-Analyse zur zerstörungsfreien Charakterisierung radioaktiver Abfälle**
von J.P.H. Kettler (2010), iv, 205 Seiten
ISBN: 978-3-89336-665-1

83. **Transportparameter dünner geträgerter Kathodenschichten der oxidkeramischen Brennstoffzelle**
von C. Wedershoven (2010), vi, 137 Seiten
ISBN: 978-3-89336-666-8

84. **Charakterisierung der Quellverteilung von Feinstaub und Stickoxiden in ländlichem und städtischem Gebiet**
von S. Urban (2010), vi, 211 Seiten
ISBN: 978-3-89336-669-9

85. **Optics of Nanostructured Thin-Film Silicon Solar Cells**
by C. Haase (2010), 150 pages
ISBN: 978-3-89336-671-2

86. **Entwicklung einer Isolationsschicht für einen Leichtbau-SOFC-Stack**
von R. Berhane (2010), X, 162 Seiten
ISBN: 978-3-89336-672-9

87. **Hydrogen recycling and transport in the helical divertor of TEXTOR**
by M. Clever (2010), x, 172 pages
ISBN: 978-3-89336-673-6

88. **Räumlich differenzierte Quantifizierung der N- und P-Einträge in Grundwasser und Oberflächengewässer in Nordrhein-Westfalen unter besonderer Berücksichtigung diffuser landwirtschaftlicher Quellen**
von F. Wendland et. al. (2010), xii, 216 Seiten
ISBN: 978-3-89336-674-3

89. **Oxidationskinetik innovativer Kohlenstoffmaterialien hinsichtlich schwerer Lufteinbruchstörfälle in HTR´s und Graphitentsorgung oder Aufarbeitung**
von B. Schlögl (2010), ix, 117 Seiten
ISBN: 978-3-89336-676-7

90. **Chemische Heißgasreinigung bei Biomassenvergasungsprozessen**
von M. Stemmler (2010), xv, 196 Seiten
ISBN: 978-3-89336-678-1

91. **Untersuchung und Optimierung der Serienverschaltung von Silizium-Dünnschicht-Solarmodulen**
von S. Haas (2010), ii, 202 Seiten
ISBN: 978-3-89336-680-4

92. **Non-invasive monitoring of water and solute fluxes in a cropped soil**
by S. Garré (2010), xxiv, 133 pages
ISBN: 978-3-89336-681-1

93. **Improved hydrogen sorption kinetics in wet ball milled Mg hydrides**
by L. Meng (2011), II, 119 pages
ISBN: 978-3-89336-687-3

94. **Materials for Advanced Power Engineering 2010**
ed. by J. Lecomte-Beckers, Q. Contrepois, T. Beck and B. Kuhn
(2010), 1327 pages
ISBN: 978-3-89336-685-9

95. **2D cross-hole MMR – Survey design and sensitivity analysis for cross-hole applications of the magnetometric resistivity**
by D. Fielitz (2011), xvi, 123 pages
ISBN: 978-3-89336-689-7

96. **Untersuchungen zur Oberflächenspannung von Kohleschlacken unter Vergasungsbedingungen**
von T. Melchior (2011), xvii, 270 Seiten
ISBN: 978-3-89336-690-3

97. **Secondary Organic Aerosols: Chemical Aging, Hygroscopicity, and Cloud Droplet Activation**
by A. Buchholz (2011), xiv, 134 pages
ISBN: 978-3-89336-691-0

98. **Chrom-bezogene Degradation von Festoxid-Brennstoffzellen**
von A. Neumann (2011), xvi, 218 Seiten
ISBN: 978-3-89336-692-7

99. **Amorphous and microcrystalline silicon applied in very thin tandem solar cells**
by S. Schicho (2011), XII, 190 pages
ISBN: 978-3-89336-693-4

100. **Sol-gel and nano-suspension electrolyte layers for high performance solid oxide fuel cells**
by F. Han (2011), iv, 131 pages
ISBN: 978-3-89336-694-1

101. **Impact of different vertical transport representations on simulating processes in the tropical tropopause layer (TTL)**
by F. Plöger (2011), vi, 104 pages
ISBN: 978-3-89336-695-8

102. **Untersuchung optischer Nanostrukturen für die Photovoltaik mit Nahfeldmikroskopie**
von T. Beckers (2011), xiii, 128 Seiten
ISBN: 978-3-89336-696-5

103. **Impact of contamination on hydrogenated amorphous silicon thin films & solar cells**
by J. Wördenweber (2011), XIV, 138 pages
ISBN: 978-3-89336-697-2

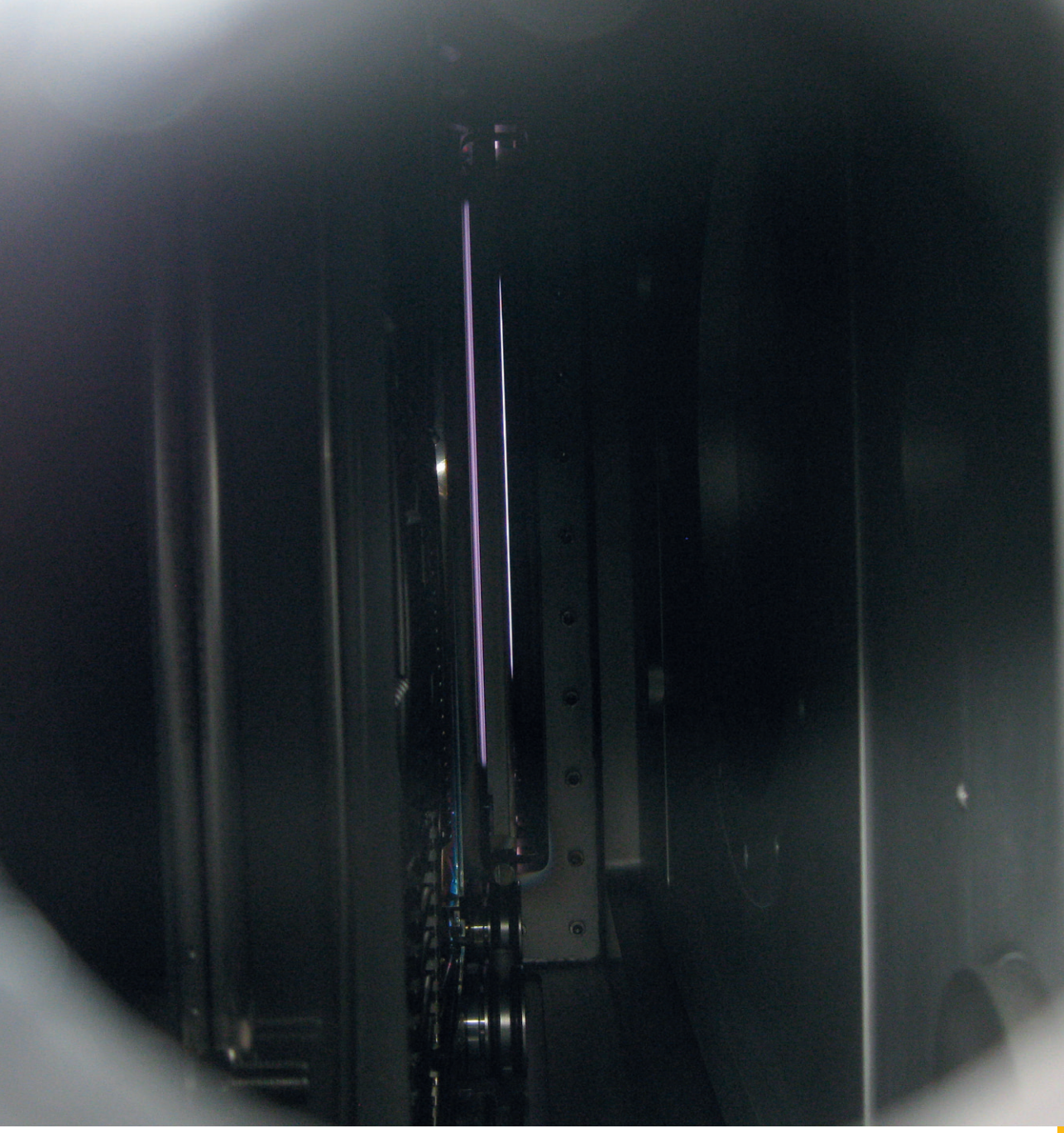

Energie & Umwelt / Energy & Environment
Band / Volume 103
ISBN 978-3-89336-697-2

JÜLICH
FORSCHUNGSZENTRUM